# Chemical and mineralogical fingerprinting of loess-mantled soils on different underlying substrates in Lower Silesia (Poland)

GEO 511 Master's Thesis

**Author**

Martina Vögtli

12-054-623

**Supervisor and faculty representative**

Prof. Dr. Markus Egli

University of Zurich -
Department of Geography
Winterthurerstrasse 190

8057 Zürich, Switzerland

markus.egli@geo.uzh.ch

**Supervisor**

Dr. Jaroslaw Waroszewski

Wroclaw University of Environmental and Life Sciences -
Institute of Soil Science and Environmental Protection
Grunwaldzka 53

50-357 Wroclaw, Poland

jaroslaw.waroszewski@upwr.edu.pl

23rd of September 2018

# Table of contents

# Figures

# Tables

3

# 1. Abstract

Loess deposits are an excellent source of information and are thus used to reconstruct paleoenvironment and -climate. This can include the extent of glaciation, sources of dust or dust pathways. However, loess mantled soils have been studied in southwestern Poland and the formation of an argic horizon due to clay translocation has been discovered and the development of certain soil types like Alisols, Luvisols, Leptosols or Cambisols due to silt addition has been described previously.

Nevertheless, the question how the clay and the heavy mineralogy are reflected in such loess mantled soils, is still a matter of debate. The main questions are if the discontinuities found in the soil texture and soil geomorphology are also reflected in the clay and heavy mineralogy, the geochemistry and the physical parameters, and where the loess deposits have their origin. Therefore, five different profiles in Lower Silesia (Poland) were studied. The five profiles are characterized by thin, reworked loess mantles which cover different underlying substrates, namely: Permian sandstone, basalt, granite, serpentinite and glacio-fluvial material. To test the hypotheses, the geochemistry and physical parameters of representative horizons (loess mantle, transition horizon, underlying substrate) were examined. Furthermore, XRD-, SEM- and DRIFT-analyzes were conducted to answer the research questions.

The results show that clear boundaries in the profiles are not only found in the geochemistry and particles sizes but also are reflected in the clay and heavy mineralogy. The loess mantles have characteristic clay minerals like kaolinite, mica, vermiculite, smectite, chlorite and hydroxy-interlayered vermiculite (HIV) or interstratified mica-vermiculite. In the Luvisols and the Stagnosol, the clay translocation was observed by accumulation of dioctahedral clay minerals in the lower horizons whereas the Alisol showed the highest occurrence in the loess mantle. The formation of HIV or interstratified mica-vermiculite and the transformation from chlorite and/or mica to vermiculite is traced back to the loess mantles. Also, the different underlying substrates are reflected in their characteristic clay and heavy mineral compositions. Regarding the topography, higher erosional processes on slopes occur and lead to rather shallow loess mantles.

The Ti/Zr and K/Rb ratios were calculated revealing that the provenance of the studied loess mantles were comparable with results from Germany. Hence, the loess might originate from the vegetation poor periglacial areas during Last Glacial Maximum (LGM) when the Scandinavian ice sheet covered northern Europe, but the southern lying Sudety mountains can not be excluded as a possible loess source.

# 2. Introduction

Loess, a terrestrial clastic sediment consisting mainly of silt-sized particles, is the result of accumulation of wind-blown dust. Loess deposits are important sources of information. They can illustrate the extent and intensity of glaciations or the variations in global atmospheric circulation (Pye 1995). Loess soils are known as the most fertile in the world, mainly due to the silt particles which ensure the supply of plant-available water, soil aeration, extensive penetration by plant roots and ease of cultivation. Besides, they also have moderately large reserves of most mineral nutrients (Catt 2001).

Most loess deposits show evidence of modification to some degree by syn- or post-depositional reworking, bioturbation, weathering or pedogenesis. This modified loess can range from weakly developed leached layers to intensely weathered paleosols and pedocomplexes. The mineralogy of loess in different parts of the world varies and thus reflects the nature of the surficial geology and the effectiveness of sediment mixing processes in individual source regions. Most deposits comprise of quartz as the dominant constituent with a content of 45-55 %. The remaining material in loess is composed of feldspars, carbonates, heavy minerals, clay minerals and volcanic glass shards (Pye 1995). The importance of clay and heavy minerals will be highlighted as these materials are the main focus of the thesis. Many clay-sized particles (< 2 μm) are phyllosilicates such as micas, kaolinite, smectite, vermiculite, and chlorite (Muhs 2013). Clays are categorized based on the combination of their octahedral and tetrahedral sheets and their layer charge. Through isomorphous substitution a net negative charge on the structure is possible which leads to a higher cation exchange. In soils, a high cation exchange capacity (CEC) coincides with a high soil fertility (Schaetzl and Anderson 2005; Scheffer et al. 2010). Heavy minerals are also important nutrient sources and furthermore possible indicators of sediment provenance (Lång 2000). Additionally, heavy mineral assemblages hold information about their depositional environment and processes and their stratigraphic position (Marcinkowski and Mycielska-Dowgiałło 2013). This thesis is not only focusing on loess but also incorporates the soil parent material. Hence, the underlying substrate is the framework of the developing soil profile and is important to understand soil patterns (Schaetzl and Anderson 2005).

The province lower Silesia in southwestern Poland is characterized by reworked loess deposits. Previous studies in the region have investigated how the incorporation of aeolian silt to regoliths/soils led to clay translocation and to the formation of Alisols, Luvisols and Leptosols (Waroszewski et al. 2017). Additional studies conducted in Poland investigated the clay mineralogy of loess soils near Krakow (Drewnik et al. 2014) or investigated the heavy mineral assemblage of quaternary deposits in central Poland (Marcinkowski and Mycielska-Dowgiałło 2013).

However, little is known about the interaction of different underlying substrates with loess mantles and their contribution to soil development. Especially, the clay and heavy mineralogy of such soils have not been studied/modelled so far. Additionally, it is still a matter of debate where the reworked loess deposits in lower Silesia originated. Therefore, the main research questions for this master's thesis are

- What influence do the underlying bedrock and the loess mantle have on soil development and soil processes in the different profiles? Can the formation and/or transformation of the phyllosilicates be observed?
- Are the discontinuities found in the soil texture and the soil geomorphology also reflected in the clay and heavy mineral distribution and in the physical and geochemical parameters in the five profiles?
- What are the origins of the loess mantles at the five different sites? Do they originate from the same source?

Consequentially, an influence from the underlying substrate and loess mantle on the soil development and on soil processes is expected. This influence is assumed to be reflected in the clay and heavy mineralogy and thus in other parameters.

Regarding the provenance of the loess mantles: One hypothesis is that the loess mantles were deposited in the Lower Silesia region during the LGM when vegetation cover in the region was scarce and Therefore an increased aeolian transportation occurred and formed the northern loess belt. Another hypothesis is that loess was deposited in the Great Odra Valley by being transported by wind from the strongly denuded mountain areas in the South.

This thesis is divided into the following chapters: first an overview about the background is given and the study sites are described. Then the methods are described and the results presented. Finally, an interpretation and discussion chapter followed by the conclusion constitute the last part of the thesis.

# 3. Theory

## 3.1 Clay minerals

Clay minerals are silicate minerals. The definition of a mineral is a naturally occurring, inorganic solid that has an ordered atomic arrangement and specific, although not fixed, chemical composition. Soil minerals are divided into primary and secondary minerals. The primary develop from a physical breakdown of igneous and metamorphic rocks and are mainly part of the sand and silt fraction. The secondary minerals that can be found in the clay fraction are formed under low-temperature weathering reactions. They originate from sedimentary rocks but are more commonly transformed from primary minerals or form directly in the soil. Common secondary minerals in soils are phyllosilicates, aluminium and iron oxides, carbonates, phosphates and sulphate minerals (Strawn et al. 2015). In the next section phyllosilicates are looked at in detail.
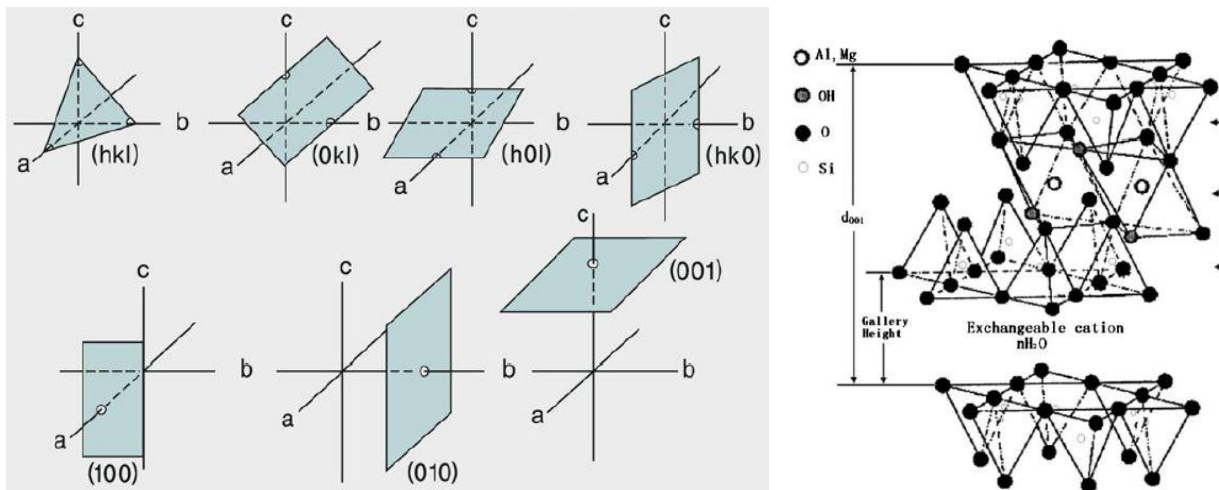


**Figure 1:** Miller indices given for important planes (left) and the structure of 2:1 smectite including the d-spacing showed in the right image (source: Okrush and Matthes 2014 (left) and Chen et al. 2008 (right)).

The structure of phyllosilicates can be understood by looking closely at the basics of mineralogy where all direction and planes in a mineral are referenced to a crystallographic coordinate system which is based on the unit cell of a mineral (Smith College 2018). The unit cell is described as the smallest set of atoms in the crystal structure. It contains a complete sample of the crystal pattern that is repeated in space to form the mineral (Schaetzl and Anderson 2005). Miller indices are used to identify rational planes in crystals. They are determined for any plane from the intersection of the plane with the crystallographic axes. Further, when one or more axis intercept is unspecified, the letters h,k and l are used for the unspecified a, b and c indices, respectively (see Figure 1). Consequently, the general Miller index is labelled: (hkl) (Smith College 2018).

Phyllosilicates are constructed by superposed atomic planes parallel to the (001) face. These periodic, repeating planes of atoms of the minerals are characterized by uniform distances between the planes, the so-called d-spacing.

Thus, the d-spacing is characteristic of the layer type and the interlayer material. The planes of the phyllosilicates are constructed from tetrahedral ($Si_2O_5^{2-}$ silica) or octahedral sheets (($AlOH$)$_3$) (see Figure 1, right). The 1:1 phyllosilicates are characterized by one silica tetrahedral sheet bonded to one octahedral sheet.

Therefore, the unit cell consists of one tetrahedral and one octahedral sheet. Examples for 1:1 layer silicates are minerals of the kaolinite and the serpentine group. The 2:1 phyllosilicates, on the contrary, contain two $Si_2O_5^{2-}$ tetrahedral sheets sandwiching an ($AlOH$)$_3$ octahedral sheet and can be classified according to the type of the octahedral sheet (Schaetzl and Anderson 2005). "Octahedral sheets that contain predominantly trivalent cations such as $Al^{3+}$ or $Fe^{3+}$ are called "dioctahedral sheets" because only two out of every three of the octahedral sites are filled" (Schaetzl and Anderson 2005, p. 65). Divalent cations like $Mg^{2+}$ or $Fe^{2+}$ can occupy all three octahedral sites. Muscovite, illite and glauconite are examples for minerals with a dioctahedral sheet type. Examples for trioctahedral minerals are for instance: talc, chlorite and biotite. Vermiculite and smectite can have both types of octahedral sheets (Schaetzl and Anderson 2005). Additionally, mixed layer minerals such as crystallites composed of two or more types of basic structural layers exist. The mixed layer minerals typically occur in soils or the upper parts of an alteration sequence. Their importance is poorly understood until now, but Velde and Meunier (2008) see them as the key to understand clay mineral stability in many soils. Examples of dioctahedral species of mixed layer minerals are illite/smectite or kaolinite/smectite. Trioctahedral species observed at the earth's surface are for example biotite-vermiculite or chlorite-vermiculite (Velde and Meunier 2008). Mixed layer clay minerals can have a regular or irregular interstratification.

The 2:1 layer silicates (vermiculite or smectite) can host extensive metal hydroxide polymers in the interlayer region and thereby hydroxy-interlayered vermiculite (HIV) and hydroxy-interlayered smectite (HIS) are distinguished. They encompass vermiculite or smectite with positively charged $Al^{3+}$ or $Fe^{3+}$ hydroxide polymers in the interlayers.

An important process taking place in phyllosilicates is the isomorphous substitution where one ion is replaced by another ion of similar charge and radius. Thereby, the crystal form does not alter. In clays typically lower valence cations are substituted for higher valence cations, for example, $Al^{3+}$ for $Si^{4+}$ in tetrahedral sheets or $Mg^{2+}$ for $Al^{3+}$ or $Fe^{3+}$ in octahedral sheets. Normally, isomorphous substitution is important in 2:1 clays. In these clays the created layer charge is neutralized by cations through absorption between two adjacent 2:1 phyllosilicate layers. 1:1 clays, on the contrary, have negligible isomorphous substitution (Schaetzl and Anderson 2005).

Due to their physical, chemical and mineralogical properties, clay-rich materials are important to support agricultural and natural ecosystem productivity (Catt 2001).

## 3.2 Clay minerals in soils

Velde and Meunier (2008) describe for the A horizon that the clays are primarily the result of plant/ clay interaction. The A horizon might be affected by physical erosion and, Therefore, it is the most fragile one. Hence, clay minerals may move upwards with time from lower horizons to the surface horizon due to erosion (Velde and Meunier 2008).

The E horizon, a light-colored mineral horizon, shows evidence of losses of clay, oxides, iron and aluminum and organic matter to greater depths. This downward translocation is mainly caused by infiltrating water. A and E horizons are zones within the soil profile where eluviation is dominating. B horizons, on the contrary, show higher evidence of illuviation. The illuviated material might include clay as well as iron, aluminum, carbonates, sodium, humus, gypsum, sulfur and silica (Schaetzl and Anderson 2005). In addition, the B horizon is a transit zone where clays from the C horizon move upwards by erosion. Therefore, the B horizon is a zone where clays from the surface and from the subsurface are mixed. Soils can develop on all sorts of geological materials: sand dunes, sediments like sand or till, sedimentary or eruptive rocks. Thus, the transformation from source material to soil is diverse. The main characteristics of the C horizon are the dissolution of material and its transportation out of the system (Velde and Meunier 2008). Weathering occurs when rocks or minerals alter physically and chemically at or near the Earth's surface, driven by biological, chemical and physical agents or their combination (Pope et al. 2002). The formative environment of rocks like - the sea floor or the crust - differs strongly from the surface (soil) environment. There, less pressure and increased amounts of oxygen, water and biota occur. Thus, primary minerals from the formative environment are unstable in soils and weather to secondary minerals, mainly clay minerals (Schaetzl and Anderson 2005). Velde (1995) states that the weathering of rocks and pedogenesis are the major processes for clay mineral formation. This formation occurring at Earth's surface is governed by a limited number of variables: rock composition, water/rock ratio, temperature and time. To conclude, the C horizon is dominated by minerals stable under conditions of interactions of surface aqueous solution and unstable high temperature minerals. The formation of clay minerals depends strongly on the environment and the bedrock (Velde and Meunier 2008).

## 3.3 Loess in Europe

The term loess originates from the German word 'Löss' and means loose. It was first described by von Leonhard (1823-4) for silty deposits along the Rhine Valley near Heidelberg (Pye 1995; Leonhard 1823). In the field loess can be recognized as a distinctive sedimentary body whose thickness is highly variable. It can range from a few centimetres to several hundred meters. Additionally, loess is very fertile and thus suitable for agricultural purposes but strongly susceptible to erosion. Furthermore, it is an important archive of Quaternary climate change.

Thus, loess is an important tool for the reconstruction of paleoclimatology over millennial timescales (Muhs 2013). Loess covers more than 10 % of the land's surface, mainly in the temperate zone (Sprafke and Obreht 2016; Pye 1995; Pécsi and Richter 1996; Muhs, D.R., Bettis III, E.A. 2003).

Pye (1995) defines loess as terrestrial clastic sediment, which predominately consists of silt-sized particles. The silt content in loess is usually 60-90 %.

Thereby, the particles have a diameter between 50 and 2 µm. The sand (> 50 µm) and the clay ( < 2 µm) contents are usually smaller (Muhs 2013). Globally, loess exhibits significant natural variation in terms of thickness, grain size, color, mineralogy, geochemical composition and morphology (Smalley and Vita-Finzi 1968).

Even though the common definition of loess is quite clear, the understanding of the formation of loess depends strongly on the researcher's background and how loess is classified in certain research fields: as a sediment, rock or soil (Sprafke and Obreht 2016).

The formation of loess is seen as a result of accumulation of wind-blown dust. Therefore, some conditions must exist for its formation: a sustained source of dust, adequate wind energy for transportation and a suitable accumulation site (Pye 1995). Muhs (2013) states that fine-grained particles are produced by both glacial and non-glacial processes. Firstly, the silt production occurs by frost shattering and by glacial grinding in periglacial regions. Silt can also be produced by volcanoes through the ejection of ash or through fluvial comminution. These two processes occur in both glacial and non-glacial environments. Secondly, non-glacial processes occur in high altitudes when silt is produced by frost shattering or when silt is inherited from siltstone bedrock. In deserts, silt results from salt weathering or from aeolian abrasion in dune fields. The silt is then transported by wind in suspension. Further silt production by aeolian abrasion is possible (Muhs 2013).

After deposition, most loess has been modified due to local reworking, bioturbation, syn-depositional weathering and pedogenesis (Pye 1995). The term loessification describes the quasi-pedogenic/quasi-diagenic processes whereby the aeolian deposits are aggregated (Sprafke and Obreht 2016). Sprafke and Obreht (2016) see loessification as the crucial element of loess genesis which provides the deposits with their important characteristics.
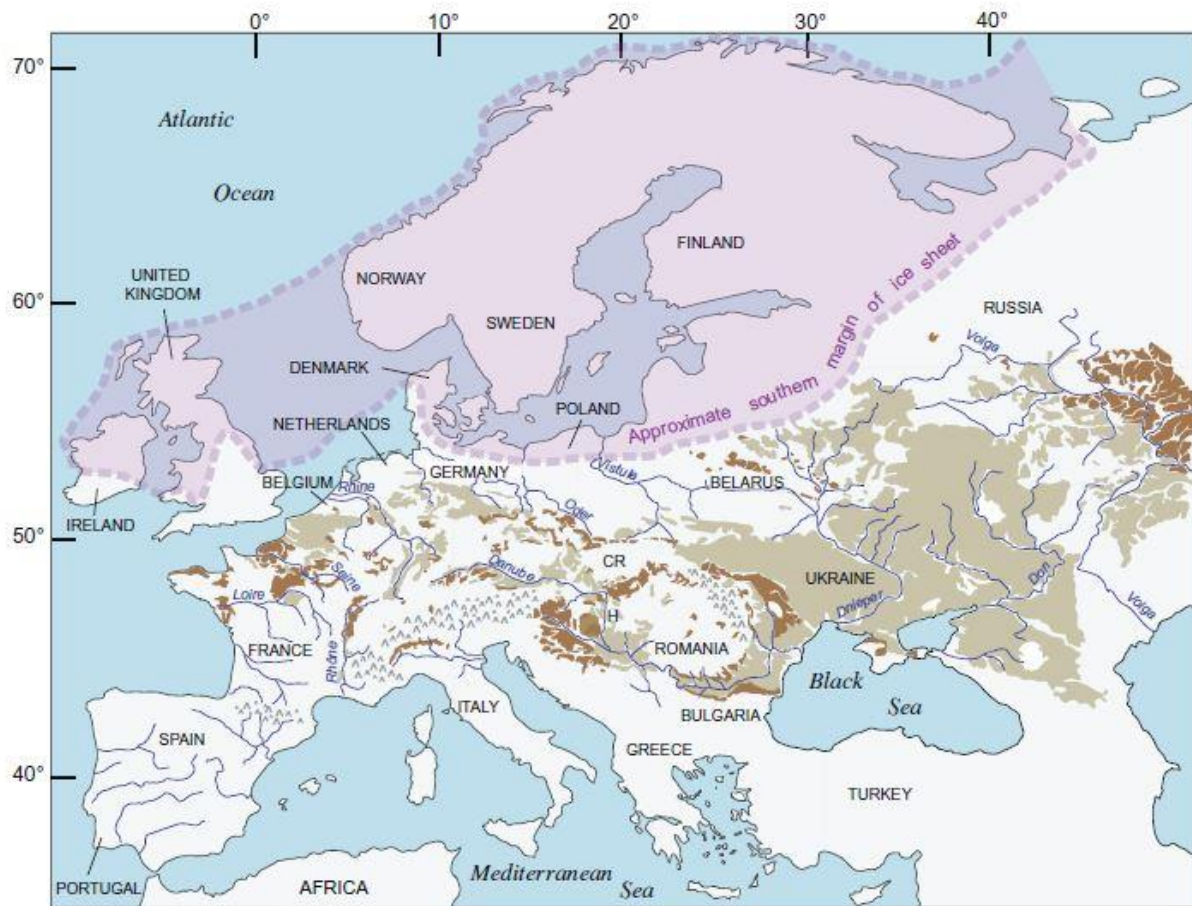
**Figure 2**: Loess deposits (thick, thin and sandy loess = brown) and loess derivates (light brown) in Europe (from Haase et al. 2007). The southern margin of the Scandinavian ice sheet of the Last Glacial Maximum is displayed in purple (from Flint 1971) (source: Muh 2013).

In Europe, loess deposits (see Figure 2) range from the north-western maritime regions (France, Belgium) over Central Europe to the Ukraine and the Russian plains, which are characterized by a continental climate. These deposits are the product of the quaternary glacial period in Europe, mainly the Weichselian period (Haase et al. 2007). The European loess and loess-derived sediments formed during the quaternary under two main conditions. Firstly, under periglacial condition in mid-continental areas beyond the limits of major ice sheets and secondly, peri-montane regions along the margins of high mountain ranges (Pye 1995). Loess covers approximately one fifth of the total surface of Europe and due to their widespread distribution, they are an excellent object for scientific studies in fields such as quaternary geology and soil science (Haase et al. 2007). Grahmann (1932) subdivided Europe into four main areas of loess distribution. Firstly, there is a continuous belt north of the mountainous regions of Europe. Secondly, loess covers are found in the northern foreland of the Alps in the central and lower course of the Danube River.

Thirdly, one of the main areas is the great East European platform and its bordering lowlands. Finally, the last main area exists in small basins and river valleys in the lower parts of the "Old Central European Mountains" (Grahmann 1932). Most loess in Europe is deposited in Eastern Europe, Russia and the former Soviet Union.

This region is limited in the south by the Black Sea and the Caucasian Mountains and in the northeast by the marginal moraines of the Valdaj glaciation (Haase et al. 2007). The most important areas influenced by loess in middle Europe are along the rivers Weichsel, Oder, Elbe and Main (Pécsi and Richter 1996). Flint (1971) describes the large river systems as the main mechanism for carrying outwash material from the glacial terrains. This outwash material provides the bulk material of the central European loess. As an example, the Danube River carried and spread outwash material from glaciers in the Alps and the Carpathian Mountains across southeastern Europe (Flint 1971).

**3.4 Last Glacial Maximum and loess deposits in southwestern Poland**

In southwestern Poland considerable deposits of loess are found. In Lower Silesia thick and thin loess deposits are distinguished. The former have a thickness between 0.3 to 2 m, whereas the thick covers are in most cases 3-5 m and sometimes reach a thickness up to 15 m (Jary and Ciszek 2013; Jary 1999). The deposits seem to originate from the Pleistocene glaciations of northern Poland but are also associated with the Carpathian and Sudetes mountains in the South.

The youngest Scandinavian glaciation during the LGM (see Figure 2) in Poland is also known as the 'Weichsel`glaciation, named after the polish river Wisla (Keilhack 1899). It can be subdivided into three main phases: the Leszno, Pozan and Pomerian phases (Woldstedt 1931). Marks (2002) emphasizes that the ice sheet limit during the LGM was not synchronous throughout Poland but rather consists of several major and minor ice lobes. These lobes reflect the stream-like structure of the ice body that radiated southwards from the Baltic Basin. The meltwater runoff during the LGM created a complex system of ice-marginal spillways and southward flowing meltwater valleys (Marks 2002; Kozarski 1988). At the Odra Bank the LGM occurred after 21 ka BP according to radiocarbon data from this region (Kramarska 1998; Kozarski 1981). Bridges and Muhs (2012) state that during glacial times winds may have been stronger, many regions more arid, the vegetation cover reduced, the hydrological cycle less intense and the dust supplies increased (Bridges and Muhs 2012). Hence, the LGM world was colder, drier, less vegetated and far dustier. Thus, the loess is a direct result of glaciogenic silt production from expanded continental ice sheets, mountain ice caps and valley glaciers (Muhs 2013).

Smalley and Leach (1978) saw the northern glaciers as producers of loess material in southwestern Poland. Certainly, they showed that the European loess belts are related to the Danube, Rhine and their tributaries, but because a major river valley was missing in the region, the loess mantles were not associated with a river.

Rather, it was believed that the loess originated as silt deflations from outwash planes and glacial till deposits in front of the LGM (Smalley and Leach 1978; Haase et al. 2007; Jary and Kida 2000). Badura et al. (2013) questioned this theory of the origin of the loess deposits and suggested that the so-called "Great Odra Valley" and the mountains in the South played an important role. The "Great Odra Valley" is described as the fossil form of the present-day Odra-valley where the fluvioglacial water ran along the Wroclaw-Magdeburg-Bremen ice-marginal valley. Fine, silty material coming from the Sudetes and the morainic hills fed the valley and accumulated parallel to the prevailing wind directions heading towards the South and Southeast. The deposited silt material was later redeposited by winds (Badura et al. 2013; Badura 2011, 2006).

# 4. Study site

## 4. 1 Geography

The study site is located in the southwestern part of Poland, in the province of Lower Silesia (see Figure 3). Lower Silesia shares borders with Germany in the West, Czech Republic in the South, the Lubusz and Greater Poland province in the North and the Opole province in the East (Nationsonline 2018). The capital of Lower Silesia is Wroclaw and lays on the banks of the Odra River in the East.
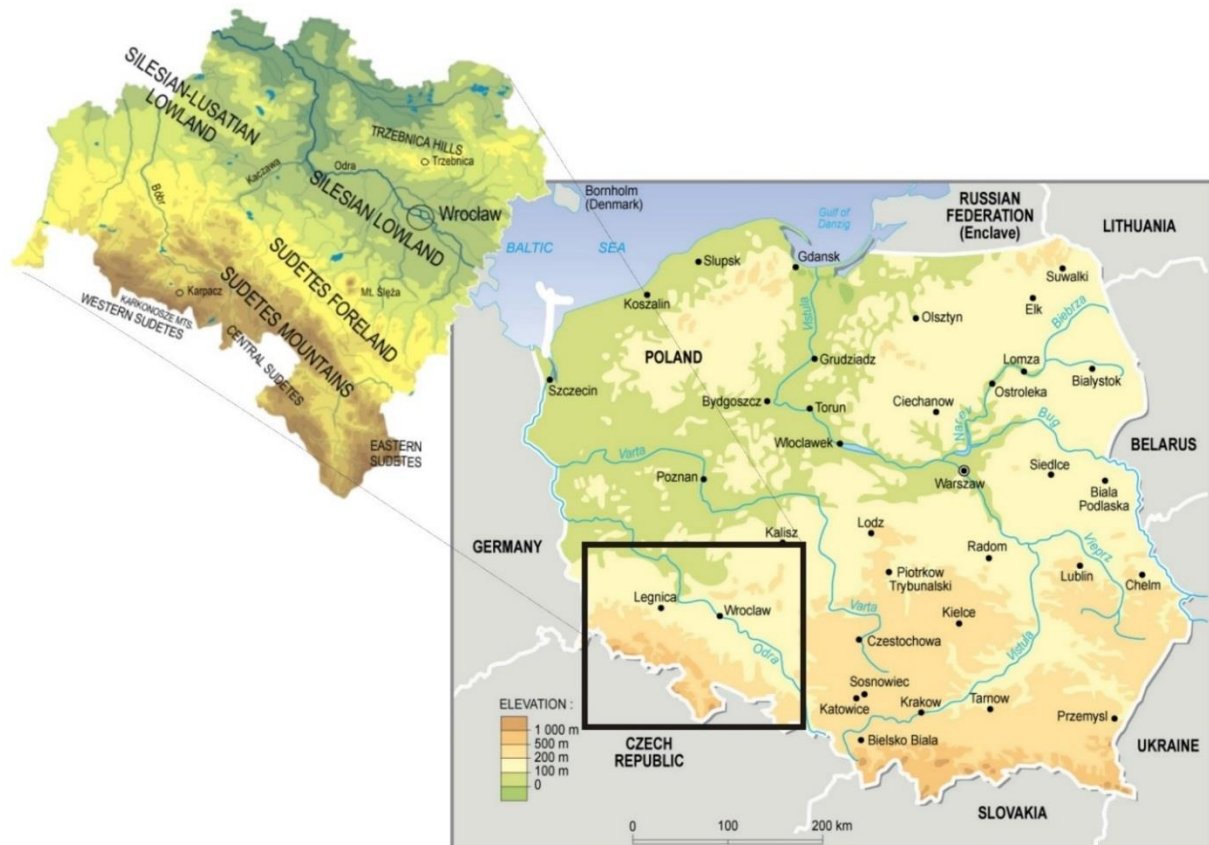


**Figure 3:** The location of Lower Silesia in Poland (on the right) and the topographical subregion of the province (Sources: mapsland 2018 (right) and karnet 2018 (left)).

Regarding the topography, around 2/3 of Lower Silesia is lowland whereas around 1/3 are part of a low mountain range in the Southwest. The lowlands are characterized by glacial landforms, which developed during the Pleistocene. In the North and West fragments of the former ice-marginal valleys (Warsaw-Berlin, Baruth-Glogow, Wroclaw-Magdeburg) are found, which reflect important hydrographic networks during the LGM (Kosmala 2015).

The Silesian Lowlands are separated from the North by the Trzebnickie Hills which are a range of moraine hills. These were formed during the Warta glaciation which occurred during MIS 6 (Rdzany 2009; Kabała et al. 2015).

Generally, moraines and outwash material are spread in the region and the hills in the lowland are covered with loess deposits. North of the Trzebnickie Hills the Milicz-Glogow Basin is located. The basin is a latitudinal belt of depressions which has a glacial valley character.

This region is also shaped by the Odra River in the middle part and the Barycz Rivers in the East. The Silesian Lowland is a vast plain with almost no diversity regarding the relief. The lowland runs from the Southeast to the Northwest, along the glacial valley of the Odra. The valleys are filled with alluvial sediments, mostly sand and gravel of Pleistocene- and Holocene age (Kabała et al. 2015). The lowland shows further glacial remains like moraine hills or eskers, which are long, narrow, winding ridges composed of stratified sand and gravel and deposited by a meltwater stream. Other characteristic remains are kames, which are mound like hills of poorly sorted drift and which were deposited near the terminus of a glacier (Britannica 2018a, 2018b, (Kabała et al. 2015). Lower Silesia has a great diversity regarding the landforms shaped by rivers and glaciers but those landforms are also the result of complex geological structures (Kosmala 2015).

## 4.2 Geology

The mountains in the Southwest are characterized by a belt system mainly due to its specific geology. Not only orographic movements shaped the landform, also the influence of the ice sheets was predominant. The Sudetic Marginal Fault divides the crystalline massif into two parts: the Sudety and the Fore-Sudetic Blocks. This Fault is one of the major tectonic structures in southwestern Poland. The visible morphotectonic escarpment is 200 km long and runs from the Southeast to the Northwest (see Figure 4). It clearly divides the lowland, which is mainly built up from sedimentary deposits, from the mountains (Kabała et al. 2015).
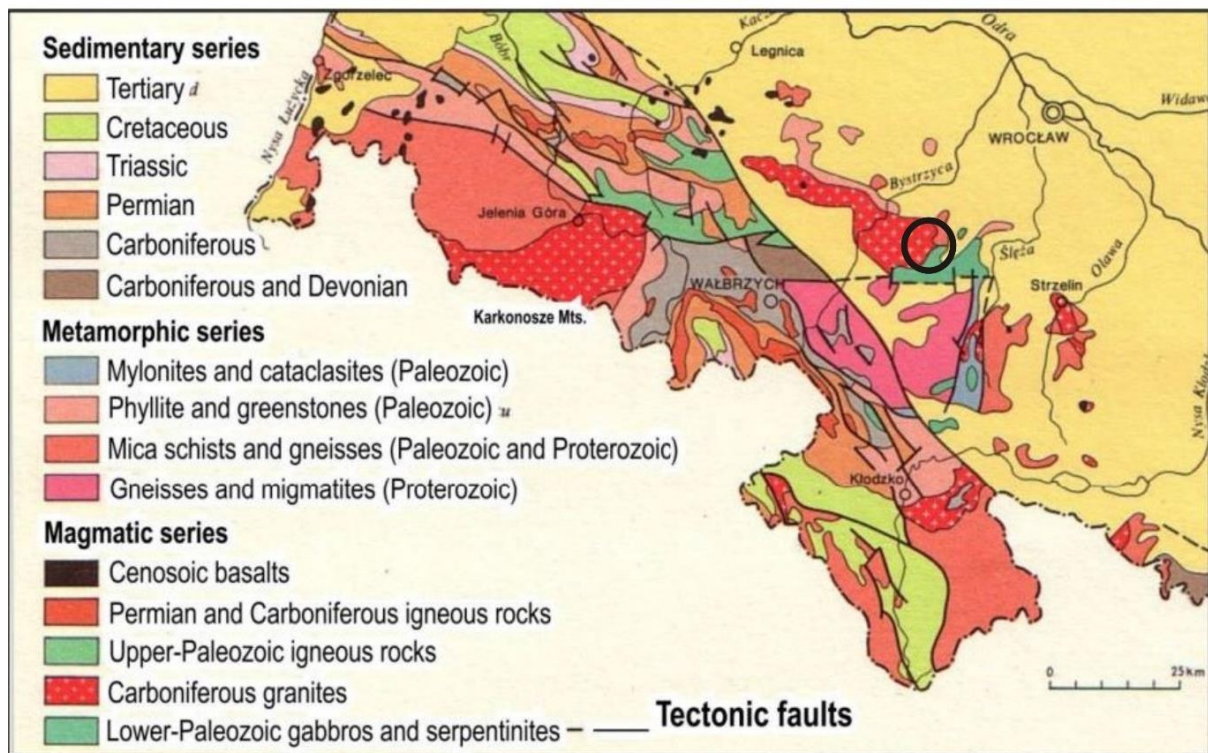
**Figure 4:** Geological map of Lower Silesia showing the sedimentary, metamorphic and magmatic series (source: (Kabała et al. 2015).

Mt. Ślęża, the northern most outreach of the Fore-Sudetic Block is an isolated mountain massif in the middle of the flat Silesian lowland (see Figure 4, encircled). Mt. Ślęża is surrounded by thin and scatterd loess-derived deposits (Waroszewski et al. 2017). The isolated mountain is subdivided into two geological units. The first is the Ślęża ophiolite, which is characterized by ultrabasic rocks like metagabbros, serpentinitzed peridotites, pyroxene- and amphibole-rich rocks or metabasalts (Kierczak et al. 2016; Kryza and Pin 2010). The second unit is the Strzegom-Sobótka Massif, which hosts Variscinian granitoids (Waroszewski et al. 2017). These bedrocks are covered with Miocene sea sediments and Quaternary sands and moraine clays. Furthermore, large areas of the region show loess mantles and deposits of fluvioglacial silt (Kabała et al. 2015).

The Sudety Mountains are built up from different crystalline and sedimentary rocks, mainly granites, gneisses, amphibolites, crystalline schists and other rocks of Paleozoic age. Partially, Tertiary basalts traverse the older rocks. The Kłodzko basin (see also Figure 4) near the Central Sudety Mountains is filled with Devonian, Carboniferous and Permian sediments and covered with several hundred meters of sandstone. The Western Sudety Mountains provide a great orographic diversity, hosting for example the Karkonosze Mountains (see also Figure 4). The latter consist of carboniferous granites and are surrounded by a series of metamorphic rocks in the East and magmatic series in the North around Jelenia Gora.

16

## 4.3 Soils

In Lower Silesia, four sub-regions can be distinguished based on their dominant soil texture. The first one lays in southwestern Poland and includes the Sudety Mountains. Its northern border runs along the main tectonic fault. About 65 % of the area is covered by loamy-textured soils and 28 % by silt-textured soils. The central sub-region which incorporates the Sudety Foreland and the Silesian Lowland south of the Odra valley is part of the "loess belt". The region is characterized by silt-textured soils (74 % of the area). The third sub-region lays in the Northwest and is dominated by sandy soils (around 84 % of the area) whereas the sub-region in the Northeast the textural diversity is relatively large. Regarding the topsoil a huge sand cover dominates the northwestern part, around 62 %. In contrast, the subsoil exhibits a higher variability in this sub-region. The major soil types in Lower Silesia from a general perspective are: Luvisols, Retisols, Alisols, Stagnosols and Planosols (IUSS Working Group 2015). These soils are characterized by subsurface illuvial clay accumulation and cover around 35 % of the province. Cambisols are the second most prevalent with around 18 %, whereas alluvial soils like Fluvic Cambiols or Fluvic Phaeozems (with 12.9 %) or rustic soils like Brunic Arenosols (with 12.2 %) are also quite frequent (Kabała et al. 2015).

## 4.4 Climate and Vegetation
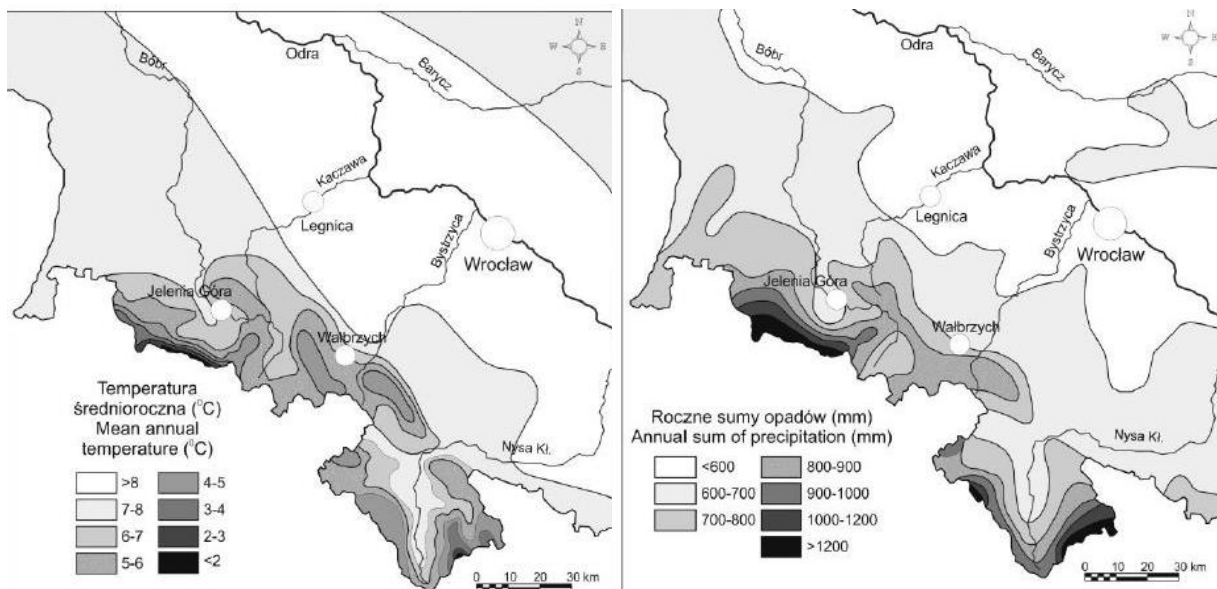


**Figure 5:** Mean annual temperature (°C) (left) and mean annual precipitation (mm)(right) in Lower Silesia (source: (Kabała et al. 2015).

Lower Silesia is situated in the temperate zone but shows transitional characteristics between maritime and continental climate. The weather is quite variable due to occasional inflows of arctic or tropical air masses during the year. Moreover, the weather is influenced by the land topography. The diversity of altitudes, ranging from the sea level up to 1'603 m a.s.l., and the variety of the relief have an impact on the weather.

The mean annual precipitation rises with increasing altitude above sea level (see Figure 5, right side). Highest mean precipitation is found in the Karkonosze Mountains with 1'371 mm/ year. The lowest mean precipitation with < 600 mm/ year occurs in the northern part of Lower Silesia. The highest mean annual temperatures (see Figure 5, left side) are found in the Silesian – Lusatian Lowlands and the Silesian Lowland. Examples are Legnica with 8.8°C or Wroclaw with 8.7°C where also the longest growing seasons occur (230 days per year). The lowest mean annual temperatures are found in the mountains on Mt. Sniezka (0.6°C) (Kabała et al. 2015). Generally, the average annual precipitation in Lower Silesia is between 600-700 mm. Together with the mean annual temperature of 8°C, they are favorable for the vegetation. Large forests, which are mainly coniferous, are found on podzolic and luvisolic soils. Kosmala (2015) hints that in the mountain region several vegetation zones are found. The lower subalpine forest zone (400-1'000 m a.s.l.) is represented by beech forests while the upper subalpine forest zone (1'000-1'300 m a.s.l.) is natural spruce forest. In the subalpine zone (1'250-1'500 m a.s.l.) found in the Karkonosze Mountains, the Snieznik Massif and the High Jesenik, dwarf mountain pines are dominating (Kosmala 2015).

## 4.5 Profile description
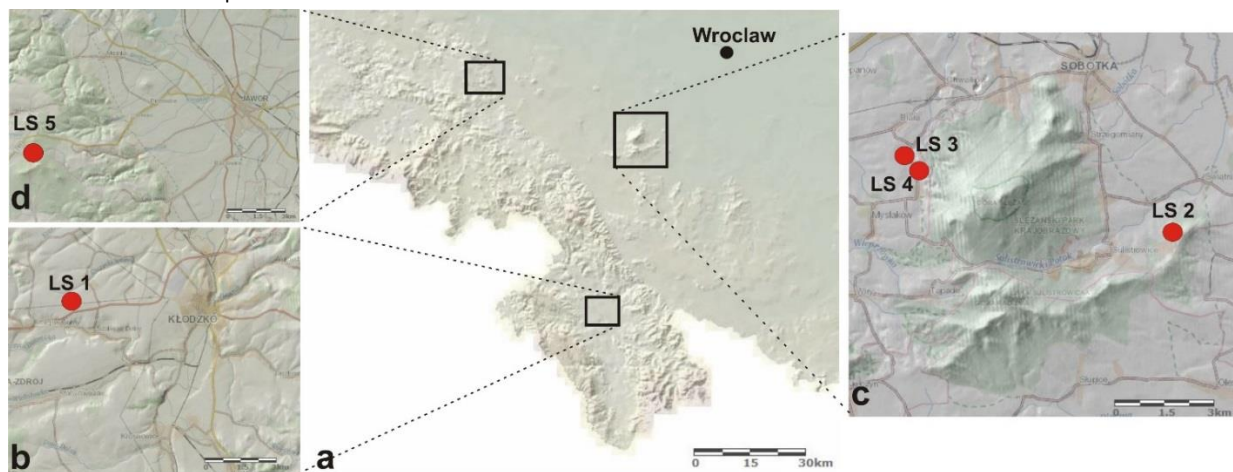


**Figure 6:** Location of the investigated profiles in Lower Silesia (a): LS1 near Kłodzko (b); LS2, LS3 and LS4 settled around Mt. Ślęża and LS5 west of Jawor (Source: mapy geoportal 2018, modified).

All investigated profiles lay either in the Silesian Lowland or near the Central Sudetes in the Kłodzko Basin. An overview is shown in Figure 6, a. Profile LS1 is situated on arable land west of the town Kłodzko (see Figure 6, b) in the southern part of Lower Silesia, close to the Czech boarder. The underlying bedrock is Permian sandstone. Profile LS2, which has serpentinite slope deposit as underlying substrate, is situated east of Mt. Ślęża (718 m.a.s.l). LS3 (on granite regolith) and LS4 (on fluvio-glacial deposits) lay west of Mt. Ślęża (see Figure 6, c). The last profile LS5 (on basalt slope deposits) is situated southwest of Wroclaw near the town Jawor (Figure 6, d).

All investigated soils reveal clear aeolian silt admixture reflected in a loess mantle which is transitionally or abruptly separated from the local bedrock. Additional details for all profiles can be found in Table 1 and in the appendix (from page 72). Details about the soil morphology like structure, consistence (moist), the horizon boundary and the diagnosistcs and color (moist) are found in Table 2, page 24.

**Table 1**: Additional information for the study site of each profile.

| Soil profile | Elevation (m a.s.l.) | Latitudes/ Longitudes | Position in landscape | Exposure | Slope (°) | Geological substrates | Present land use | Soil type WRB (2015) |
|---|---|---|---|---|---|---|---|---|
| LS1 | 529 | 50°26'05.4''N, 16°34'24.3''E. | Shoulder | NE | 5 | loess/ Permian sandstone | arable land | Endoskeletic Luvisol (Episiltic, Raptic) |
| LS2 | 250 | 50°51'20.0''N, 16°46'55.3'E. | Midslope | NW | 12 | loess/ serpentinite | Forest | Endoskeletic Luvisol (Magnesic, Raptic) |
| LS3 | 260 | 50°52'35.0''N, 16°40'09.1''E. | summit/ shoulder | NE | 2 | loess/ granite | Forest | Katoskeletic Alisol (Raptic) |
| LS4 | 230 | 50°52'24.6''N, 16°40'09.1''E. | summit/ shoulder | NE | 3 | loess/ glacio-fluvial deposits | Grassland | Endoskeletic Luvisol (Episiltic, Endoloamic, Raptic) |
| LS5 | 402 | 51°01'10''N, 16°01'40''E. | backslope | NW | 8 | loess/ basalt slope cover | Forest | Eutric Luvic Albic Folic Stagnosol (Anosiltic, Ochric,) |

In LS1 in total five horizons were defined, see Figure 7 on the left side. The soil type according to WRB is Endoskeletic Luvisol (Episilitic, Raptic). The loess mantle has a thickness of 48 cm. For this study, the horizon AE was taken as example for the loess mantle. The 2Btg2/E horizon reflects the transition horizon and 3BC the bedrock (Permian sandstone). AE horizon exists in a depth between 18 and 45 cm, the 2Btg2/E horizon from 78 to 95 cm and 3BC horizon from 95 to 112 cm.
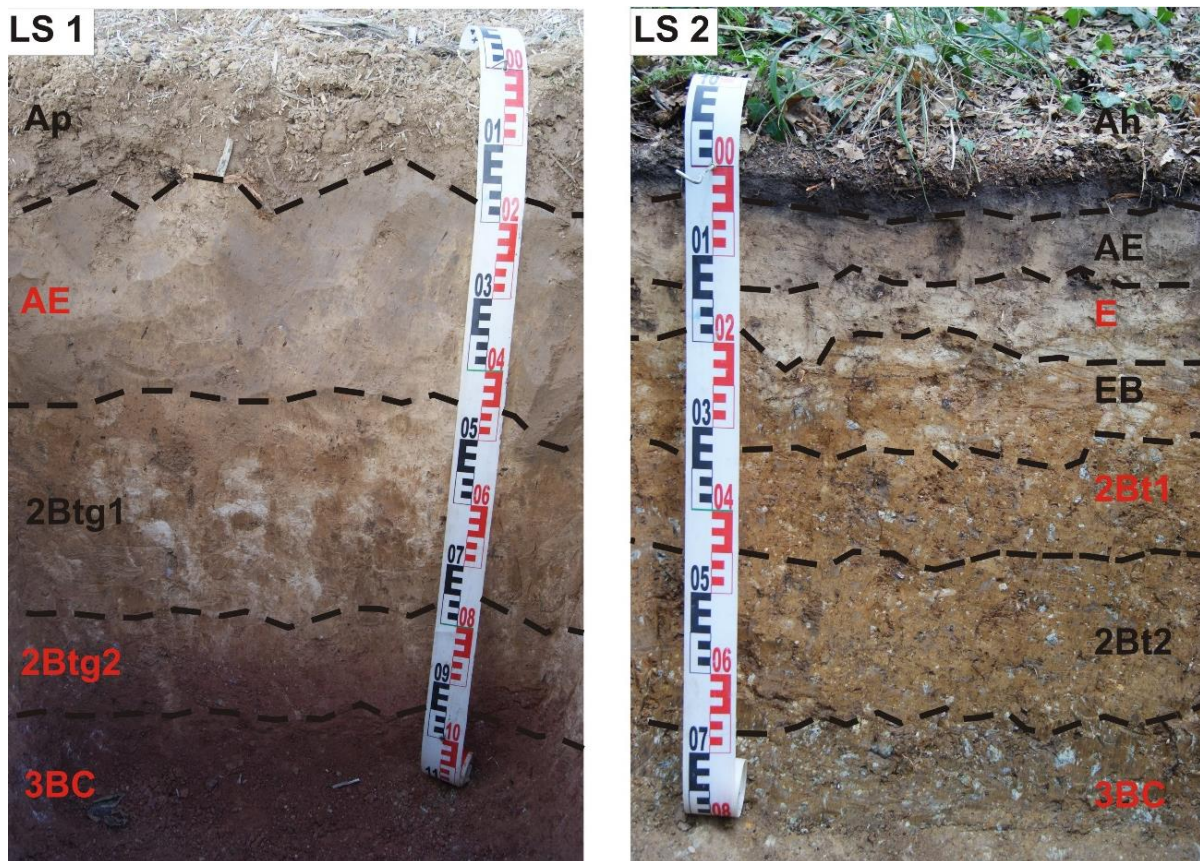
**Figure 7:** Soil profiles of LS1 (on Permian sandstone) and LS2 (on serpentinite). The investigated horizons are shown in red (J. Waroszewski).

Profile LS2 is situated on a midslope in a forest on serpentinite slope sediments and shows characteristics of an Endoskeletic Luvisol (Magnesic, Raptic). In total seven horizons were identified (see Figure 7, right). The loess mantle occurred from 4 to 33 cm, whereby the E horizon (14-19 cm) was taken as represented sample. The transition zone occurred between 33 and 68 cm, while the underlying serpentinite strata was identified as 3BC from 68 to 86 cm (maximum depth of the profile). The horizon 2Bt1 between 33 and 45 cm reflects the transition horizon. The transition horizon of LS2 is skeletal and shows coarse rock fragments up to 19 cm.

The third profile LS3, which lays on granite, is situated on a summit/shoulder in a forest. The soil type according to WRB (2015) is a Katoskeletic Alisol (Raptic). The profile reached a depth of 130 cm and totally seven horizons were defined (see Figure 8, left). The loess mantle was identified from the soil surface down to 30 cm. The transition zone occurred from 30 to 70 cm, which was characterized by coarse rock fragments. The underlying material in this profile was detected from 70 to 130 cm. Following horizons were further analyzed in this thesis: the Bw(t) horizon (8-30 cm), the 2BC horizon (50-70 cm) and the 3BC (70-110 cm).
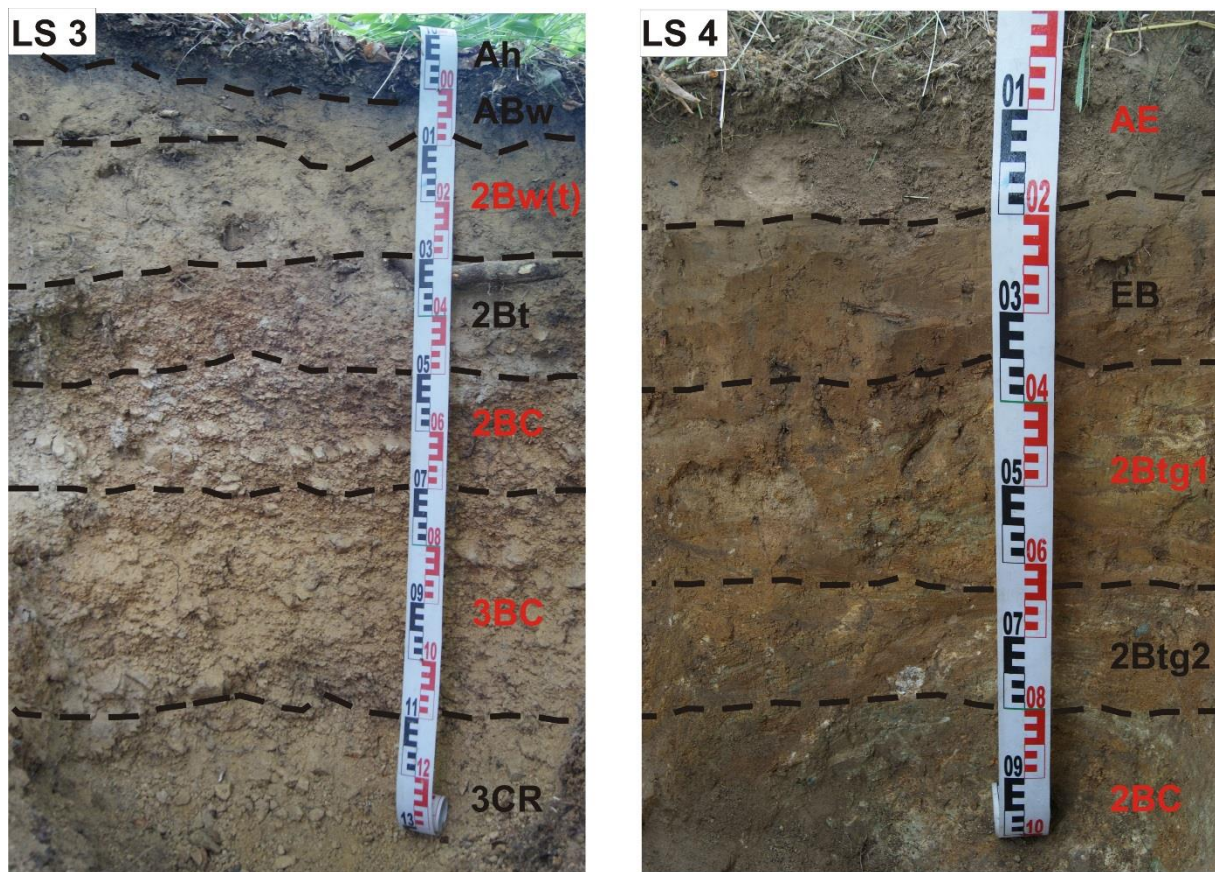
**Figure 8:** Horizons of LS3 (on granite) and LS4 (on glacio-fluvial material). The red labelled horizons were investigated (J. Waroszewski).

The profile LS4 is characterized by glacio-fluvial deposits as underlying material. It is situated on a summit/shoulder on grassland (soil type: Endoskeletic Luvisol (Episilitic, Endoloamic, Raptic)). The profile reached a depth of 105 cm and was divided into five horizons (see Figure 8, right). The loess mantle has a thickness of 36 cm and the AE horizon (0-20 cm) Therefore is the representative horizon. Samples of the 2Btg1 horizon (36-64 cm) were described as transition horizon. The horizon 2BC between 81 and 105 cm reflected the features of the underlying substrate.
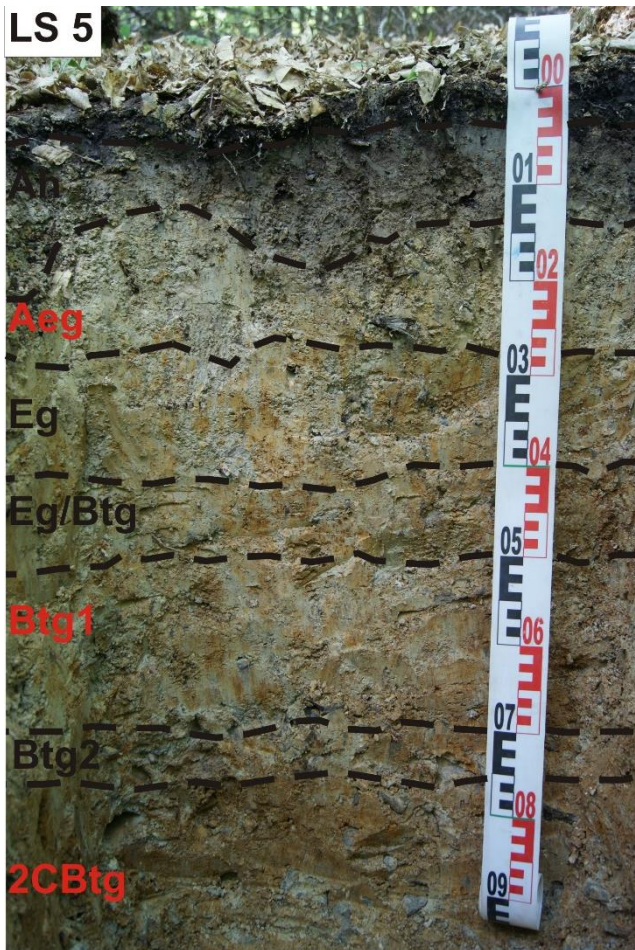
**Figure 9:** Horizons of profile LS5 laying on basalt (J. Waroszewski).

The last profile (LS5) is settled on a backslope in a forest on basaltic bedrock. Its soil type is an Eutric Luvic Albic Folic Stagnosol (Anosilitic, Ochric). The profile was divided into seven horizons and reached a maximum depth of 100 cm (see Figure 9). The loess mantle occurred between 4 and 28 cm while the transition zone was identified between 28 and 70 cm. The last 30 cm represent the residuum material (2CBtg horizon). The loess mantle is represented by the AEg horizon (4-14 cm), while the Btg1 horizon between 40-50 cm reflects the transition horizon.

**Table 2:** Soil morphology of the investigated profiles.

| Profile | Horizon | Depth (cm) | Color (moist) | Redox features | Structure | Consistence (moist) | Horizon boundary | Diagnostics |
|---------|---------|-----------|---------------|----------------|-----------|---------------------|------------------|-------------|
| LS1 | AE | 18-45 | 10YR 5/4 | - | sb, fi | fr | g,w | |
| | 2Btg2/E | 78-95 | 10YR 6/4 | - | ab/pl, fi | fi | c | argic |
| | 3BC | 95-112 | 2.5YR 4/5 | - | ab, fi | vfi | | |
| LS2 | E | 14-19 | 10YR 8/2 | - | ab, vfi | fr | g | albic |
| | 2Bt1 | 33-45 | 10YR 4/6 | - | ab, fi/m | fi | g | argic |
| | 3BC | 68-86 | 10YR 6/6 | - | ab/sb, fi | vfi | | |
| LS3 | Bw(t) | 8-30 | 10YR 5/6 | - | ab, fi | fr | g | argic |
| | 2BC | 50-70 | 10YR 6/4 | - | ab, m | fr | g | |
| | 3BC | 70-110 | 7.5YR 5/8 | - | ab, m | vfr | g | |
| LS4 | AE | 0-20 | 10YR 5/4 | - | sb, fi | fr | w | |
| | 2Btg1 | 36-64 | 7.5YR 4/6 | 2.5 YR 7/3 | ab, m | fr/vfr | g | argic |
| | 2BC | 81-105 | 5YR 8/3 | 5Y 8/3-6/3 | sb, fi | fr | | |
| LS5 | AEg | 4-14 | 10YR 4/1 | - | ab, m | fr | c,w | |
| | Btg1 | 40-50 | 5Y 6/2 | 10YR 5/6 | ab, m | fi | g | argic |
| | CBtg | 70-100 | G1 6/5GY | 7.5YR 5/6 | ab/sb, m | fi | | |

Explanations: structure: vfi – very fine, fi – fine, m – medium, ab – angular blocky, gr – granular, pl – platy, sb – subangular blocky; consistence (moist): vrf – very friable, fr – friable, fi- firm; Horizon boundary: c – clear, g – gradual, s – smooth, w – wavy

# 5. Methods

## 5.1 Sampling and Geochemistry

Five profiles were opened on different bedrocks in Lower Silesia, Poland (see previous chapter). The soils were described according to the FAO Guidelines (FAO 2006). Characteristics like elevation, coordinates, exposure, slope and present land use of each site were determined and the color, depth and soil texture of each horizon defined. The soil reference groups were identified using the WRB classification (IUSS Working Group 2015). From each soil horizon approximately 2 kg of soil material was collected. After sampling, the samples were dried, slightly crushed and passed through a 2 mm sieve at the Institute of Soil Science and Environmental Protection of Wroclaw University of Environmental and Life Sciences (Waroszewski et al. 2016). Chemical and physical parameters like total elemental content, oxalate- and dithionite extractable contents, pH, $C_{org}$, base saturation and grain sizes were determined. Additionally, total elemental contents were obtained through sample fusion with lithium borate and XRF anayses (Acme Labs, Vancouver, Canada). Several element ratios were calculated.

## 5.2 SEM

Before identification of the heavy minerals using the scanning electron microscope (SEM), the heavy fraction had to be extracted from the samples. About 60-80 g of soil material was sieved with a mesh width of 0.1 mm. The fraction < 0.1 mm was then pre-separated in a water bath. The collected material was treated with hydrogen chloride (HCl, 10 %) to remove the coatings from the minerals. The samples were washed several times with deionized $H_2O$ and then dried in the oven at 95°C.

For the heavy mineral separation, sodium polytungstate (SPT) was used. To obtain the heavy minerals, a density of 2.97 g/cc was needed which was reached by either heating the SPT or by adding water to it. The SPT was poured into a funnel and around 3-6 g of the < 0.1 mm fraction was added. The mixture was left for approximately four hours and stirred every 30 minutes. During this time, enough heavy minerals were sunken to the closed end of the funnel (see Figure 10, a). The material less dense than 2.97 g/cc was floating on top of the liquid and could be removed.
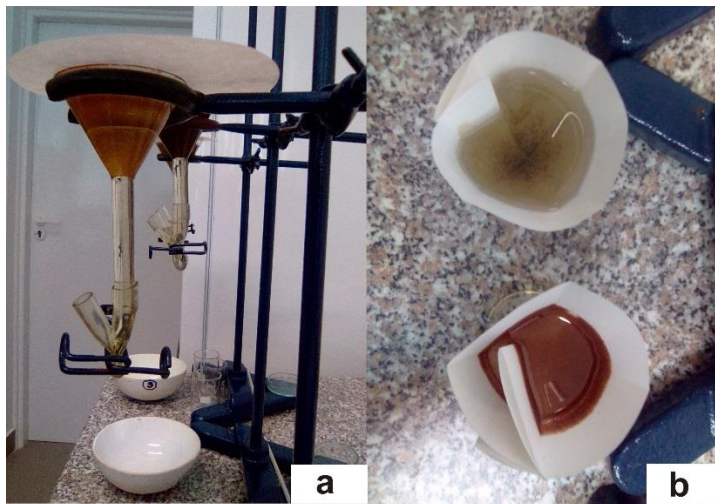
**Figure 10:** Heavy minerals separation with SPT (M. Vögtli 2017).

The rest of the liquid containing the heavy minerals was poured into a beaker covered with folded filter paper to collect the minerals (see Figure 10, b). Then, the heavy minerals were cleaned with deionized water, dried and were used for thin section preparation. Those were prepared at the Institute of Geological Sciences at University of Wroclaw.

The identification of the heavy mineral assemblage was conducted with a scanning electron microscope (SEM) at University of Wroclaw. Heavy minerals were identified by using JEOL JSM-IT100 coupled with an Energy Dispersive Spectrometer (EDS) at high vacuum, 15–20 kV working mode and 40 s counting time in polished thin sections (personal communication J. Waroszewski). Approximately 200 grains per sample were shot for the statistical significance. The spectrogram of each grain was studied, and the corresponding mineral identified by using the website webmineral.com and Reed 2010 (Reed 2010, Webmineral 2018).

5.3 XRD

For the X-ray Diffraction (XRD) measurements, the clay minerals were first extracted from the < 2 mm fraction. The soil was pre-treated to remove aggregating agents, so that the clay size fraction can be separated from coarser particles by sedimentation (Schaetzl and Anderson 2005; Brindley 1980; Kunze and Dixon 1986; Whittig and Allardice 1986). Therefore, 30 g of sieved, dried soil material was used from each sample. First, the organic material was removed and thus, two litres of hydrogen peroxide $H_2O_2$ solution (3 %; buffered with Na – acetate to pH 5) was prepared as follows: 200 ml $H_2O_2$ (30%) + 240 µl Acetic Acid (2mmol) + 492 mg Na – acetate (3.6 mmol) per 2 l deionized $H_2O$. Then, 50 ml of the $H_2O_2$ solution (3 % buffered with Na – acetate) was added to each sample (Brindley 1980) .

The samples were left at room temperature for two hours and stirred 3-4 times/h, then 25 ml of the $H_2O_2$ solution (3 % buffered with Na – acetate) was added. The samples were placed on the stove at a temperature of 50 °C for seven hours and stirred 1 -2 times/h. At the end, again 25 ml of the $H_2O_2$ solution (3 % buffered with Na – acetate) was added and left overnight.

The treated samples were transferred into a 250 ml centrifuge beaker and filled with deionized $H_2O_2$, then centrifuged at 12'000 revolutions per minute (rpm) for 15 minutes in a centrifuge with Rotor SLA 1500. Afterwards, the supernatant was decanted, and the remaining sediment was washed out with approximately 100 ml deionized $H_2O$ into a 250 ml beaker. Next, hexametaphosphate (5 % Calgon) was prepared: 12.5 g Na - Hexametaphosphate + 1.75 g $Na_2CO_3$ (water-free) per 250 ml. Then 10 ml of the prepared sodium hexametaphosphate (5 %) was added to each sample and treated with the ultrasonic Badelin Sonoplus HD 2070, 5 min, 70%, five cycles.

After the removal of organic material, the separation of clay minerals was conducted. First, each sample was transferred quantitatively into a 250 ml shaker bottle, filled up to 200 ml with deionized $H_2O$, and then 5 ml sodium hexametaphosphate (5 %) was added. The whole mixture was shaken for one hour at 150 rpm.
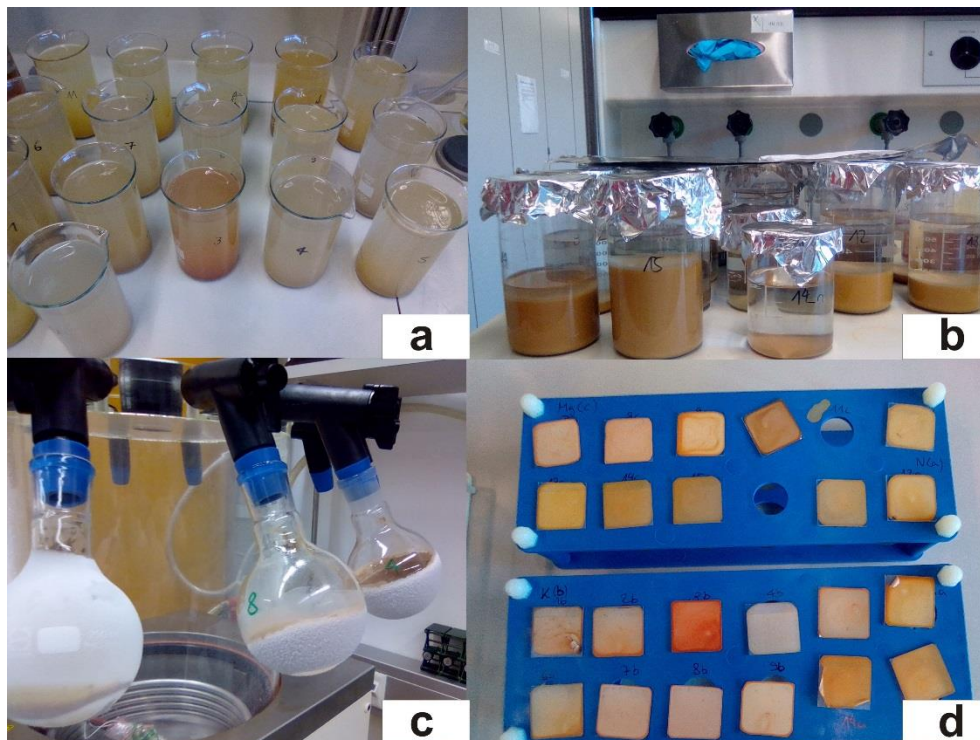


**Figure 11:** Clay extraction for XRD measurements: drop height according to Stokes's law (a), overnight coagulation (b), freeze drying (c) and orientated samples on glass slides (M. Vögtli 2017).

The sample material then was transferred into a 500 ml beaker and filled up with deionized $H_2O$ to 2 cm below its seam (see Figure 11, a). Then, the samples were stirred intensively and left at 20 °C for 6h 58 min., the drop height according to Stokes's law was 9 cm.

Meanwhile, the 2M MgCl$_2$ was prepared: 406.6 g MgCl$_2$ x 6 H$_2$O per 1 l deionized H$_2$O. After 6h 58 min., the suspension was transferred with a pump into a 1000 ml beaker, the remaining sediment was left in the beaker. Then, 30 ml of the 2M MgCl$_2$ was added to the remaining sediment and left overnight for coagulation (Figure 11, b). This whole procedure was repeated seven times until the suspension was clear and sufficient clay material was collected.

The clay material was put into 100 ml special tubes and centrifuged for 10 minutes at 4000 rpm. The supernatant was decanted, approximately 40 ml deionized H$_2$O was added, and each sample was centrifuged again for 15 min at 4000 rpm. The last step was conducted three times to wash out the chlorides. After removal of the water, the sample were put into special beakers and freeze dried, see Figure 11, c (Egli et al. 2017).

The next step of the clay pre-treatment was to put a thin film on glass slides for XRD measurements. Therefore, the solutions for potassium (K)-saturation and magnesium (Mg)-saturation had to be prepared. Mg and K were used to saturate the interlayer cation adsorption sites (Schaetzl and Anderson 2005).

For the Mg-saturation 1 M MgCl$_2$ was prepared as follows: 25.42 g of MgCl$_2$ • H$_2$O per 250 ml of solution with deionized water. First, 25-30 mg of the clay material was weighted into a 15 ml centrifuge tube. 2.5 ml 1 M MgCl$_2$ solution was added and the tube was agitated until the sample was in suspension. The samples were treated in an ultrasonic bath for 30 seconds and then centrifuged for five minutes, at 4000 rpm. After, the supernatant was decanted, 2.5 ml 1 M MgCl$_2$ were added and agitated. The samples were shaken overnight, then again centrifuged for five minutes (4000 rpm) and the supernatant decanted. Next, 2.5 ml 1 M MgCl$_2$ solution was added, agitated, treated in an ultrasonic bath for 30 seconds and then centrifuged for five minutes (4000 rpm). Then, the samples were washed three times with H$_2$O. Every time 2.5 ml deionized H$_2$O was added, agitated and centrifuged for five minutes (4000 rpm). The supernatant was decanted and 1000-2000 µl were put on a glass slide with a pipette. The orientated samples on the glass slides are shown in Figure 11, d.

The same procedure as describe above was conducted for the K-saturation. Therefore, in the beginning 1 M KCl solution was prepared as follows: 18.64 g of KCl per 250 ml of deionized water. As a control, the same treatment was conducted with deionized H$_2$O. In total, three series of glass slides were prepared: one with the K-saturated sample, one with the Mg-saturated samples and the samples treated with deionized H$_2$O. The glass slide method was used because it is ease of application. One must say that the orientation is only fair, but for qualitative analysis this method is suitable (Moore and Reynolds 1997).

After X-raying of the first three series, the Mg-saturated samples were equilibrated with glycerol. The glycerol solvation was mainly conducted to distinguish between vermiculite and smectite (Walker 1958; Mosser-Ruck et al. 2005). The K-saturated samples were first heated at 335°C, and then at 550°C. After each heating and the glycerol treatment, the samples were x-rayed again (Schaetzl and Anderson 2005). Additionally, randomly orientated powder samples were prepared.

The orientated samples on the glass slides were x-rayed using CuKα radiation from 2 to 15°2θ with steps of 0.02°2θ at 2s/step. To study the *d*(060) region, the randomly orientated samples were step-scanned from 58 to 64°2θ with steps of 0.02°2θ at 10 s intervals using a Bruker AXS D8 Advance (CuKα). The same samples were used to scan the region from 2 to 80°2θ with steps of 0.02°2θ (Waroszewski et al. 2016). The obtained x-ray data in the range of 2 to 15°2θ were corrected for Lorentz and polarization factors using EVA (Moore and Reynolds 1997). "The diffraction patterns in the range of 2 to 15°2θ and 58 to 64°2θ were fitted by the Origin^TM PFM programme using the Pearson VII algorithm." (Waroszewski et al. 2016, p. 369). For the baseline a parabola was set and the d-spacing (°A) was calculated with the Bragg equation:

$$d = 1.541838/(2 * \sin\left(\left(\frac{2\theta}{2}\right) * \frac{\pi}{180}\right)$$

Whereby 1.541838 is the angle of copper (Cu). The XRD pre-treatment and the measurement were conducted at University of Zurich.

## 5.4 DRIFT

In addition to the XRD measurements, diffuse reflectance infrared fourier transformation (DRIFT) measurements were conducted at the Department of Geography at University of Zurich (GIUZ) to distinguish the clay minerals chlorite and kaolinite. Therefore, 97 % of Potassium bromide (KBr) and 3 % of soil material were mixed. Thus, 30 mg of the extracted clay fraction and 270 mg of KBr were weighted into Eppendorf vessels. As a control, one vessel was filled with 300 mg KBr. The samples then were dried for 30 minutes at 80°C. After the removal of the moisture, the Eppendorf vessels were put into shake containers and put on a shaker for 120 seconds with a frequency of 20 hertz (Hz). This step was necessary to homogenize the samples. The samples were heated again at 80°C for 45 minutes (Egli et al. 2017). Then, a small amount of each sample was analyzed from the range 250 to 4000 cm$^{-1}$ with the DRIFT (Waroszewski et al. 2016). The used software was OPUS 6.5, which had a sample and background scan time of 64 seconds, each. The interferogram shows the intensity measured as a function of the distance difference of the screened sample. It was used for qualitative identification of the clay minerals (Egli et al. 2017).

# 6. Results

## 6.1 Physical and geochemical data

In this chapter physical and geochemical data will be described and analyzed. The detailed dataset is found in the appendix (p. 72-76).
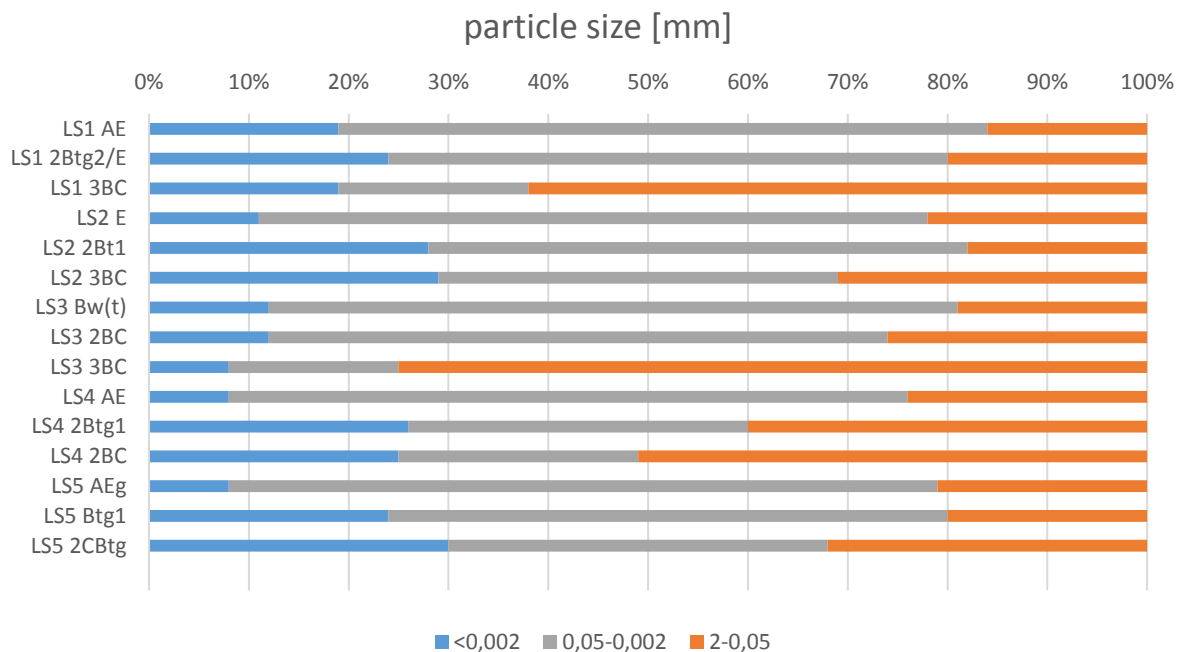


**Figure 12:** Particle size distribution [mm] of the investigated profiles and horizons.

In Figure 12 the percentage of the particle sizes is shown. Thereby, the distinction is made between clay (< 0.002 mm), silt (0.05-0.002 mm) and sand (2-0.05mm). In the loess mantle of LS1 (AE) the clay content lays at 19 % while the sand content is 16 %. The silt content is certainly the highest there, showing a content of 65 %. The transition horizons of LS1 (2Btg2/E) shows a clay and sand content of 24 % and 20 %, respectively. In this horizon the silt content is the highest with 56 %. LS1 3 BC shows similar clay and silt contents (19 %) while the sand content is the highest of the profile with 62 %. The loess mantle of LS2 (E horizon) exhibits clay and sand contents of 11 % and 22 %, respectively. Moreover, the silt content is the highest with 67 %. The 2Bt1 horizon is characterized by a high silt content (54 %) and a low sand content (18 %). The clay content is 28 %. Furthermore, the horizon of the underlying substrate (3BC) has a high silt content (40 %) and similar sand and clay contents (around 30 %). For the loess mantle of LS3 (Bw(t)) a silt content of 69 %, a sand continent of 19 % and a clay content of 12 % is observed. The 2 BC of LS2 exhibits also a high silt content (62 %) while sand and clay contents lay at 26 % and 12 %, respectively.

The 3BC which reflects the underlying substrate of LS3, shows a quite high sand content with 75 % while a silt content of 17 % and a clay content of 8 % is found.

For LS4 the loess mantle is characterized by a silt content of 68 %, a sand content of 24 % and a clay content of 8 %. Towards the underlying bedrock a decrease of the silt content is observed (34 %). Instead, the sand and clay contents increased with 40 % and 26 %, respectively. At the bottom of the profile (2BC), the sand content is quite high with 51 % while sand and clay contents are around 25 %. To conclude, the last profile LS5 shows again a high silt content (71 %) in the loess mantle while the sand content is 21 % and the clay content 8 %. The transition horizon (Btg1) exhibits compared to the loess cover, a lower silt content of 56 %. There, the sand content is 20 % and the clay content reaches 24 %. The particle size distribution of the 2CBtg of LS5 is rather balanced with 38 % of silt, 32 % of sand and 30 % of clay.
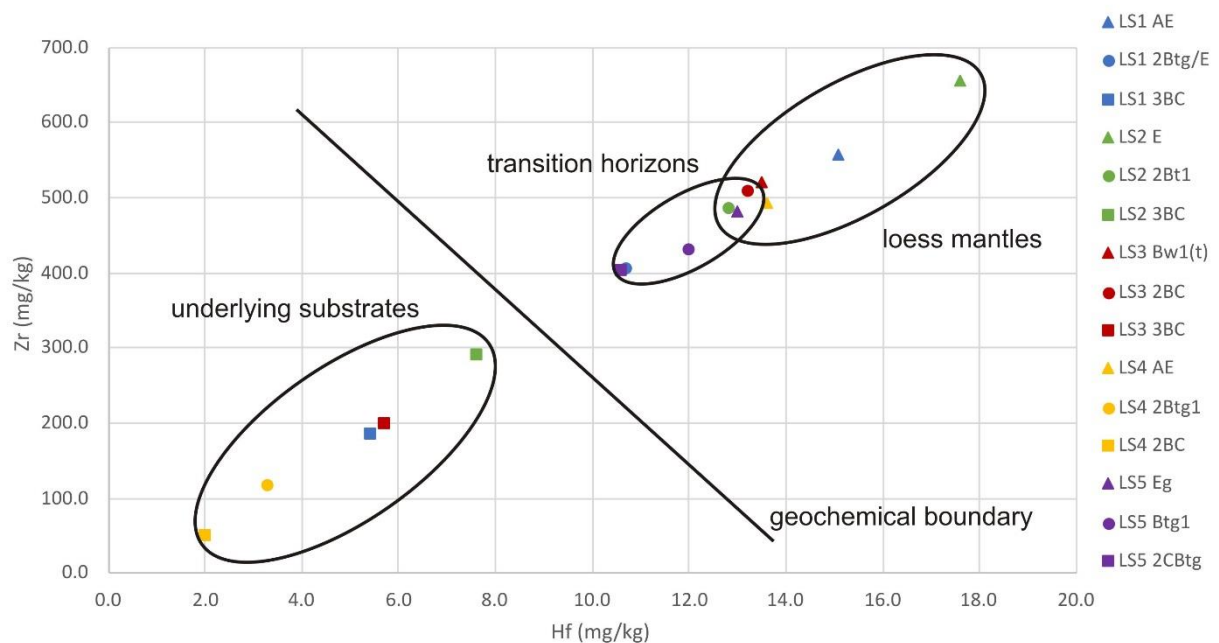


**Figure 13:** Relationship of Hf and Zr for the five profiles. A clear geochemical boundary between the upper horizons and the underlying substrates is observed.

Regarding the geochemistry, several immobile elements like zirconium (Zr), titanium (Ti) and hafnium (Hf) were analyzed. Chemically immobile elements are used to study possible aeolian additions to soils (Dahms and Egli 2016).

In Figure 13, the concentration of Hf and Zr in the investigated horizons of the profiles are shown. A clear geochemical boundary between the loess mantles, the transition horizons and the bedrocks can be observed. Furthermore, the Hf and Zr concentrations exhibit a linear relationship. The loess mantles (displayed as triangles) show relatively high concentration of Hf and Zr, ranging between 13 and 17.6 ppm and 481.5 and 656.2 ppm, respectively. The transition horizons (displayed in circles) exhibit slightly lower Hf and Zr concentrations than the loess mantles.

The Hf concentrations lay between 3.3 and 13.2 ppm while the Zr concentration range from 118.7 to 509.9 ppm. The bedrock horizons (displayed in squares) obviously show the lowest concentrations. Hf occurs with 2 to 10.6 ppm while Zr shows concentrations between 50.6 and 403.5 ppm. The transitions horizons of LS4 (2Btg1) exhibits lower concentration than the other transition horizons and thus is comparable with the bedrock concentrations.
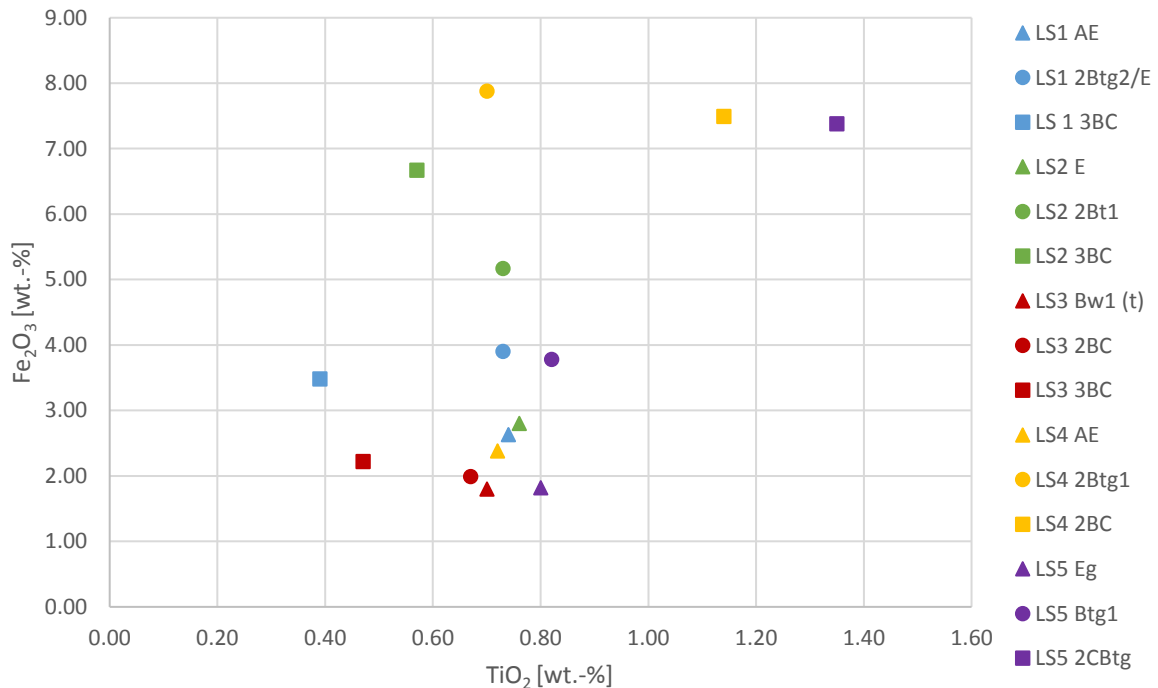


**Figure 14:** $Fe_2O_3$-$TiO_2$ [wt.-%] plot showing the geochemical weathering behavior in the horizons of the five study sites.

In addition, the $Fe_2O_3$-$TiO_2$ contents were compared (see Figure 14). These are helpful to understand the changes in elemental compositions due to pedogenesis. Thereby, the relative enrichment of Fe (in this example) during pedogenesis is illustrated (Schatz et al. 2015). The $Fe_2O_3$/$TiO_2$ percentages of the loess mantles scatter all in a similar area. They are small and range between 0.68 and 0.8 wt.-% ($TiO_2$) and between 1.8 and 2.8 wt.-% ($Fe_2O_3$). The transition horizons exhibit similar $TiO_2$ percentages ranging from 0.67 to 0.82 wt.-%. Their $Fe_2O_3$ percentages on the contrary are widely distributed, between 1.99 and 7.88 wt.-%. Focusing on the bedrock, a wide $TiO_2$ range is observed, with weight percentages between 0.39 and 1.35. The $Fe_2O_3$ contents also show a wide range between 2.22 and 7.49 wt.-%.

The K/Rb and the Ti/Zr ratios were calculated (shown in Figure 15 a & b, right and left row, respectively). Both are applied to determine changes in lithogenic sources (Silva-Sánchez et al. 2015) and show admixtures of another sedimentological component (Sauer et al. 2016). In the next section the Ti/Zr and the K/Rb ratios are described in detail for each profile.
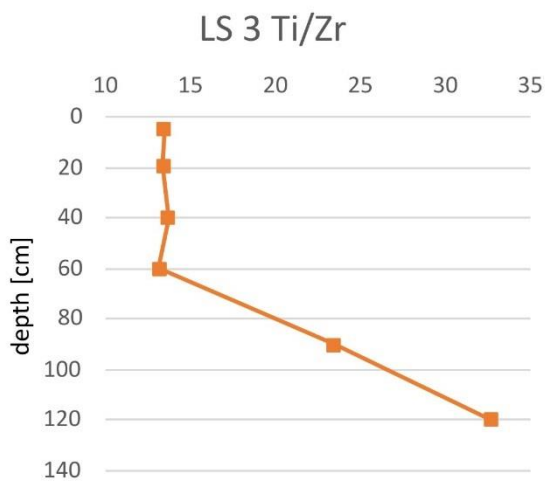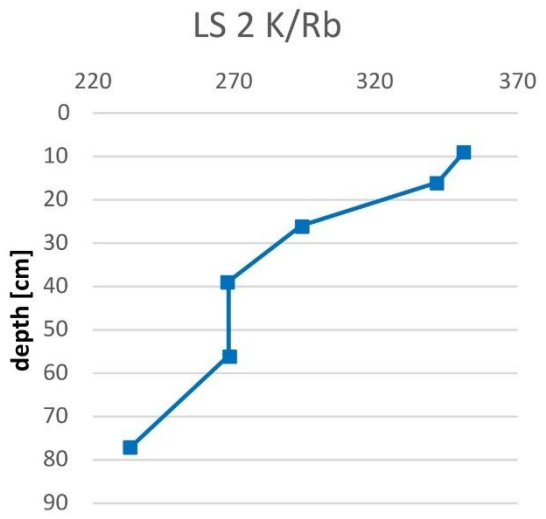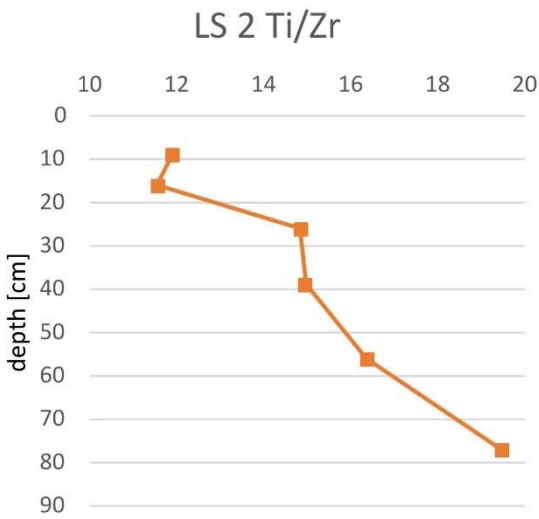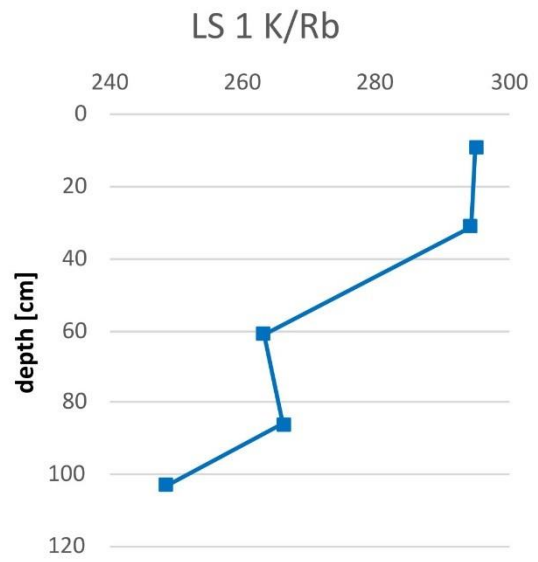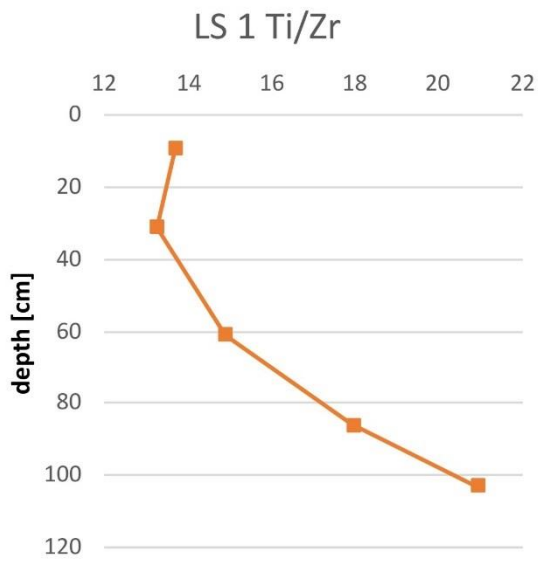
**Figure 15a:** Ti/Zr ratios (left) and the K/Rb ratios (right) for LS1, LS2 and LS3.
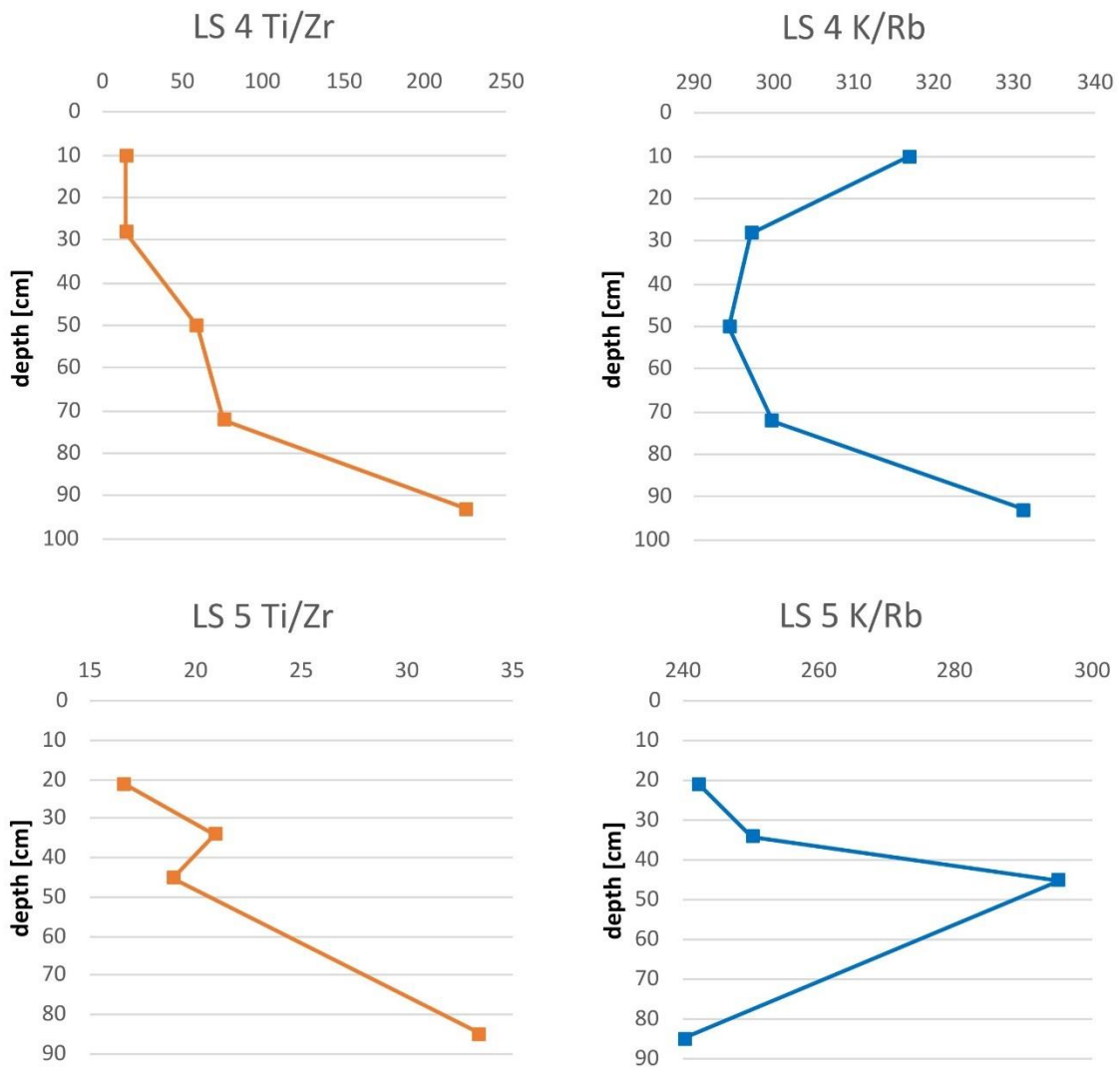
**Figure 15b:** Ti/Zr ratios (left) and the K/Rb ratios (right) for LS4 and LS5.

One can observe that the Ti/Zr ratio in each profile increases towards the bedrock. LS1 exhibits Ti/Zr ratios between 13.2 (in the loess mantle) and 20.9 (underlying substrate). LS2 shows ratios of 11.6 and 19.5 in the loess mantle and in the bedrock, respectively. The transition horizon shows values around 16.0. Ti/Zr ratios for LS3 are quite constant in the loess mantle and transition horizon showing ratios between 13.1 and 13.7. Towards the granitic bedrock, an increase of the ratios is recognizable with values between 23.4 and 32.7. LS4 shows Ti/Zr ratios around 14.5 in the loess mantle. An increase is observed in the middle part of the profile with ratios of 58.9 and 75.4. The underlying glacio-fluvial material exhibits a strong increase in the ratios, up to 225.3. Consequently, LS4 consists of the widest Ti/Zr range. LS5 has a Ti/Zr ratio of 16.6 in the loess mantle and values of 18.9 and 20.9 in the transition horizon. The underlying basalt shows a ratio of 33.4. A slight decrease in the transition horizon is identified.

On the contrary in all profiles except LS4, the K/Rb ratios exhibit a decrease towards the underlying substrate. LS1 has a K/Rb ratios in the loess mantle of 294.3. The transition horizon has a ratio of 266.1 while the Permian sandstone shows a ratio of 248.5. The K/Rb ratio for the loess mantle of LS2 is the highest of all profiles with 341.9. In the transition horizon a K/Rb ratio of 267.8 was calculated and for the serpentinite a ratio of 233.6 was found. LS3 has ratios of 357.9, 331.5 and 343.6 for the loess mantle, transition zone and underlying granite, respectively. Moreover, LS4 has the lowest K/Rb ration in the transition horizon with 294.5 while the ratio in the loess is slightly higher with 316.9. The glacio-fluvial material shows a K/Rb ratio of 331.2. In LS5 the highest K/Rb ratio was identified in the transition horizon with 295.2. The loess mantle and the basalt have similar ratios around 241.

## 6.2 SEM

The results obtained with SEM are described in the following sections. Figure 16 shows a detail of a backscattered electron picture of heavy minerals from LS1 3BC. More details for each profile can be found in the appendix, p. 77 & 78).
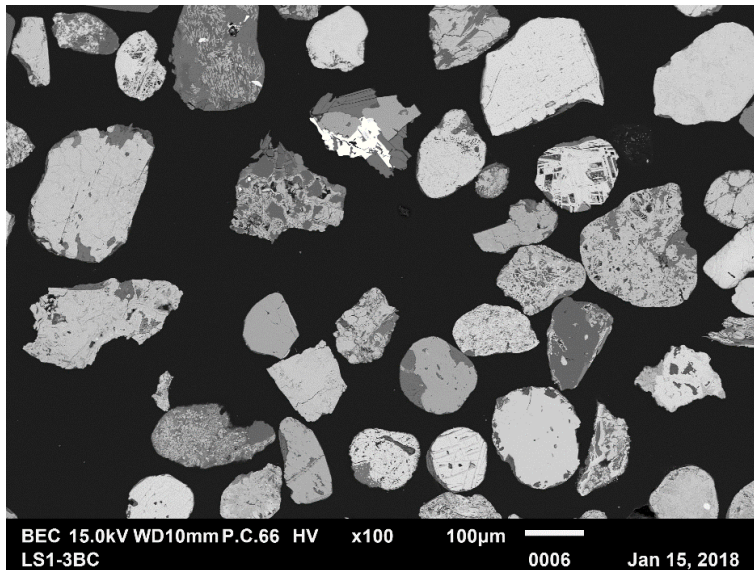


**Figure 16:** Backscattered electron picture of the heavy mineral fraction of LS1 3BC. The light grey colored minerals reflect the very heavy fraction while the dark colored are lighter minerals (J. Kierczak 2018).

LS1

In the profile LS1, which lies on Permian sandstone, the mantle with the aeolian silt consists of a high percentage of Fe-oxides (30.5 %). In addition, magnesiochromite and magnetite (17.4 %), rutile (12.6 %) and ilmenite (12.1 %) are present in significant amounts. Other heavy minerals occurring in LS1-3BC are: amphibole, apatite, biotite, chlorite, minerals of the epidote-group, garnet, monazite, staurolite, tourmaline and zircon.

The transition horizon of LS1 (2BgE) is characterized by Fe-oxides (26.8 %), magnesiochromite and magnetite (14.5 %), rutile (13.8 %) and garnet (10.1 %).

Other heavy minerals, which are present are: minerals of the $Al_2SiO_5$- and epidote-group, amphibole, biotite, ilmenite, monazite, titanite, tourmaline, ulvospinel and zircon.

The bedrock (3BC) consists of Fe-oxides (33.2 %), ilmenite (21.5 %), magnesiochromite and magnetite (16.4 %) and rutile (8.4 %). Other heavy minerals are: albite, biotite, monazite, ulvospinel, xenotime and zircon. The heavy mineral composition for each horizon of LS1 is shown in Figure 17.
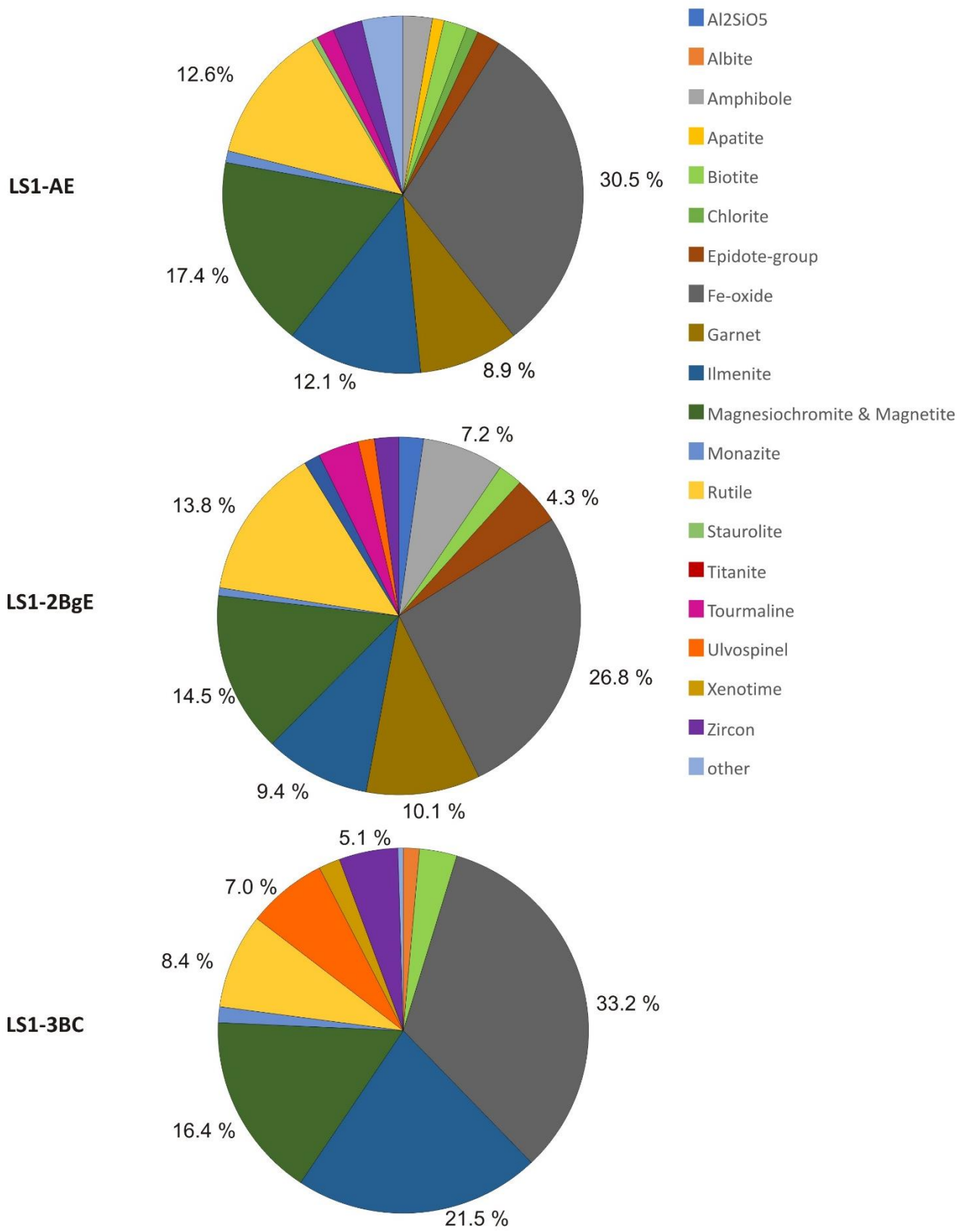
**Figure 17:** Heavy mineral composition for LS1 on Permian sandstone.
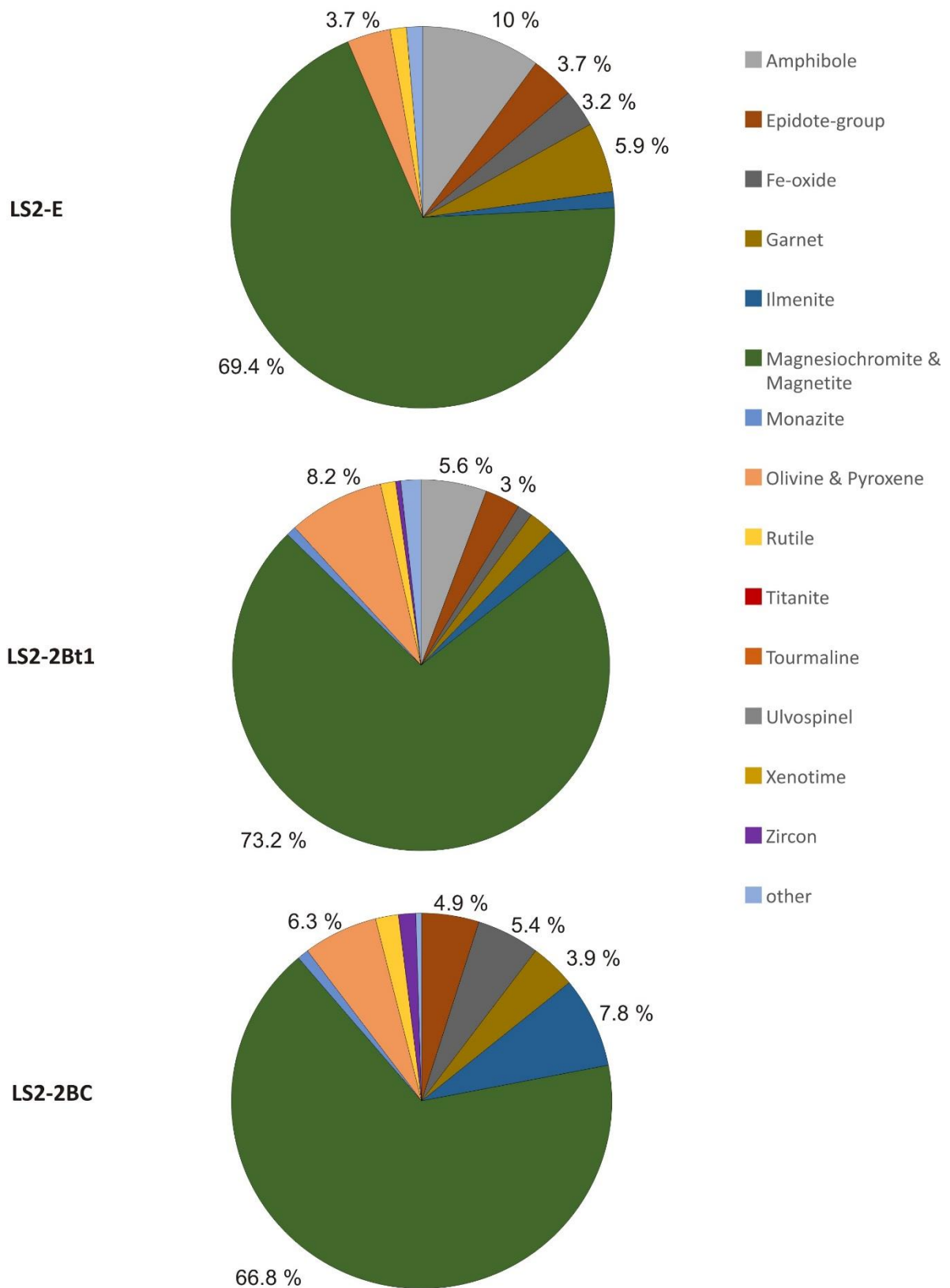
**Figure 18:** Heavy mineral composition for LS2 on serpentinite.

LS2

The profile LS2 is located on serpentinite. The loess mantle (E horizon) is characterized by a high amount of magnesiochromite and magnetite (69.4 %) and amphibole (10 %). Additionally, minerals from the epidote-group, Fe-oxides, garnet, ilmenite, olivine and pyroxene and rutile are detected.

The transition horizon of LS2 (2Bt1) exhibits also a high amount of magnesiochromite and magnetite (73.2 %) and olivine and pyroxene (8.2 %) are present. Additionally, amphibole, minerals from the epidote-group, Fe-oxides, garnet, ilmenite, monazite, rutile and zircon are identified.

The bedrock (2BC) of LS2 consists also of magnesiochromite and magnetite (66.8 %). In addition, smaller amounts of ilmenite (7.8 %) and olivine and pyroxene (6.3 %) occur. Minerals from the epidote-group, Fe-oxides, garnet, monazite, rutile and zircon are observed. The heavy mineral composition of the investigated horizons of LS2 is shown in Figure 18.


LS3

LS3 which is located on granite, exhibits a considerable amount of Fe-oxides (34 %), ilmenite (16.7 %) and magnesiochromite and magnetite (12.9 %) in the loess mantle (Bw horizon). This horizon consists also of amphibole, minerals of the epidote-group, garnet, monazite, olivine and pyroxene, rutile, staurolite, xenotime and zircon.

The transition horizon (2BC) is characterized by rutile (31.5 %), Fe-oxides (23.7 %) and ilmenite (18.3 %). Additional detected heavy minerals are biotite, epidote minerals, garnet, magnesiochromite and magnetite, monazite, staurolite and zircon.

For the bedrock (3BC) a high amount of rutile (66.7 %) and biotite (18 %) are identified. Additional heavy minerals are: Fe-oxides, ilmenite, monazite and xenotime. The heavy mineral composition of the investigated horizons of LS3 is shown in Figure 19.
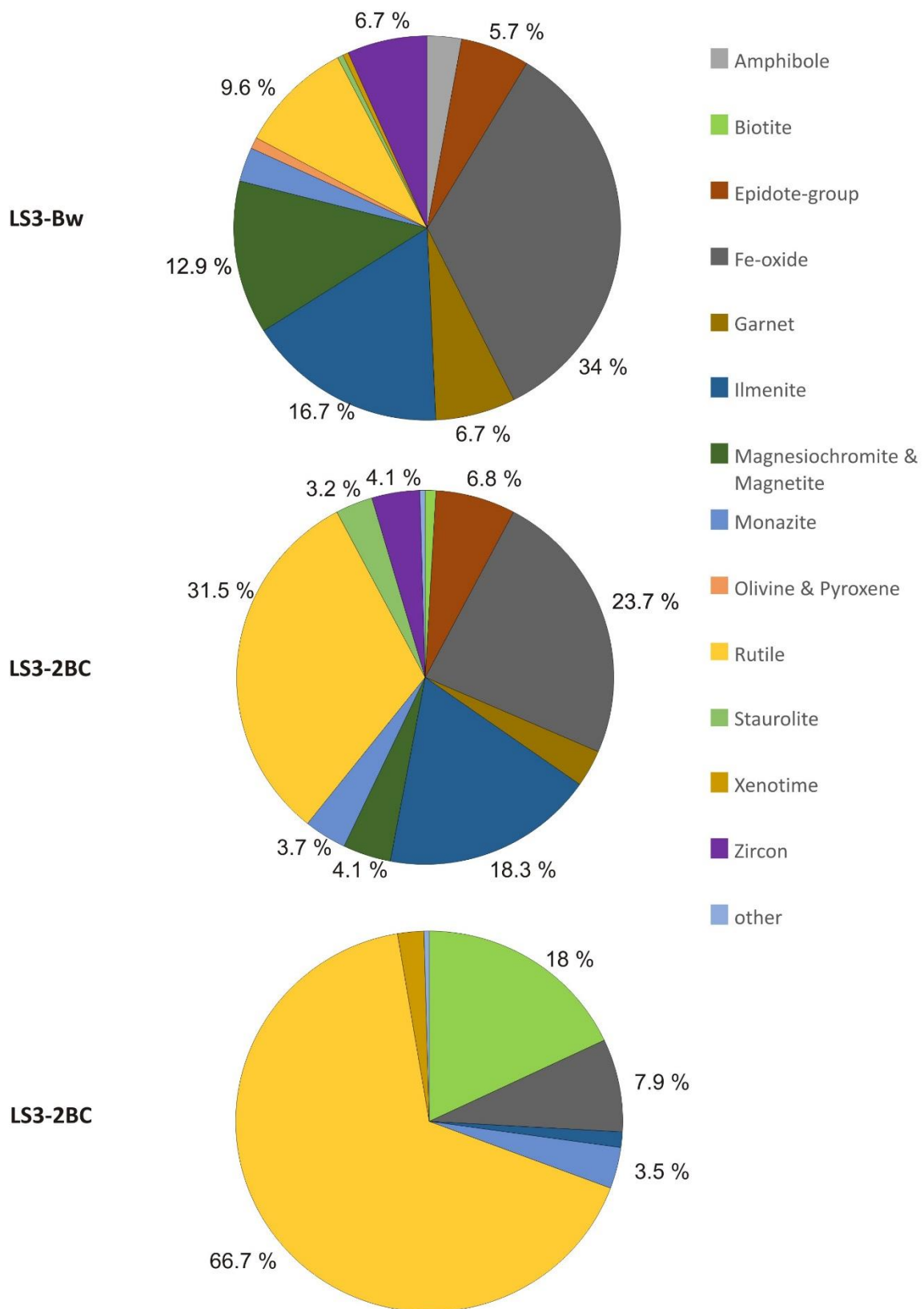
**Figure 19:** Heavy mineral composition for LS3 on granite.
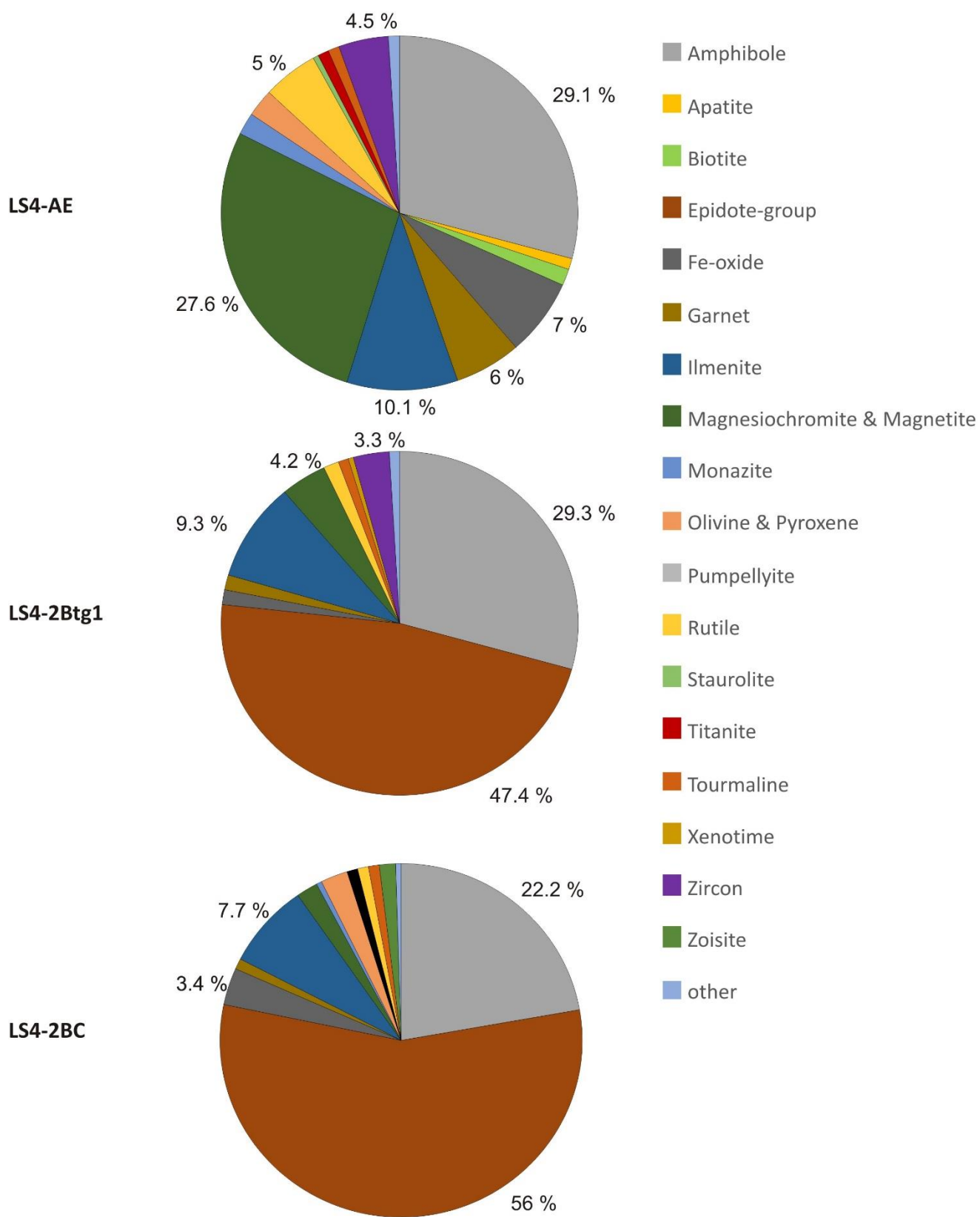
**Figure 20:** Heavy mineral composition for LS4 on glacio-fluvial material.

LS4

The loess mantle of the profile on glacio-fluvial material (LS4 AE) exhibits amphibole (29.1 %), magnesiochromite and magnetite (27.6 %) and ilmenite (10.1 %) as main heavy minerals. Apatite, biotite, Fe-oxides, garnet, monazite, olivine and pyroxene, rutile, staurolite, titanite, tourmaline and zircon are present.

In the transition horizon (2Btg) epidote (47.4 %) and amphibole (29.3 %) reflect the main heavy fraction. Moreover, Fe-oxides, garnet, ilmenite, magnesiochromite and magnetite, rutile, tourmaline, xenotime and zircon are present.

The bedrock (2BC) also consists of epidote (56 %) and amphibole (22.2 %). Additional heavy minerals are: Fe-oxides, garnet, ilmenite, magnesiochromite and magnetite, monazite, olivine and pyroxene, pumpellyite, rutile, tourmaline and zoisite. The heavy mineral composition of the investigated horizons of LS3 is displayed in Figure 20.

LS5

LS5, the profile on basalt exhibits epidote (23 %), amphibole and rutile (both 18 %) in the loess mantle (AEg horizon). Additional heavy minerals are: Fe-oxides, ilmenite, monazite, olivine and pyroxene, pumpellyite, spinel, titanite, ulvospinel, xenotime and zircon.

In the transition horizon (Btg1) epidote (16 %), amphibole (15 %), ilmenite and ulvospinel (both 12 %) are the main heavy minerals. Additionally, Fe-oxides, monazite, olivine and pyroxene, pumpellyite, rutile, staurolite, titanite and zircon were identified.

In the bedrock (2BCg2) ulvospinel (25 %), olivine and pyroxene (18 %) and pumpellyite (12 %) present the main heavy fraction. Amphibole, epidote, Fe-oxide, ilmenite, monazite, rutile, spinel, staurolite and zircon were also observed. The heavy mineral composition diagrams of LS5 are shown in Figure 21.
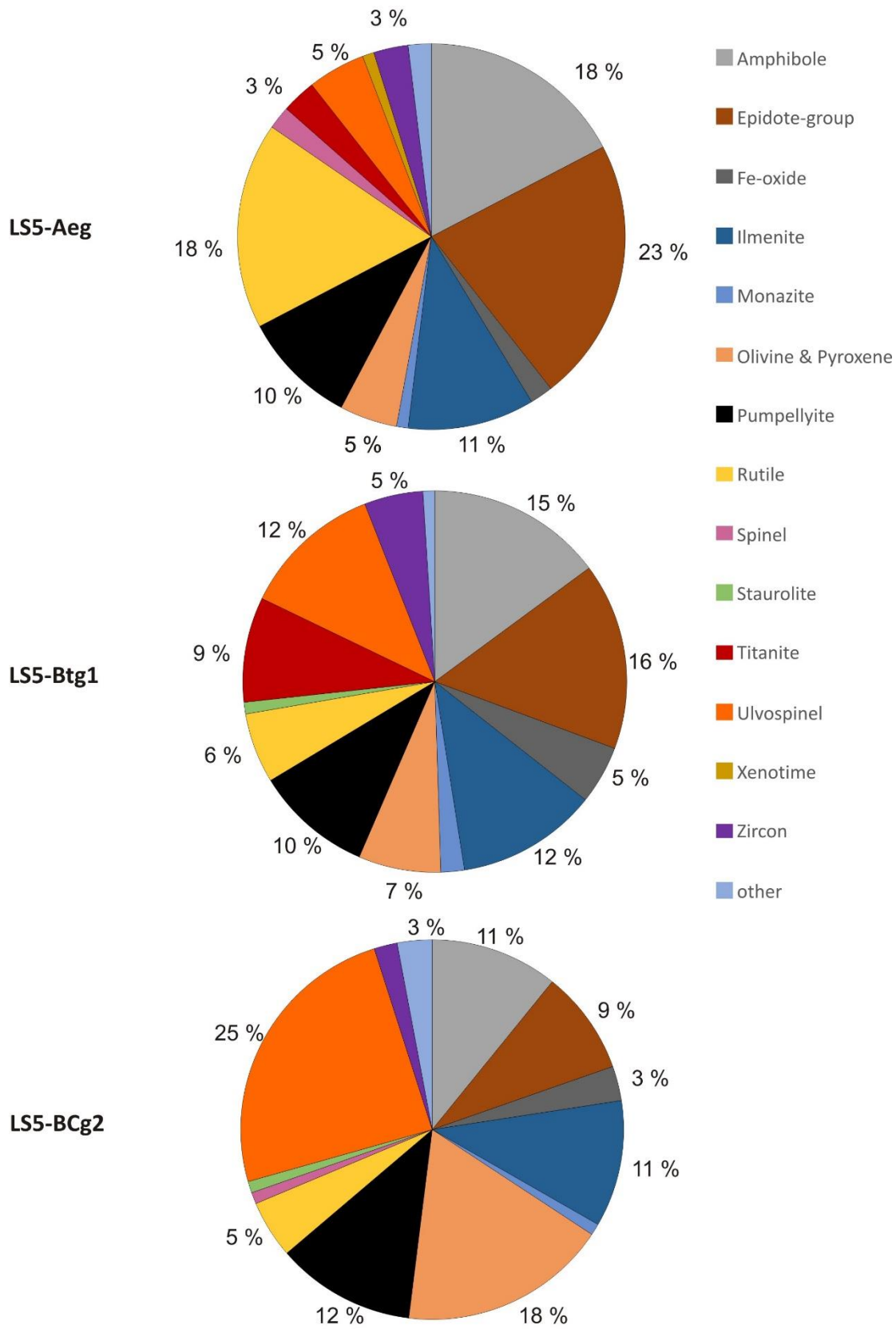
**Figure 21:** Heavy mineral composition for LS5 on basalt.

6.3 XRD

The analyzed clay fraction (< 2 µm) consists of quartz, mica, chlorite, kaolinite, smectite, interstratified mica-vermiculite or hydroxy-interlayered vermiculite (HIV) and vermiculite. The results for each horizon can be found in Table 3.

**Table 3:** Major components of the clay fraction.

| Soil profile | Soil Horizon | Quartz | Mica | Chlorite | Kaolinite | Smectite | Interstratified mica-vermiculite or HIV | Vermiculite |
|---|---|---|---|---|---|---|---|---|
| LS1 | AE | Xx | xx | x | xx | x | x | x |
| | 2Btg/E | Xx | xx | (x) | xx | (x) | x | (x) |
| | BC | Xx | xx | - | xx | (x) | x | x |
| LS2 | E | Xx | xx | x | xx | x | x | x |
| | 2Bt1 | Xx | xx | (x) | xx | x | x | x |
| | 3BC | xx | x | (x) | xx | x | (x) | x |
| LS3 | Bw (t) | xx | x | x | xx | - | x | x |
| | 2BC | xx | xx | x | xx | - | x | x |
| | 3BC | xx | xx | - | xx | - | x | x |
| LS4 | AE | xx | xx | x | xx | (x) | (x) | x |
| | 2Btg1 | xx | (x) | - | xx | x | (x) | (x) |
| | 2BC | xx | (x) | - | xx | x | x | (x) |
| LS5 | AEg | xx | xx | (x) | xx | x | x | x |
| | Btg1 | xx | (x) | - | x | x | x | x |
| | 2CBtg | xx | x | - | xx | x | (x) | x |

xx major, x minor, (x) trace,
- absent

Here, a general description of the detected clay minerals in the 15 samples under different treatments is given.

Smectite is an expanding mineral. The treatment with Mg-glycerol leads to an expansion of the d-spacing to 1.7/1.8 nm while with heating (550°C) it collapses to 1.0 nm. Vermiculite is characterized by a d-spacing of 1.4 nm in the Mg-saturated sample. No expansion occurs after the Mg-glycerol treatment. With the K treatment and the heating at 550°, the 1.4 nm peak collapses to 1.0 nm. Mica is identified by a peak at 1.0 nm in all treatments. The first-order peak of kaolinite is at 0.7 nm, which coincides with the second-order peak of chlorite. Kaolinite decomposes at 550°C, but chlorite retains its *d(001)* at 1.4 nm. Characteristic for chlorite is the 1.4 nm d-spacing that persists in all treatments (Schaetzl and Anderson 2005).

In the following sections the interpreted clay mineralogy of each horizon of all profiles is described in detail. Figures are only shown for LS1 (AE and 3BC horizon) and LS3 (BW (t) and 3BC). All XRD pattern are found in the appendix, p. 86-93.
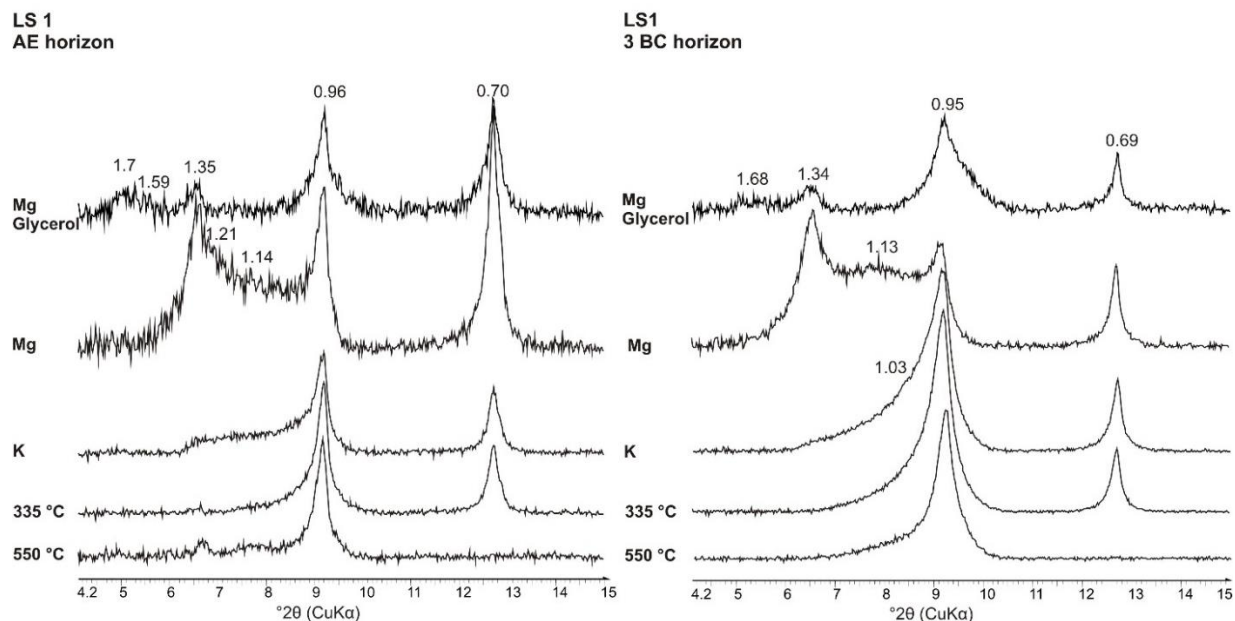
**Figure 22:** XRD pattern of the soil clays of the AE and 3BC horizon of LS1. Each treatment is displayed: Mg-glycerol, Mg- and K-saturation and heating treatments at 335°C and 550°C. D-spacings are given in nm.

The Mg-saturated samples of the AE horizon exhibit distinct peaks at 1.35, 0.96 and 0.70 nm (see Figure 22, left). At 1.21 and 1.14 nm peaks are assumed, which reflect interstratified mica-vermiculite or HIV material. With the glycerol treatment, the peaks at 1.35, 0.96 and 0.70 nm stay while at 1.74 nm a flat peak appears, which is identified as the $d_{001}$* of smectite. A small peak at 1.59 nm is also visible. The peak at 1.35 nm is identified as vermiculite whereas the peak at 0.96 nm appearing in all five treatments is assigned to mica. Further, the peak at 0.70 nm which disappears with the heating (550°C) was identified as kaolinite. A small peak at around 6.6°2θ with the 550°C treatment is detectable, which is assigned to chlorite.

In the 2Btg/E horizon a similar pattern is observed. With the Mg treatment distinct peaks appear at 1.34, 0.96 and 0.69 nm. At 1.14 and 1.08 nm peaks are assumed, which reflect the interstratified mica-vermiculite or mica-HIV. With the glycerol treatment peaks at 1.34, 0.96 and 0.69 nm stay, while a small peak at 1.70 nm (smectite) appears. Considering all treatments; 1.34, 0.96 and 0.69 are assigned to vermiculite, mica and kaolinite, respectively. Looking at the 550°C treatment, a weak peak at around 6.8°2θ is assumed, which is most probably chlorite.

The Mg-saturated clay fraction of the 3BC horizon (Figure 22, right) exhibits distinct peaks at 1.34, 0.95 and 0.69 nm, which are assigned due to their behavior with other treatments to vermiculite, mica and kaolinite, respectively.

Between the vermiculite and kaolinite peak in the Mg treatment, interstratified mica-vermiculite or HIV material is assumed. The small peak at 1.68 in the Mg-glycerol treatment is assigned to smectite.

LS2

The loess mantle (E horizon) of profile LS2 shows peaks at 1.34, 0.96 and 0.70 nm in the Mg-saturated samples. The peak at 0.70 nm is quite broad and possibly hides other peaks. It is assigned to kaolinite, but also to chlorite. Indications for the latter are the small peak at 6.7 °2θ (1.4 nm) in the 550℃ treatment. The peak at 1.34 nm in Mg and Mg-glycerol treatment is interpreted as vermiculite while the peak at 0.96 nm appearing in all treatments, is assigned to mica. The broad peak at 1.69 nm in the Mg-glycerol treatment is attributed to smectite, while the peak at 1.43 nm is either chlorite, vermiculite or HIV. In this horizon an additional peak is observed in the K-saturated samples at 1.31 nm, which is possibly HIV or HIS. Additionally, between the 1.34 and 0.96 nm peak, interstratified mica-vermiculite or HIV material exists.

The clay fraction of the transition horizon (2Bt1 horizon) revealed distinct peaks at 1.34, 0.96 and 0.69 nm in the Mg-saturated samples, which are assigned again to vermiculite, mica and kaolinite, respectively. In the glycerol treatment a high, broad peak at 1.73 nm is detectable which is characteristic for smectite. The presence of chlorite is given with the peaks at 1.40 and 0.70 nm of the 550℃ heating treatment. Again, the occurrence of interstratified mica-vermiculite or HIV material is assumed. Furthermore, a peak at 1.40 nm in the 335℃ heating treatment is observed which is assigned to chlorite.

The bedrock (3BC horizon) exhibits a distinct peak at 1.38 nm (vermiculite) and at 0.71 and 0.70 nm (chlorite and kaolinite) in the Mg-saturated samples. A small peak is identifiable at 0.97 nm, which is most probably mica. In the Mg-glycerol treated samples the characteristic peak for smectite at 1.71 nm appears while another peak at 0.89 nm is visible. In this horizon chlorite is present due to the characteristic peaks at 1.31 and 0.71 nm in the 550℃ treatment. It is also assumed that interstratified mica-vermiculite or HIV is present (Mg-saturation between 1.38 nm and 0.97 nm). The clay fraction of the K-saturation exhibits a peak at 1.38 nm which might be HIV or HIS.

.
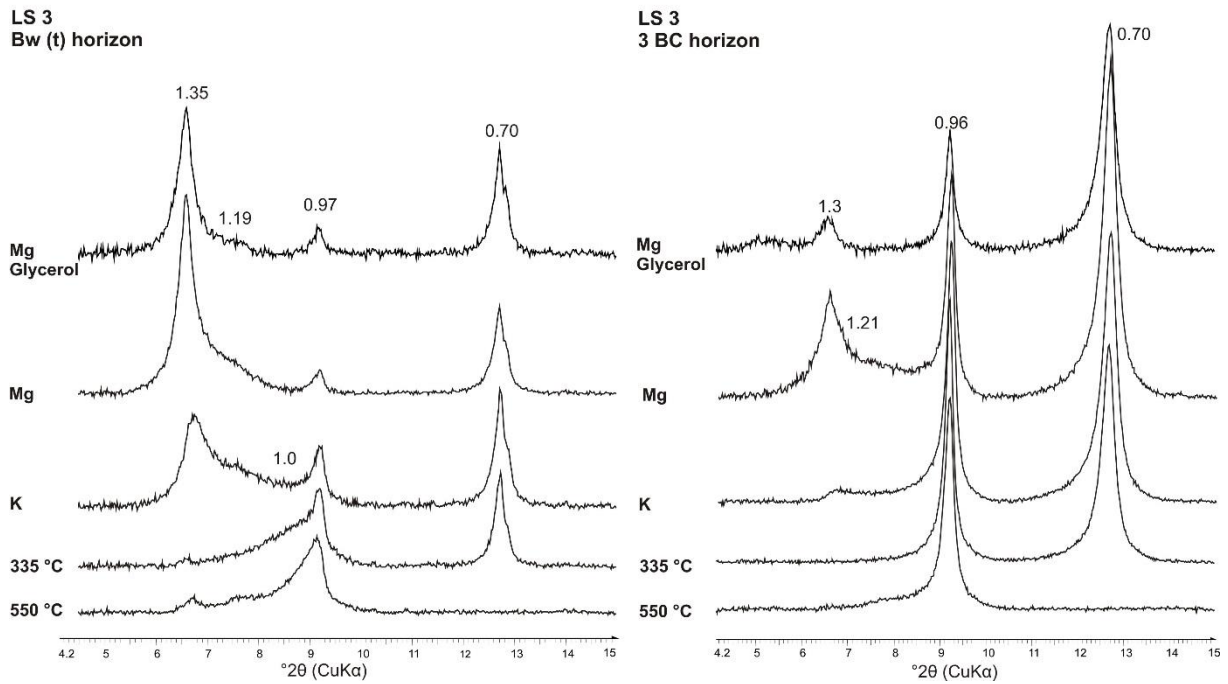
**Figure 23:** XRD pattern of horizons Bw (t) and 3BC of profile LS3.

LS3

The loess mantle (Bw(t) horizon) consists of the characteristic peaks of vermiculite, mica and kaolinite with a d-spacing of 1.35, 0.97 and 0.70 nm, respectively (see Figure 23, left). In the Mg- and glycerol-saturated samples a small peak at 1.19 is present, which is attributed to an interstratified mica-vermiculite (or mica-HIV). The Mg- and K-saturation exhibit smaller peaks between 1.35 and 0.97 nm, which is interpreted as interstratified mica-vermiculite or HIV. The presence of chlorite in this sample is assumed due to the small peak at 6.7°2θ in the 550°C heating treatment.

The transition horizon (2BC horizon) shows distinct peaks at 1.34, 0.96 and 0.70 nm in the Mg-saturated samples. These were assigned to vermiculite, mica and kaolinite, respectively. Between 1.34 and 0.96 nm interstratified mica-vermiculite or HIV material is assumed. The K-saturated sample also consists of a peak at 1.34 nm, which shifts towards 1.0 nm in the 335°C treatment and thus might be HIV or HIS. Besides, the presence of chlorite is indicated by the peak at 6.7°2θ in the 550°C heating treatment. In this treatment a peak at 1.14 nm was observed, which was not further identified.

The bedrock (3BC horizon) consists of a peak at 1.34 nm (vermiculite) and very sharp peaks at 0.96 (mica) and 0.70 nm (kaolinite) (see Figure 23, on the right). The presence of interstratified mica-vermiculite or HIV material is assumed due to the smaller peaks in the Mg treatment between 1.34 and 0.96 nm. In the K-saturated samples a small peak at 1.34 nm is present, which might be HIV or HIS. The granitic bedrock does not show any presence of chlorite.

In all three horizons of LS3 the presence of smectite is not observed.

LS4

The AE horizon of LS4 consists of vermiculite, mica and kaolinite, which show peaks at 1.34, 0.96 and 0.70 nm, respectively in the Mg-saturated samples. In the Mg and glycerol treated samples, a small peak at 1.73 is detected, which is smectite. In the K-saturated samples a peak at 1.34 nm is present, which is attributed to chlorite (or highly HIS) and one at 1.18 nm that is due to HIV or HIS. The presence of chlorite is confirmed due to the small peak at 1.34 nm in the 550°C treatment.

The transition horizon (2Btg1) exhibits distinct peaks in the Mg-saturated samples at 1.36 (vermiculite) and 0.70 nm (kaolinite). The small peak at 0.97 nm indicates mica. The presence of interstratified mica-vermiculite or HIV material is assumed. The Mg- and glycerol treated sample exhibits a distinct peak at 1.72 nm (smectite) and smaller peaks at 0.88 and 0.81 nm. The latter might be amphibole or the $d$(002) of smectite. The peak at 0.81 nm appears in all treatments. The K-saturated sample consists of smaller peaks between 1.36 and 0.97 nm, which most probable are HIS or HIV.

The bedrock (2BC horizon) exhibits a similar pattern like the transition horizon. Vermiculite and kaolinite are obviously present with distinct peaks at 1.36 and 0.70 nm in the Mg treatment. Also, interstratified mica-vermiculite or HIV material is present. The peak at 1.72 nm in the Mg-glycerol treatment is assigned to smectite while the smaller peaks at 0.87 and 0.81 nm might represent amphibole or the $d$(002) of smectite. Mica is present showing a peak at 0.96 nm in all treatments. The K-saturated sample consists of some smaller peaks between 1.36 and 0.96, which again might be HIS or HIV. The presence of chlorite in the transition horizon and in the bedrock is not observed.

LS5

The loess mantle of LS5 (AEg horizon) exhibits distinct peaks in the Mg treatment at 1.35, 0.96 and 0.70 nm which are assigned to vermiculite, mica and kaolinite, respectively. Between 1.34 and 0.96 nm interstratified mica-vermiculite or HIV material exists (1.16 nm) and a small peak at 0.61 nm is observed which probably is the $d$(002) of smectite. This peak is also visible in the Mg-glycerol treated sample but is not identified yet. Additional peaks in this treatment are at 1.80 and 1.69 nm (smectite). The K-saturated sample might comprise of HIV and HIS whereas the small peak at 1.32 nm in the 550°C treatment possibly shows the presence of chlorite.

The transition horizon (Btg1) has a distinct peak at 1.35 nm, which is assigned to vermiculite. Additional peaks in the Mg treatment are at 0.96 and 0.70 nm (mica and kaolinite). In this treatment the presence of interstratified mica-vermiculite or HIV material is assumed due to peaks at 1.55 and 1.24 nm. The Mg-glycerol treated sample exhibits a distinct, broad peak at 1.74 nm, which is obviously smectite.

A smaller, unknown peak is also observed at 0.90 nm. The K treatment revealed some peaks around 1.24 nm which might be HIS and HIV.

The bedrock (2CBtg horizon) consists of distinct peaks at 1.35, 0.96 and 0.70 nm in the Mg-saturated samples. Due to their behavior in all treatments the peaks are assigned to vermiculite, mica and kaolinite. The presence of interstratified mica-vermiculite or HIV material is assumed due to the broad peak around 1.35 nm. Moreover, in the Mg-glycerol treatment the broad peak is assigned to smectite and a small peak at 0.88 is observed but not identified. The K-saturated sample might consist of HIS and HIV due to the peaks around 1.13 nm.

Again, chlorite is not observed in the transition horizon and the bedrock of LS5.

### 6.3.1 $d$(060)

The reflections of $d$(060) allow a distinction between dioctahedral and trioctahedral types and thus give information about weathering processes in the soils. The $d$(060)can vary for a given mineral species because they depend on the composition of the octahedral sheet, the amount of Al in tetrahedral coordination, and the degree of tetrahedral tilt (Moore and Reynolds 1997). In the following sections the $d$(060) reflections of each horizon are described and compared. All XRD patterns from the $d$060 region with their modelled curves are found in the appendix, p. 94-98.

LS1

In profile LS1 (see Figure 24, left), trioctahedral species are found at 0.1560 and 0.1556 nm and between 0.1539 and 0.1534 nm. The sharp peak at 0.1542/0.1541 nm is most probably quartz. Moore and Reynolds (1997) describe that in this case another reflection at d = 0.182 nm must occur. This is confirmed looking at the powder plots from 9°2θ to 80°2θ, whereby a peak with the same intensity at 60°2θ appears (see appendix, p. 79). The small peak at 0.1525 nm in the 3BC horizon might be Fe-rich dioctahedral minerals (Fanning et al. 1989). The peak at 0.1509 nm (AE horizon) and 0.1508 nm (3 BC horizon) might be glauconite, a dioctahedral phyllosilicate. Furthermore, a quiet distinct peak is observed in the 2Btg/E horizon at 0.1505 nm, which might be montmorillonite (smectite) (Okrusch and Matthes 2014; Moore and Reynolds 1997). The sharp peak between 0.1501 and 0.1498 nm and the peak between 0.1490 and 0.1486 nm, which are present in all horizons of LS1, are interpreted as illite (muscovite) and kaolinite, respectively (Moore and Reynolds 1997). One can see that the proportion of trioctahedral and dioctahedral minerals varies throughout the profile. The trioctahedral species seem to decrease towards the bedrock. The proportion of dioctahedral to trioctahedral species is in all horizons higher. The transition horizon (2Btg/E) thereby has the highest dioctahedral proportion.

LS2

All horizons of LS2 exhibit a peak around 0.1558 nm, which is a trioctahedral mineral. The sharp peak at 0.1543-0.1540 nm is clearly assigned to quartz. Around 0.1527 nm some Fe-rich dioctahedral minerals are present (Fanning et al. 1989). The peak at around 0.1511 nm is identified as glauconite while montmorillonite (smectite) is characteristic between 0.1506 and 0.1496 nm (Moore and Reynolds 1997; Okrusch and Matthes 2014). The peak between 0.1500 and 0.1498 nm in all horizons is most probably illite, whereas the peak between 0.1491 and 0.1488 nm is assigned to kaolinite (Moore and Reynolds 1997). In profile LS2 the proportion of the dioctahedral minerals is higher in all horizons. One can say that the dioctahedral minerals decrease towards the soil surface, so do the trioctahedral mineral species.

LS3

In the horizon of LS3 a trioctahedral mineral around 0.1560 nm is present. Chlorite is assumed between 0.1549 and 0.1537 nm. A big, sharp peak in the 2BC and 3BC horizon is present around 0.1541 nm and a smaller peak in the BW(t) horizon exists at 0.1540. This is most probably quartz (Moore and Reynolds 1997). A small peak at around 0.1525 is assigned to Fe-rich dioctahedral minerals (Fanning et al. 1989). Additionally, smectite is detected between 0.1504 and 0.1494 nm. Illite is present in all horizon with peaks between 0.1501 and 0.1497 nm. Kaolinite is also present showing peaks between 0.1491 and 0.1486 nm (Moore and Reynolds 1997). In the profile LS3 the dioctahedral minerals show a higher proportion in the upper horizon BW(t) and decrease towards the bedrock. A substantial transformation from trioctahedral to dioctahedral minerals has taken place in LS3.
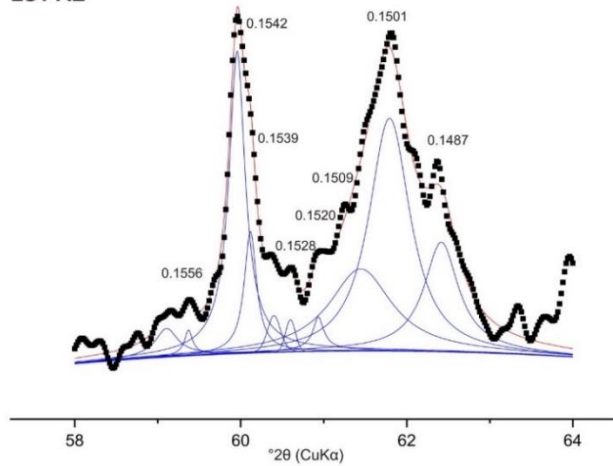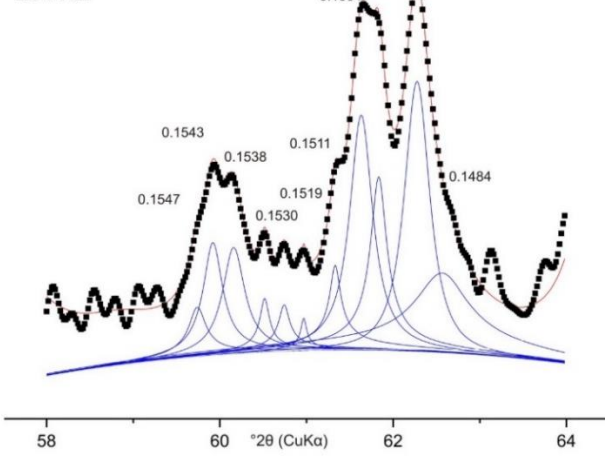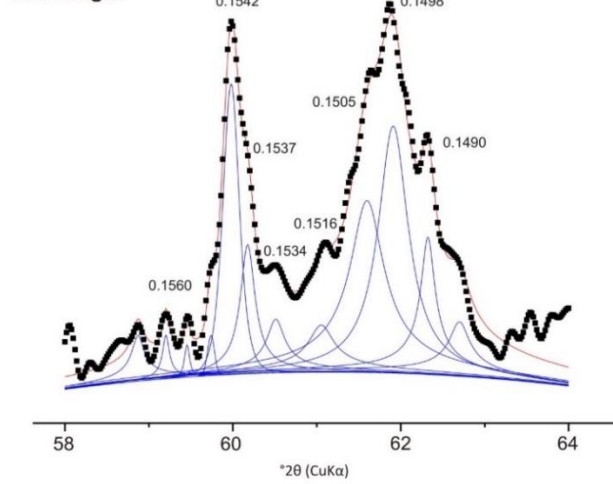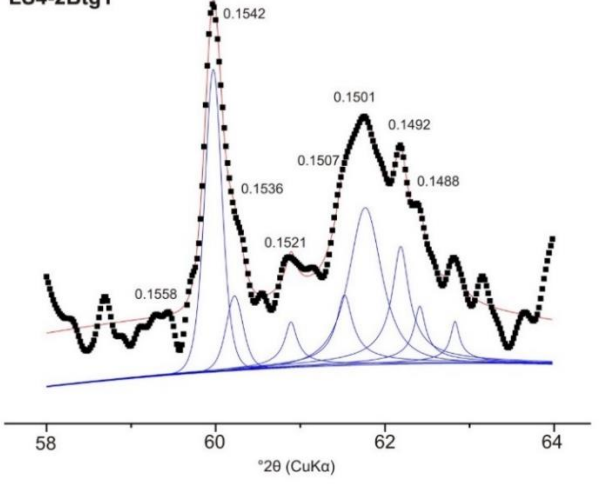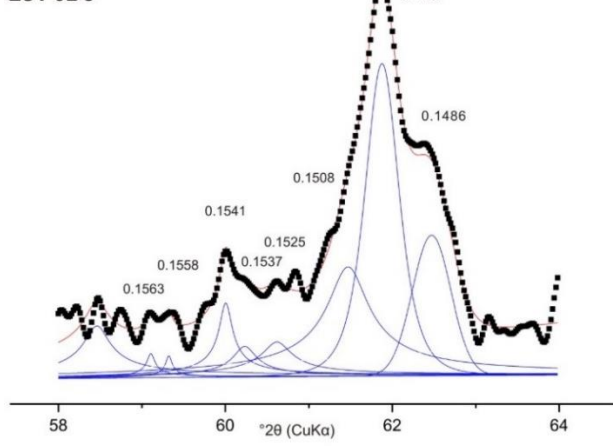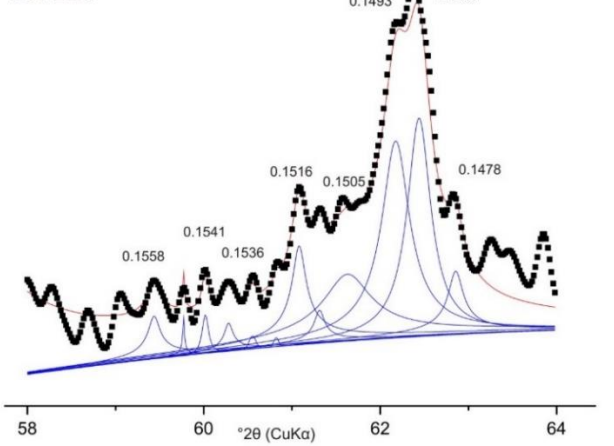
**Figure 24:** XRD pattern with modelled curves of the d060 region of LS1 (left) and LS5 (right). D-spacings are given in nm.

LS4

In all horizons of LS4, quartz is present (0.1543-0.1541 nm).  Between 0.1538 and 0.1536 nm peaks are detected, which might be biotite or chlorite. Between 0.1505 and 0.1492 nm the occurrence of montmorillonite is assumed. Illite is present with peaks between 0.1501 and 0.1493 nm. Further, kaolinite is identified with peaks between 0.1490 and 0.1487 nm in all horizons (Moore and Reynolds 1997). The trioctahedral minerals seem to decrease towards the bedrock. The dioctahedral minerals exhibit a higher proportion in the transition horizon (2Btg1) and the bedrock (2BC).

LS5

In profile LS5 the peak at 0.1541/0.1540 nm is clearly identified as quartz while the lower two horizons seem to consist of chlorite due to a peak around 0.1538 nm. In the region 0.1504-0.1493 nm montmorillonite most probably is present. Illite and kaolinite are identified due to peaks at 0.1499 nm and around 0.1488 nm, respectively (Moore and Reynolds 1997). The transition horizon has the highest occurrence of dioctahedral species and thus also a higher proportion of dioctahedral minerals. To conclude, throughout LS5 the dioctahedral species dominate.

### 6.3.2 Powder samples

The investigated powders samples between 2°2θ and 80°2θ are dominated by quartz, muscovite and kaolinite. Accessory minerals are: plagioclase, orthoclase amphibole, biotite, muscovite, magnetite, ilmenite, rutile, garnet and chlorite. Traces of epidote, titanite, kyanite, zircon, albite, ulvospinell and olivine were detected in some samples. An example of the XRD pattern is displayed in Figure 25. All XRD patterns and the detailed table can be found in the appendix, p. 79-85.
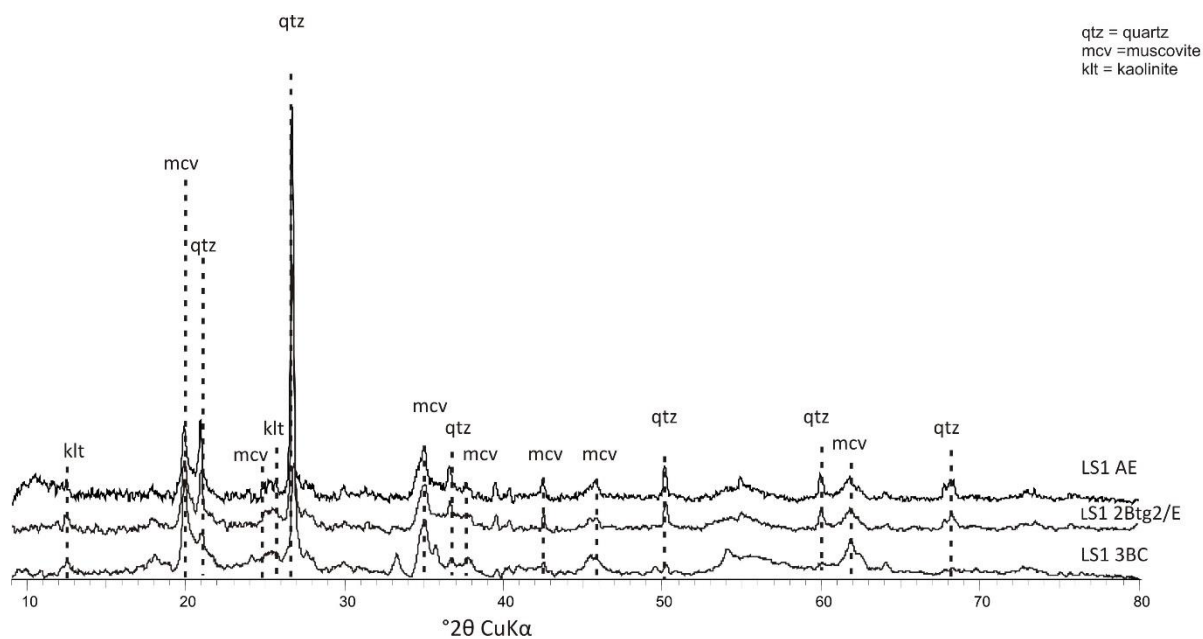
**Figure 25:** Identified polytypes of LS1. Main components are quartz, muscovite and kaolinite.

LS1 shows a quartz content between 36 and 58 %. Muscovite and kaolinite are present in the AE and 2Btg2/E horizons with 8 % and around 6 % respectively. The bedrock (3BC) consists of a higher content of muscovite (16 %) and has a magnetite content of 9 %.

LS2 reveals quartz contents between 53 % and 59 % while the kaolinite content lays between 5 % and 8 %. Muscovite is slightly decreasing towards the surface. In the bedrock (3BC), 13 % are measured while in the loess mantle (E), a content of 9 % occurs.

The quartz content in LS3 varies between 40 % and 64 % and is decreasing towards the soil surface. The muscovite contents lay between 6 % and 15 % while kaolinite has percentages of 6 and 14. The kaolinite percentage in the transition horizon (2BC) is the lowest of this profile.

Moreover, in LS4 quartz the contents lay between 28 % (in the loess mantle) and 51 % (in the transition horizon). Muscovite is present with a content of 6 % in the transition horizon (2Btg1), 8 % in the bedrock (2BC) and 12 % in the loess mantle (AE). Kaolinite varies between 13 % (in the transition horizon) and 31 % (in the loess mantle).

In LS5, the quartz contents vary between 40 % (in the bedrock) and 57 % (in the loess mantle). The second most occurring mineral is kaolinite with contents between 12 % and 16 %. The kaolinite content is increasing towards the bedrock. In the loess mantle (AEg), orthoclase is occurring with 4 % while the lower two horizons reveal muscovite as third most mineral. In the Eg and 2CBtg horizons, the muscovite contents are 7 % and 11 %, respectively.

## 6.4 DRIFT

The results of the DRIFT measurements were primarily conducted to confirm the presence of kaolinite. Therefore, a better distinction between kaolinite and chlorite (XRD) can be performed. The table with the detailed results is found in the appendix (p. 99 & 100). Calcite and dolomite are not part of the interpretation because the pH is lower than 7.

LS1

The peaks at 348, 474, 3620, 3652 and 3694 cm$^{-1}$ confirm the presence of kaolinite in all horizons of LS1. The presence of chlorite is assumed due to peaks at 750, 3428 and 3575 cm$^{-1}$ (Farmer 1974). Chlorite seems to increase towards the surface. Further, in all horizons gibbsite, imogolite, muscovite and AlMgOH are observed. The upper horizon consists of octahedral Mg/Fe and probably dioctahedral smectite.

LS2

Profile LS2 revealed the presence of kaolinite due to peaks at 474, 3620, 3652 and 3694 cm$^{-1}$. The presence of chlorite is confirmed exhibiting peaks at 750, 3428 and 3676 cm$^{-1}$ (Farmer 1974). The transition horizon of LS2 (2Bt1) shows the highest occurrence of chlorite. Additional identified minerals are gibbsite, imogolite, illite, octahedral Mg/Fe and dioctahedral smectite. The transition horizon (2Bt1) and the bedrock (3BC) show presence of muscovite while the presence of AlMgOH in the bedrock is assumed.

LS3

Kaolinite occurs in profile LS3. The confirmation Therefore are the peaks at 348, 474, 3620, 3652 and 3694 cm$^{-1}$. Additionally, also chlorite is identified showing peaks at 750, 3428, 3575 and 3676 cm$^{-1}$ (Farmer 1974). In this profile the transition horizon (2 BC) and bedrock (3BC) are characterized by a higher chlorite content. The following clay minerals occur in LS3: gibbsite, illite, octahedral Mg/Fe and muscovite. Imogolite was present in the upper two horizons and is assumed in the bedrock. Dioctahedral smectite is assumed in the loess mantle and clearly exists in the lower two horizons. Besides, AlMgOH is not found in the transition horizon while it was present above and below.

LS4

The presence of kaolinite and chlorite are also confirmed in profile LS4. Kaolinite shows peaks at 348, 474, 3620, 3652 and 3694 cm$^{-1}$ whereas the characteristic peaks for chlorite are found or assumed at 750, 3428 and 3575 cm$^{-1}$ (Farmer 1974). The peak at 750 cm$^{-1}$ is found in all three horizons whereas the others are only assumed. The transition horizon has the highest occurrence of chlorite.

Additional detected clay minerals are: imogolite, illite, muscovite and dioctahedral smectite. Octahedral Mg/Fe is only confirmed in the loess mantle (AE) and assumed in the bedrock (2BC). AlMgOH is not detected in the transition horizon (2Btg1) but assumed above and below.

LS5

Profile LS5 shows presence of kaolinite and chlorite. The kaolinite peaks are at 348, 474, 3620, 3652 and 3694 cm$^{-1}$. Chlorite was detected due to peaks at 750, 3428 and 3575 cm$^{-1}$ (Farmer 1974). Chlorite exists throughout the profile. Gibbsite, illite and muscovite is found in all horizons of LS5. Imogolite occurs in the upper two horizons (AEg and Btg1) while the presence of AlMgOH is only assumed in the loess mantle.

# 7. Interpretation and Discussion

## 7. 1 Physical and geochemical parameters

Regarding the particle sizes, differences between the horizons are obvious. As expected, the loess mantles present the highest silt contents within the profiles because silt is one of the main characteristics of loess. The silt content decreases towards the bedrock in each profile while the sand content is increasing with greater depth. The clay content in the five profiles varies considerably.

LS1 is an Endoskeletic Luvisol. This soil type is known for a clay-depleted horizon above an illuvial clay-rich B horizon (Schaetzl and Anderson 2005). Already Waroszewski et al. (2017) have stated that through moderate aeolian silt admixture Luvisols or Alisols can develop. Through aeolian silt addition the conditions for clay eluviation/illuviation processes are favored. Moreover, soil formation and evolution is closely related to the thickness of the loess mantle (Jacobs et al. 2012).

In LS1, a clear clay accumulation was observed in the transition horizon (2Btg2/E) where a higher proportion of dioctahedral clay mineral species also occurred. Herein, we interpret that the loess mantle is already further developed/ weathered and its components, like clay and heavy minerals, were transported progressively downwards, amongst others, by water. Regarding LS2, which is also an Endoskeletic Luvisol, the topography is a major factor. LS2 is situated on a midslope of Mt. Ślęża which has a slope of 12°. The loess mantle (E horizon) is weakly developed in this profile compared to the others and exhibits a thickness of 5 cm. Herein, the conclusion is that the slope is prone to erosion and thus pedogenesis is reduced. Another indicator for erosional processes at the site is that the transition zone is relatively skeletal and no regolith is present. Nevertheless, clay translocation occurs in LS2. The eluviated clays are accumulated in the 2Bt1 and 3BC horizon. This coincides with the downward increasing dioctahedral species. The profile LS3, lying on granite on a summit/shoulder, does not provide an E horizon. Hence, the mixing of aeolian silt with acidic granite regolith resulted in the formation of an Alisol (Waroszewski et al. 2017). LS3 is the only investigated profile that showed the highest clay content and the occurrence of dioctahedral minerals in the loess mantle. A decrease in the clay content was observed towards the bedrock. In the 2BC horizon a small clay illuviation seems possible whereas the 3BC horizon is dominated by in situ weathering. In addition, LS4 was identified as an Endoskeletic Luvisol and lays on a summit/shoulder. In this profile similar soil processes as in LS1 and LS2 were observed. In the loess mantle (AE horizon) the clay is eluviated and accumulated in the 2Btg1 horizon. For LS5 an Eutric Luvic Albic Folic Stagnosol on a backslope was identified. Stagnosols develop when former argic horizons are buried with eroded loess material (Waroszewski et al. 2017). On this site clay accumulation was noticed in the transition horizon (Btg1) and the underlaying substrate (2CBtg). A higher proportion of dioctahedral clay minerals occurred in the former.

LS5 is situated on a backslope with an inclination of 8° and thus a higher erosion is assumed at the surface. Indicators are a quite thin loess cover and a shallow AEg horizon.

The clay accumulation zones in the described profiles are also identifiable due to angular blocky structure and mostly firm consistency.

Regarding the geochemistry, several parameters were analyzed. All investigated soil profiles showed a low carbonate content and a low pH. The highest Hf/Zr concentration was identified in the loess mantles of the profiles. Scheib et al. (2014) describe the relationship of Hf and Zr and see these elements as indicators for aeolian deposits. Zr displays very low mobility under most environmental conditions, mainly due to the very high stability of the principal host mineral zircon (Ioannides et al. 2015). Zircon is accumulated through different processes while less dense and resistant minerals are removed. The zircon grains remain stable due to their resistant nature and their high density (4.6 to 4.7 g/cm$^3$)(Scheib et al. 2014). A higher occurrence of zircon in the loess mantles and the transition horizons was also detected by SEM in LS3 and LS4. The high Hf/Zr concentration supports the fact that the mantles of the five profiles have an aeolian origin. In the different profiles, the Hf/Zr concentrations decrease towards the bedrock. In the transition horizon, the higher concentrations are remaining because loess is incorporated into greater depth. These results show clearly how the aeolian material and the undelaying substrate are mixed in the transition zone.

Regarding the percentages of $Fe_2O_3$ and $TiO_2$, generally less $Fe_2O_3$ was found in the loess mantles than in the transition horizons and bedrocks. Schatz et al. (2015) argue that Fe is relatively enriched during pedogenesis and alkaline metals such as Na, K, Ca and Mg are depleted. $TiO_2$ is one of the most stable oxides (Raczyk et al. 2015). Újvári et al. (2008) defined an average loess composition which has a $Fe_2O_3$ percentage of 3.7 and a $TiO_2$ percentage of 0.69. The loess mantles of the investigated profiles are comparable showing similar $TiO_2$ percentages but slightly lower $Fe_2O_3$ percentages. In the transition zones the incorporation of the loess is visible due to similar $TiO_2$ percentages. The differences found in the oxides regarding the underlying substrates are explained by the different chemical compositions of the bedrocks. The ultramafic serpentinite is extremely rich in iron likewise basalt for example (Schaetzl and Anderson 2005). The high $Fe_2O_3$ in LS4 (on glacio-fluvial material) might be explained with the local serpentinite material. Quartz-rich substrates, like the Permian sandstone (LS1) and granite (LS3), exhibit lower $Fe_2O_3$ percentages.

The Ti/Zr ratio is applied to determine admixture of another sedimentological component (Sauer et al. 2016). Moreover dust provenance can be investigated by studying weathering-inert elements such as Si, Al, Ti and Zr and calculating their ratios (Profe et al. 2018).

In all five profiles changes in the ratio with increasing depth can be found. While the Ti/Zr ratios in the loess mantles are between 12-17, the ratios increase towards the underlying substrate. The latter have a greater range, between 19-225, which shows the variability of the underlying substrates. The high ratio of the profile on glacio-fluvial material is especially interesting, which possibly is the result of the heterogenic material. All profiles obviously exhibit differences in the Ti/Zr ratios in the loess mantle, transition horizon and the underlying substrate. Regarding the provenance of the loess mantles of the five profiles, comparable ratios were found in Germany. Schnetger (1992) investigated loess in Hessia and Lower Saxony and the retrieved Ti and Zr values led to a Ti/Zr ratio of 13.25 (Újvári et al. 2008). The Ti/Zr ratios calculated for the loess mantles of the five profiles are moderately comparable and probably were deposited when the Scandinavian ice sheet covered northern Europe during the LGM. Still, the Ti/Zr ratios of the five profiles vary and Therefore different provenances might be considered.

Additionally, the K/Rb ratios of the different horizons for each profile were calculated. This ratio is commonly applied to determine changes in lithogenic sources (Silva-Sánchez et al. 2015). In none of the investigated profiles constant K/Rb ratios were found. In most profiles they showed a decrease with increasing depth. The loess mantles had a ratio between 242 and 358 while the ratios of the underlying substrates were between 233 and 343. The K/Rb ratio calculated from the data of Schnetger (1992) was 269 and laid again in the range of the loess mantles (Újvári et al. 2008). The closest concordance with the reference ratio was LS5 which is the northern and western most of all profiles. Consequently, a similar loess source as in Germany might be assumed. The loess mantles of the profiles around Mt. Ślęża (LS2-LS4) certainly have the same provenance whereas the loess of LS1 in the southern lying Kłodzko basin might originate from the Sudety mountains.

## 7. 2 Heavy minerals

In soils, heavy minerals are important nutrient sources and possible indicators of sediment provenance (Lång 2000). The latter is especially important for this thesis to distinguish between the loess mantle, the transition horizon and the underlying substrate.

In LS1 garnet is present in the upper two horizons but was not found in the bedrock. Therefore, it can be interpreted as a signal of loess. Garnet is enriched in the transition horizon which is a sign that downward movements occurred, possibly by percolating water or bioturbation. Other heavy minerals which seem to reflect the loess are amphibole, apatite, chlorite, epidote, rutile. However, the loess generally is derived from a mafic source but also from some allogenic metamorphic material ($Al_2SiO_5$) is present, mainly in the transition horizon and the underlying substrate. Regarding the other heavy minerals, ulvospinel and xenotime seem to originate from the underlying Permian sandstone. In addition, ulvospinel is an indicator that basalt exists (personal communication J. Kierczak).

In general, the bedrock 3BC has a mafic origin. The high Fe-oxide content which is around 29 % throughout the profile, is traced back to the Permian sandstone. Besides, the oxidized iron minerals are responsible for the characteristic red color (Schaetzl and Anderson 2005).

The heavy mineral assemblage of LS2 is dominated by magnesiochromite and magnetite, which seem to originate from both the loess mantle and the underlying serpentinite. Amphibole is an input from the loess because it was not observed in the bedrock samples and shows a slight decrease from the loess mantle to the transition horizon. Minerals from the epidote-group also occur throughout the profile and thus are present in the loess mantle and the underlying substrate. Moreover, the loess mantle hosts garnet but minerals like ilmenite, olivine and pyroxene are derived from the underlying serpentinite. Zircon and rutile are more abundant in the lower horizons but are not common weathering products of serpentinite. They might be translocated by water from the loess cover into greater depths.

Amphibole, minerals from the epidote-group and zircon seem to clearly originate from the loess mantle in LS3. Also, Fe-oxide, garnet, ilmenite, magnesiochromite and magnetite are interpreted as signals from the loess. Otherwise, biotite, monazite, rutile and xenotime are clearly weathering products from the underlying granite. The rutile signal in the 2BC horizon with 66.7 % is exceptionally high. However, heavy minerals like monazite and xenotime are characteristic for the granite of Mt. Ślęża (personal communication J. Kierczak).

The profile LS4, which is located on glacio-fluvial material, exhibits small amounts of different heavy minerals throughout the profile. This can be explained by considering the origin of the underlying substrate. The glacio-fluvial material originates from Scandinavia and was transported for several kilometers. It has a granitic and serpentinite character (Waroszewski et al. 2017). Apatite, biotite, garnet, Fe-oxide, magnesiochromite and magnetite, monazite, rutile and zircon are clear signals for the loess. Amphibole and ilmenite have constant amounts throughout the profile and occur in the loess mantle and the underlying substrate. Epidote-group minerals are definitely originating from the glacio-fluvial material. The latter also contain small amounts of pumpellyite and zoisite, which are not present in the upper two horizons.

LS5, the profile on basalt, shows the following heavy minerals as loess signals: minerals from the epidote-group, rutile, spinel and zircon. Furthermore, amphibole, Fe-oxide, ilmenite and pumpellyite are present throughout the profile. They show similar amounts and seem to occur in the loess mantle and the basalt. Monazite and titanite occur in higher amounts in the transition horizon. There an input from allogenic material is observed and might be explained by downward water movement.

To conclude, olivine and pyroxene, staurolite and ulvospinel are interpreted as signals from the bedrock. They show a mafic character which coincides with the basalt.

## 7.3 Clay minerals

All loess mantles of the investigated profiles have the following secondary minerals in common: vermiculite, mica, kaolinite and chlorite. Besides, HIV or interstratified mica-vermiculite was detected. Kalm et al. (1996) reported for a loess sequence of the Chinese loess plateau similar minerals, namely illite (mica), kaolinite, mixed layer chlorite-vermiculite, chlorite and small amounts of smectite with traces of mixed layer illite/smectite. Whereas the large European loess deposits are derived mainly form till material (Catt 1988). "They are composed mostly of vermiculite, smectite/illite and illite/smectite; and kaolinite" (Velde and Meunier 2008, p. 308). For the silt sized fraction in French deposits, illite and chlorite plus some kaolinite were reported (Hardy et al. 1999; Jamagne 1973). Even though the investigated profiles mainly had an uniform clay mineralogy in the loess mantles, small differences between the horizons of each profile and differences between the profiles were observed.

HIV or interstratified mica-vermiculite was observed in all investigated samples and is Therefore highlighted here. As previously discussed, low carbonate contents were recognized in the five profiles. After the removal of carbonates in loess soils, the transformation from mica and/or vermiculite and/or smectite to hydroxy-interlayered minerals is an important process in temperate climates. The lack of carbonates or low carbonate contents further progress the dispersion and translocation of clay particles to greater depths. Hence, the formation of Luvisols is the result (Drewnik et al. 2014). The formation of HIV or interstratified mica-vermiculite in the five profiles is predominantly seen as an impact of the loess mantles.

The proportion of mica to vermiculite is higher throughout LS1, situated on Permian sandstone. The interpretation Therefore is that mica is not strongly weathered and transformed into vermiculite. Moreover, rather high amounts of kaolinite are observed in the loess mantle. It indicates that this clay mineral is inherited from an allogenic source but also is transformed from the Permian sandstone through weathering. Kaolinite forms when other silicates like feldspars or micas break down completely (Strawn et al. 2015). This coincides with the Permian sandstone which mainly consists of quartz, feldspar and rock fragments (Britannica 2018c).

The peak intensity of smectite is generally increasing towards the surface. High smectite contents are often associated with a lower mica signal. Hence, a transformation of mica into smectite due to weathering is suggested (Egli et al. 2006). In general, chlorite decreases towards the bedrock.

Considering the DRIFT-measurements and the XRD-pattern in the $d$060 region, chlorite must also occur in the 3BC horizon but with relatively smaller amounts compared to the upper two horizons. Consequently, the decrease of chlorite towards the underlying bedrock might be explained with its transformation into vermiculite (Wilson 1999).

The bedrock of LS2 is serpentinite, which consists mainly of serpentine minerals like lizardit, antigorite or chrysotile (Okrusch and Matthes 2014). In the underlying substrate of LS2 the occurrence of chlorite is stronger compared to the substrates of the other profiles. The presence of chlorite is also confirmed by the DRIFT-measurements. Thus, the presence of chlorite is seen as a signal of the underlying serpentine bedrock. Also Velde (1995) describes the formation of chlorite on a serpentinite saprolite. Chlorite is also found in the upper layers which reflects the incorporation from the loess mantle. An increase in the intensity of the vermiculite peak towards the surface is observed while the mica peak decreases. Hence, a transformation from mica into vermiculite is assumed (Wilson 1999).

In LS2 the presence of smectite is confirmed with XRD- and DRIFT-measurements. The plots between 4°2θ-15 °2θ indicate an increase from the loess mantle towards the bedrock. This phenomenon can be explained looking at the E horizon, where clay was washed out. The clay was illuviated into greater depths and thus higher amounts of smectite are found. But the underlying serpentinite is also prone to produce smectite (Velde 1995).

Looking at LS3, kaolinite is increasing toward the bedrock. As previously explained, kaolinite forms when other silicates like feldspars or micas break down completely. Another process where kaolinite is formed, is its precipitation from $Al^{3+}$ and $Si^{4+}$ ions in solution (Strawn et al. 2015). LS3 is situated on granite which consists of feldspar, micas and quartz (Okrusch and Matthes 2014). The higher presence of kaolinite, especially in the underlying substrate, might result from the weathering of granite. Moreover, in LS3 an increase in the intensity of the vermiculite peak towards the surface is observed with a concomitant decrease of the mica peak. This is explained by a transformation of mica into vermiculite (Wilson 1999). The increase of the mica peak intensity towards the bedrock is also explained by weathering of the granitic bedrock. Nesbitt and Young (1989) highlight that illite is a common weathering product of K-feldspar.

As observed in previous profiles, the amount of chlorite is decreasing with increasing depth. It seems to disappear in the 3BC horizon of LS3. Including the DRIFT-measurements, chlorite is present in all horizons of LS3 but in smaller amounts. The decrease towards the bedrock might be explained with its transformation into vermiculite (Nesbitt and Young 1989).

Smectite seems to be completely absent in LS3 when looking at the 4°2θ - 15 °2θ plots. Considering the DRIFT-measurements and the *d*060 region, smectite occurs in smaller amounts. One explanation might be that the loess mantle is already considerably eroded and the loess which remains, reflects the lower part of the former cover. Hence, smectite which is a mineral of intermediately weathered soils, was already removed (Strawn et al. 2015). Poormasoomi and Ramezanpour (2010) did not find smectite in a soil profile on granite, whereas the profile on andesitic basalt consisted of the discussed clay mineral. Consequently, a correlation with the underlying granite and the absence of smectite must be considered.

In LS4 the same phenomenon like in the E horizon of LS2 is observed. Relatively small amounts of smectite are found in the AE horizon of LS4 but higher amounts of smectite occur at greater depths. The explanation is again that the clay was illuviated downwards and smectite was enriched in the 2Btg1 and 2BC horizon. The underlying substrate of LS4 is glacio-fluvial material which mostly comprises of rounded, reddish Scandinavian granites and local serpentinites (Waroszewski et al. 2017). The amphibole peak at 0.81 nm in the 2Btg1 and the 2BC horizon is clearly originating from the bedrock. In the heavy mineral fraction of the two mentioned layers amphibole was also found. The intensity of the kaolinite peak is the highest in the underlying substrate (2BC) and might be explained with the weathering of the granitic components of the glacio-fluvial material (see also LS3). Mica and vermiculite show similar intensities throughout the profile. Mica (illite) might be a weathering product of the granitic part of the fluvio-glacial material but is also inherited from the loess. Vermiculite might be the transformation product of biotite and chlorite (Nesbitt and Young 1989).

In LS5 a transformation from mica to vermiculite toward the soil surface is observed. In this profile, the relatively high amounts of smectite in the Btg1 and 2CBtg horizon are notable. Most probably smectite was translocated by percolating water from the AEg horizon to the underlying horizons. It is primarily seen as a weathering product of the loess. The vermiculite peak exhibits a higher intensity than the mica peak in the AEg horizon with an opposite peak pattern at the bedrock (2CBtg horizon). Poormasoomi and Ramezanpour (2010) report for their soil profile on andesitic basalt the following clay minerals: mica, kaolinite, vermiculite and smectite. These are the weathering products of primary minerals coming from the basalt. In this study the mentioned minerals seem to originate from the bedrock but are also inherited from the loess because they are present in the AEg horizon.

Generally, in this thesis the focus was mainly on the pedosphere and lithosphere. Velde and Meunier (2008) state that the soil-plant interaction zone (A horizon) also plays an important role regarding the clay transformation, which was not considered here.

# 8. Conclusion

In this thesis five loess mantled soils on different underlying substrates were analyzed and compared. One of the main research questions was how the loess mantle and the underlying substrate exert influence on pedogenesis and soil processes. Considering the results, several phenomena were observed. The profiles LS1, LS2 and LS4 were identified as Luvisols and generally showed clay translocation features in the subsoil. The morphology of the investigated soils is characterized by an E horizon where the clay was eluviated with a concomitant illuviation into the underlying Btg horizon. This process was mainly reflected in the accumulation of dioctahedral clay minerals in the lower horizons. Usually, a higher amount of smectite was observed in the Btg horizons of the discussed profiles. Smectite is a secondary, pedogenic clay mineral and is thus easily transported by percolating meteoric water (Schaetzl and Anderson 2005). LS3, with an Alisol as soil type, showed a high accumulation of dioctahedral clay minerals in the loess mantle (Bw(t) horizon). The Stagnosol of LS5 also had an AEg horizon and an underlying Btg horizon. Similar soil processes (clay translocation) as in the Luvisols were observed here. Furthermore, the topography shows a correlation with the thickness of the loess mantles. The profiles situated on mid- or backslope (LS2 and LS5) having a dip slope between 8 and 12° exhibit thinner loess covers. This is explained by the steep slopes which inhibited the formation of a regolith before loess deposition. Due to the aeolian silt addition the slopes were stabilized but the loess mantles were eroded and are these days rather thin.

Regarding the question if the formation or transformation of phyllosilicates is detected, several observations were made. In all investigated profiles a transformation from chlorite and/or mica to vermiculite and smectite is assumed. Furthermore, the (neo)formation of HIV or interstratified mica-vermiculite occurred in all profiles and is the main result of the loess mantles. The acidic soil environment promotes this formation. In general, the loess mantles had the following clay minerals in common: kaolinite, mica, vermiculite, smectite, chlorite and HIV or interstratified mica-vermiculite. In LS3 smectite was not found in the whole profile, which is explained by erosional processes of the loess mantle. Based on Strawn et al. (2015) vermiculite, illite (mica), chlorite and smectite are predominant in intermediately weathered soils whereas kaolinite is a signal for advanced weathered soils.

Moreover, the bedrocks have the affinity to form their characteristic clay minerals. For the Permian sandstone higher kaolinite amounts were identified which are explained by the weathering of quartz and feldspar. The underlying serpentinite delivers more chlorite while in the granitic bedrock higher amounts of kaolinite and mica were observed. Furthermore, the glacio-fluvial material produced more amphibole, kaolinite and mica in the lowest horizon where the weathering of the basalt might be reflected in its higher smectite amounts.

The second research question incorporated if the discontinuities found in the soil texture and the soil geomorphology are also reflected in other parameters. Herein, we can see that the stated discontinuities are also found in the clay and heavy mineralogy and in the physical and geochemical parameters. The clay mineralogy of the five profiles was already discussed above and clear signals from the loess mantles and the bedrocks were highlighted. Regarding the heavy mineralogy, the discontinuities are obvious but differ from profile to profile. Hence, the provenance of the loess mantles might differ. Furthermore, the transition zones commonly have imprints from the loess mantles but also from the bedrock and Therefore highlight their mixing. The physical parameters are clearly seen in the grain sizes while the geochemical parameters are found in the Hf/Zr concentrations, the $Fe_2O_3$ and $TiO_2$ percentages and finally the Ti/Zr and K/Rb ratios. In all profiles the loess mantle, transition horizon and the underlying substrate were separable from each other, analyzing the mentioned parameters.

The final research question dealt with the origin of the loess mantles and if they are originating from the same source or if they have different provenances. Answering this question has turned out to be difficult. The Ti/Zr and K/Rb ratios exhibit small differences in the loess mantles but had comparable ratios found in Hessia and Lower Saxony in Germany. Thus, the provenance from vegetation-free periglacial areas during the LGM when the Scandinavian ice sheet covered northern Europe still seems very likely. Due to the calculated ratios, LS5, which is the northern and western most profile, showed the closest relation to the ratios from Germany. Hence, a similar loess source might be assumed. The profiles settled around Mt. Ślęża (LS2-LS4) seem to have the same loess source whereby the loess mantle of the southern lying LS1 might originate from the denudated Sudety mountains. For a conclusive answer more data is needed.

To conclude, soil processes like clay translocation are clearly reflected in the clay mineralogy but also the topography plays a key role in soil development. The loess mantle and its secondary clays and the further mixing of the loess with the underlying substrate have an influence on soil formation. Furthermore, the different underlying substrates have their characteristic weathering products which are not only reflected in the clay and the heavy mineralogy but also in the geochemical and physical parameters.

# 9. Acknowledgements

# 10. Publication bibliography

Badura, J. (2006): Pradolina wroclawsko-magdeburska i jej znaczenie w paleogeografii plenivistulianu Polski SW. In *Morawski, W. (Ed.), Plejstocen poludniowej Warmii i zachodnich Mazur na tle struktur podloza. 13 Konferencja stratygrafia plejstocenu Polski, Maróz, 4-8 wrzesnia 2006*, pp. 32–35.

Badura, J. (Ed.) (2011): Sources of loess deposits for the foreland of Central European Highlands. Jary, Z. (Ed.), Closing the Gap - North Carpathian Loess Traverse in the Eurasian Loess Belt: International Workshop, 6th Loess Seminar in Wroclaw, May 16-21 2011. Abstract and Field Guide Book. Institute of Geography and Regional Development, University of Wroclaw.

Badura, J.; Jary, Z.; Smalley, I. (2013): Sources of loess material for deposits in Poland and parts of Central Europe. The lost Big River. In *Quaternary International* 296, pp. 15–22. DOI: 10.1016/j.quaint.2012.06.019.

Boxleitner, M.; Musso, A.; Waroszewski, J.; Malkiewicz, M.; Maisch, M.; Dahms, D. et al. (2017): Late Pleistocene – Holocene surface processes and landscape evolution in the central Swiss Alps. In *Geomorphology* 295, pp. 306–322. DOI: 10.1016/j.geomorph.2017.07.006.

Bridges, N. T.; Muhs, D. R. (2012): Duststones on Mars: source, transport, deposition, and erosion. In *Grotzinger,J.,Milliken,R.(Eds.), Sedimentary Geology of Mars, vol. 102. SEPM Special Publication 5*, pp. 169–182.

Brindley, G. W. (1980): Quantitative x-ray mineral analysis of clays. In G. W. Brindley and G. Brown (eds.) Crystal Structures of Clay Minerals and their X-Ray Identification. Monograph no. 5. Mineralogical Society, London.

Catt, J. A. (Ed.) (1988): Loess- Its formation, transport and economic significance. With assistance of A. Lerman, Meybeck, M. (eds.) Physical and Chemical Weathering in Geochemical Cycles. Dordrecht: Springer Netherlands.

Catt, J.A (2001): The agricultural importance of loess. In *Earth-Science Reviews* 54 (1-3), pp. 213–229. DOI: 10.1016/S0012-8252(01)00049-6.

Dahms, D.; Egli, M. (2016): Carbonate and elemental accumulation rates in arid soils of mid-to-late Pleistocene outwash terraces, southeastern Wind River Range, Wyoming, USA. In *Chemical Geology* 446, pp. 147–162. DOI: 10.1016/j.chemgeo.2015.12.006.

Drewnik, Marek; Skiba, Michał; Szymański, Wojciech; Żyła, Marcin (2014): Mineral composition vs. soil forming processes in loess soils — A case study from Kraków (Southern Poland). In *CATENA* 119, pp. 166–173. DOI: 10.1016/j.catena.2014.02.012.

Egli, M.; Röthlisberger, S.; Brandová, D.; Keller T.; de Castro Portes R. (2017): Geochronology laboratory methods. Zurich.

Egli, Markus; Mirabella, Aldo; Sartori, Giacomo; Zanelli, Remo; Bischof, Simone (2006): Effect of north and south exposure on weathering rates and clay mineral formation in Alpine soils. In *CATENA* 67 (3), pp. 155–174. DOI: 10.1016/j.catena.2006.02.010.

Fanning, D. S.; Keramidas, V. Z.; and El-Desoky, M. A. (1989): Micas. In *Minerals in Soil Environment 2nd edition (J.B. Dixon and S.B. Weed, editors). Soil Science Society of America, Madison, Wisconsin*, pp. 551–634.

FAO (2006): Guidelines for Soil Description.

Farmer, V. C. (1974): Layer Silicates. In *Farmer, V.C. (Ed.)Infrared Spectra of Minerals, Monograph 4. Mineralogical Society, London*, pp. 331–363.

Flint, R. F. (1971): Glacial and Quaternary Geology.: John Wiley & Sons Inc., New York.

Grahmann, R. (1932): Der Löss in Europa. In *Mitteilung der Gesellschaft für Erdkunde Leipzig* (51), pp. 5–24.

Haase, D.; Fink, J.; Haase, G.; Ruske, R.; Pécsi, M.; Richter, H. et al. (2007): Loess in Europe—its spatial distribution based on a European Loess Map, scale 1. 2,500,000. In *Quaternary Science Reviews* 26 (9-10), pp. 1301–1312. DOI: 10.1016/j.quascirev.2007.02.003.

Hardy, M.; Jamagne, M.; Elsass, F.; Robert, M.; Chesneau, D. (1999): Mineralogical development of the silt fractions of a Podzoluvisol on loess in the Paris Basin (France). In *European Journal of Soil Science* 50 (3), pp. 443–456. DOI: 10.1046/j.1365-2389.1999.00246.x.

Ioannides, K.; Stamoulis, K.; Papachristodoulou, C.; Tziamou, E.; Markantonaki, C.; Tsodoulos, I. (2015): Distribution of heavy metals in sediment cores of Lake Pamvotis (Greece). A pollution and potential risk assessment. In *Environmental monitoring and assessment* 187 (1), p. 4209. DOI: 10.1007/s10661-014-4209-4.

IUSS Working Group WRB (2015): World Reference Base for Soil Resources 2014, update 2015 International soil classification system for naming soils and creating legends for soil maps. World Soil Resources Reports No. 106. FAO, Rome.

Jacobs, P. M.; Mason, J. A.; Hanson, P. R. (2012): Loess mantle spatial variability and soil horizonation, southern Wisconsin, USA. In *Quaternary International* 265, pp. 43–53. DOI: 10.1016/j.quaint.2012.01.017.

Jamagne, M. (1973): Contribution à l'étude pédogénétique des formations loessiques du Nord de la France. In *Thèse de la Faculté des sciences agronomique de Gembloux*.

Jary, Z. (Ed.) (1999): Charakterystyka podstawowych horyzontów litologiczno-strukturalnych lessach południowo-zachodniej Polski. In Jary Z. (Ed.), III Seminarium Lessowe – Geneza i wiek pokrywowych utorów pylastych południowo-zachodniej Polski. Uniwersytet Wrocławski, Wrocław-Bożków Poland.

Jary, Z.; Kida, J. (2000): Loess particles sources, transport and deposition on the example of SW Poland. In *Acta Universitatis Wratislaviensis 2269, Studia Geograficzne* (74), pp. 71–77.

Jary, Z., Ciszek, D. (2013): Late Pleistocene loess–palaeosol sequences in Poland and western Ukraine. In *Quaternary International 296*, pp. 37–50.

Kabała, C. (ed); Bekier, J.; Bogacz, A.; Binczychi, T. (2015): Gleby Dolnego Śląska-Soils of Lower Silesia. Geneza, różnorodność i ochrona : praca zbiorowa - origins, diversity and protections. Wrocław: Polskie Towarzystwo Gleboznawcze.

Kalm, V. E.; Rutter, N. W.; Rokosh, C. D. (1996): Clay minerals and their paleoenvironmental interpretation in the Baoji loess section, Southern Loess Plateau, China. In *CATENA* (27), pp. 49–61.

Keilhack, K. (1899): Die Stillstandslagen des letzten Inlandeises und die hydrographische Entwicklung des pommerschen Küstengebietes. In *Jahrbuch der Preussischen Geologischen Landesanstalt* (19), pp. 90–152.

Kierczak, J.; Pędziwiatr, A.; Waroszewski, J.; Modelska, M. (2016): Mobility of Ni, Cr and Co in serpentine soils derived on various ultrabasic bedrocks under temperate climate. In *Geoderma* 268, pp. 78–91. DOI: 10.1016/j.geoderma.2016.01.025.

Kosmala, G. (2015): Geographical characteristics of Silesia. In *Academy of Physical Education in Katowice*.

Kozarski, S. (1981): Vistulian stratigraphy and chronology of the Great Poland Lowland. In *Geografia* (6), pp. 1–44.

Kozarski, S. (1988.): Origin of pradolinas: a discussion of mistaken ideas. In *Zeitschrift für Gletscherkunde und Glazialgeologie* (24 (1)), pp. 75–92.

Kramarska, R. (1998): Origin and development of the Odra Bank in the light of the geologic structure and radiocarbon dating. In *Geological Quarterly* (42 (3)), pp. 277–288.

Kryza, R.; Pin, C. (2010): The Central-Sudetic ophiolites (SW Poland). Petrogenetic issues, geochronology and palaeotectonic implications. In *Gondwana Research* 17 (2-3), pp. 292–305. DOI: 10.1016/j.gr.2009.11.001.

Kunze, G. W.; Dixon, J. B. (1986): Pretreatment for mineralogical analysis. In A. Klute (ed), Methods of Soil Analysis, Part 1, Physical and Mineralogical Methods, Agronomy Monograph no. 9, 2nd edn. Madison, WI, American Soil Association and Soil Science Society of America.

Lång, L. (2000): Heavy mineral weathering under acidic soil conditions. In *Applied Geochemistry* 15 (4), pp. 415–423. DOI: 10.1016/S0883-2927(99)00064-5.

Leonhard, K. C. von (1823): Charakteristik der Falsarten: Engelman, Heidelberg, 3 vols.

Marcinkowski, B.; Mycielska-Dowgiałło, E. (2013): Heavy-mineral analysis in Polish investigations of Quaternary deposits. A review. In *Geologos* 19 (1-2). DOI: 10.2478/logos-2013-0002.

Marks, L. (2002): Last Glacial Maximum in Poland. In *Quaternary Science Reviews* 21 (1-3), pp. 103–110. DOI: 10.1016/S0277-3791(01)00086-5.

Moore, D. M.; Reynolds, R. C. (1997): X-ray diffraction and the identification and analysis of clay minerals. 2. ed. Oxford: Oxford Univ. Press.

Mosser-Ruck, R.; Devineau, K.; Charpentier, D.; Cathelineau, M. (2005): Effects of ethylene glycol saturation protocols on XRD patterns. A critical review and discussion. In *Clays Clay Miner.* 53 (6), pp. 631–638. DOI: 10.1346/CCMN.2005.0530609.

Muhs, D. R. (2013): The geologic records of dust in the Quaternary. In *Aeolian Research* 9, pp. 3–48. DOI: 10.1016/j.aeolia.2012.08.001.

Muhs, D.R., Bettis III, E.A. (2003): Quaternary loess-Paleosol sequences as examples of climate-driven sedimentary extremes. In *The Geological Society of America Special Papers* (370), 53-74.

Nesbitt, H. W.; Young, G. M. (1989): Formation and Diagenesis of Weathering Profiles. In *The Journal of Geology* 97 (2), pp. 129–147. DOI: 10.1086/629290.

Okrusch, M.; Matthes, S. (2014): Mineralogie. Eine Einführung in die spezielle Mineralogie, Petrologie und Lagerstättenkunde. 9. Aufl. Berlin: Springer Spektrum (Springer-Lehrbuch). Available online at http://dx.doi.org/10.1007/978-3-642-34660-6.

Pécsi, M.; Richter, G. (1996): Löß. Herkunft - Gliederung - Landschaften ; gewidmet dem 14. INQUA-Kongreß in Berlin. Berlin: Borntraeger (Zeitschrift für Geomorphologie Supplementband, 98).

Poormasoomi, M.; Ramezanpour, H. (2010): A study on mineralogy of soils under two parent rocks in higher rainfall areas of Iran. In *Conference Paper: 19th World Congress of Soil Science 2010*, pp. 1–6.

Pope, G. A.; Meierding, Th.C.; Paradise, Th.R. (2002): Geomorphology's role in the study of weathering of cultural stone. In *Geomorphology* 47 (2-4), pp. 211–225. DOI: 10.1016/S0169-555X(02)00098-3.

Profe, Jörn; Wacha, Lara; Frechen, Manfred; Ohlendorf, Christian; Zolitschka, Bernd (2018): XRF scanning of discrete samples – A chemostratigraphic approach exemplified for loess-paleosol sequences from the Island of Susak, Croatia. In *Quaternary International. DOI:* 10.1016/j.quaint.2018.05.006.

Pye, K. (1995): The natur, origin and accumulation of Loess. In *Quaternary Science Reviews* 14, pp. 653–667.

Raczyk, Jerzy; Jary, Zdzisław; Korabiewski, Bartosz (2015): Geochemical properties of the Late Pleistocene loess-soil sequence in Dankowice (Niemcza-Strzelin Hills). In *Landform Analysis* 29, pp. 49–61. DOI: 10.12657/landfana.029.007.

Rdzany, Zbigniew (2009): Reconstruction of the course of the Warta Glaciation in the Łódź Region. Łódź: University of Łódź.

Reed, S.J.B. (2010): Electron microprobe analysis and scanning electron microscopy in geology. In *University of Cambridge, Cambridge University Press*.

Sauer, D.; Kadereit, A.; Kühn, P.; Kösel, M.; Miller, Ch.E.; Shinonaga, T. et al. (2016): The loess-palaeosol sequence of Datthausen, SW Germany. Characteristics, chronology, and implications for the use of the Lohne Soil as a marker soil. In *CATENA* 146, pp. 10–29. DOI: 10.1016/j.catena.2016.06.024.

Schaetzl, R. J.; Anderson, S. (2005): Soils. Genesis and geomorphology. Cambridge: Cambridge Univ. Press.

Schatz, A.; Scholten, Th.; Kühn, P. (2015): Paleoclimate and weathering of the Tokaj (Hungary) loess–paleosol sequence. In *Palaeogeography, Palaeoclimatology, Palaeoecology* 426, pp. 170–182. DOI: 10.1016/j.palaeo.2015.03.016.

Scheffer, F.; Schachtschabel, P.; Blume, H.; Brümmer, G. W.; Horn, R.; Kandeler, E. et al. (2010): Lehrbuch der Bodenkunde. 16. Auflage. Heidelberg: Spektrum Akademischer Verlag. Available online at http://site.ebrary.com/lib/alltitles/docDetail.action?docID=10359930.

Scheib, A. J.; Birke, M.; Dinelli, E. (2014): Geochemical evidence of aeolian deposits in European soils. In *Boreas* 43 (1), pp. 175–192. DOI: 10.1111/bor.12029.

Schnetger, B. (1992): Chemical composition of loess from a local and worldwide view. In *Neues Jahrbuch für Mineralogie Monatshefte* (1), pp. 29–47.

Silva-Sánchez, N.; Schofield, E. J.; Mighall, T. M.; Martínez Cortizas, A.; Edwards, K. J.; Foster, I. (2015): Climate changes, lead pollution and soil erosion in south Greenland over the past 700 years. In *Quat. res.* 84 (02), pp. 159–173. DOI: 10.1016/j.yqres.2015.06.001.

Smalley, I. J.; Leach, J. A. (1978): The origin and distribution of the loess in the Danube basin and associated regions of East-Central Europe: a review. In *Sedimentary Geology* (21), pp. 1–26.

Smalley, I. J.; Vita-Finzi, C. (1968): The formation of fine particles in sandy deserts and the nature of "desert' loess. In *Journal of Sedimentary Petrology* (38), pp. 766–774.

Sprafke, T.; Obreht, I. (2016): Loess. Rock, sediment or soil – What is missing for its definition? In *Quaternary International* 399, pp. 198–207. DOI: 10.1016/j.quaint.2015.03.033.

Strawn, D. G.; Bohn, H. L.; O'Connor, G. A. (2015): Soil chemistry. 4. ed. Chichester, West Sussex: Wiley Blackwell.

Újvári, G.; Varga, A.; Balogh-Brunstad, Z. (2008): Origin, weathering, and geochemical composition of loess in southwestern Hungary. In *Quat. res.* 69 (03), pp. 421–437. DOI: 10.1016/j.yqres.2008.02.001.

Velde, B.; Meunier, A. (2008): The Origin of Clay Minerals in Soils and Weathered Rocks. Berlin, Heidelberg: Springer-Verlag Berlin Heidelberg. Available online at http://dx.doi.org/10.1007/978-3-540-75634-7.

Velde, Bruce (1995): Origin and Mineralogy of Clays. Berlin, Heidelberg: Springer Berlin Heidelberg.

Walker, G. F. (1958): Reactions of expanding lattice clay minerals with glycerol and ethylene glycol. In *Clay Minerals Bulletin* (3), pp. 302–313.

Waroszewski, J.; Egli, M.; Kabala, C.; Kierczak, J.; Brandova, D. (2016): Mass fluxes and clay mineral formation in soils developed on slope deposits of the Kowarski Grzbiet (Karkonosze Mountains, Czech Republic/Poland). In *Geoderma* 264, pp. 363–378. DOI: 10.1016/j.geoderma.2015.08.044.

Waroszewski, J.; Sprafke, T.; Kabala, C.; Musztyfaga, E.; Łabaz, B.; Woźniczka, P. (2017): Aeolian silt contribution to soils on mountain slopes (Mt. Ślęża, southwest Poland). In *Quat. res.* 76, pp. 1–16. DOI: 10.1017/qua.2017.76.

Whittig, L. D.; Allardice, W. R. (1986): X-ray diffraction techniques. In A. Klute (ed.) Methods of Soil Analysis, Part 1. Physical and Mineralogical Methods, Agronomy Monograph no. 9, 2nd edn. American Soil Association and Soil Science Society of America, Madison, WI.

Wilson, M. J. (1999): The origin and formation of clay minerals in soils: past, present and future perspectives. In *Clay Minerals* (34), pp. 7–25.

Woldstedt, P. (1931): Über Randlagen der letzten Vereisung in Ostdeutschland und Polen und über die Herausbildung des Netze-Warthe Urstromtales. In *Jahrbuch der Preussischen Geologischen Landesanstalt* (52), pp. 59–67.

## 10.2 Internet

Britannica 2018a: Esker. Online available. URL:  https://www.britannica.com/science/esker (Last access: 11.7.18)

Britannica 2018b: Kame. Online available. URL:  https://www.britannica.com/science/kame (Last access: 11.7.18)

Britannica 2018c: Classification of Sandstones. Online available. URL: https://www.britannica.com/science/sedimentary-rock/Classification-of-sandstones (Last access: 22.8.18)

Illinois Institute of technology 2018: Miller Indices. Online available. URL: https://web.iit.edu/sites/web/files/departments/academic-affairs/academic-resource-center/pdfs/Miller_Indices.pdf (Last access: 26.3.18)

Nationsonline 2018:  Administrativ Map of Poland. Online available. URL: http://www.nationsonline.org/oneworld/map/poland-administrative-map.htm (Last access: 26.7.2018)

Smith College 2018: Lecture notes – Mineralogy – Miller Indices. Online available. URL: http://www.science.smith.edu/geosciences/min_jb/Miller_Indices.pdf (Last access: 26.3.18)

Webmineral 2018: Minerals by Element Search. Online available. URL: http://webmineral.com/MySQL/mineral_chem.php (Last access: 5.6.18)

10.3 Images

**Fig. 1:**

Okrusch, Martin; Matthes, Siegfried (2014): Mineralogie. Eine Einführung in die spezielle Mineralogie, Petrologie und Lagerstättenkunde. 9. Aufl. Berlin: Springer Spektrum (Springer-Lehrbuch): 8.

Chen B., Evans J.R.G., Greenwell H.C., Boulet P., Conveney P.V., Bowden A. and Whiting A. (2008): A critical appraisal of polymer-clay nanocomposites. In Chemical Society Reviews 37: 572.

**Fig. 2:**

Muhs, D. R. (2013): The geologic records of dust in the Quaternary. In Aeolian Research 9: 15.

**Fig. 3:**

Karnet 2018: Topography Silesia. Online available. URL:

http://karnet.up.wroc.pl/~kabala/Silesia_Sudetes_morphology.jpg (Last access: 11.7.18)

Mapsland 2018: Elevation map of Poland. Online available. URL:
https://www.mapsland.com/maps/europe/poland/elevation-map-of-poland-small.jpg (Last access: 11.7.18)

**Fig. 4 & 5:**

Kabała, C. (ed); Bekier, J.; Bogacz, A.; Binczychi, T. (2015): Gleby Dolnego Śląska-Soils of Lower Silesia. Geneza, różnorodność i ochrona: praca zbiorowa - origins, diversity and protections. Wrocław: Polskie Towarzystwo Gleboznawcze: 11 & 18.

**Fig. 6:**

Mapy geoportal 2018: Geoportal. Online available. URL:
http://mapy.geoportal.gov.pl/imap/?gpmap=gp1 (Last access: 26.7.2018)

**Fig. 7 - 9:** J. Waroszewski 2017

**Fig. 10 & 11:** M. Vögtli 2017/2018

**Fig. 16:** J. Kierczak 2018

## Appendix

| Sample Nr. | Laboratory Nr. | Profile | Horizon | Depth (cm) | Corg. (%) | pH H2O | Particle size distribution [%] | | | Texture classes USDA |
| --- | --- | --- | --- | --- | --- | --- | --- | --- | --- | --- |
| | | | | | | | <0,002 mm | 0,05-0,002 mm | 2-0,05 mm | |
| 1 | 165C17MV1 | LS1 | AE | 18-45 | 1.22 | 6.30 | 19 | 65 | 16 | SiL |
| 2 | 165C17MV2 | LS1 | 2Btg2/E | 78-95 | 1.18 | 7.15 | 24 | 56 | 20 | SiL |
| 3 | 165C17MV3 | LS1 | 3BC | 95-112 | 0.13 | 6.01 | 19 | 19 | 62 | SL |
| 4 | 165C17MV4 | LS2 | E | 14-19 | 0.63 | 4.80 | 11 | 67 | 22 | SiL |
| 5 | 165C17MV5 | LS2 | 2Bt1 | 33-45 | 0.38 | 5.96 | 28 | 54 | 18 | SiCL |
| 6 | 165C17MV6 | LS2 | 3BC | 68-86 | 0.24 | 6.43 | 29 | 40 | 31 | CL |
| 7 | 165C17MV7 | LS3 | Bw(t) | 8-30 | 1.19 | 4.49 | 12 | 69 | 19 | SiL |
| 8 | 165C17MV8 | LS3 | 2BC | 50-70 | 0.34 | 4.53 | 12 | 62 | 26 | SiL |
| 9 | 165C17MV9 | LS3 | 3BC | 70-110 | 0.31 | 4.28 | 8 | 17 | 75 | SL |
| 10 | 165C17MV10 | LS4 | AE | 0-20 | 1.019 | 5.30 | 8 | 68 | 24 | SiL |
| 11 | 165C17MV11 | LS4 | 2Btg1 | 36-64 | 0.182 | 5.32 | 26 | 34 | 40 | L |
| 12 | 165C17MV12 | LS4 | 2BC | 81-105 | 0.095 | 5.20 | 25 | 24 | 51 | SCL |
| 13 | 165C17MV13 | LS5 | AEg | 4-14 | 2.562 | 3.76 | 8 | 71 | 21 | SiL |
| 14 | 165C17MV14 | LS5 | Btg1 | 40-50 | 0.292 | 4.58 | 24 | 56 | 20 | SiL |
| 15 | 165C17MV15 | LS5 | 2CBtg | 70-100 | 0.166 | 5.42 | 30 | 38 | 32 | CL |

Tab. A1: Additional information for each sample.

| Profile | Horizon | SiO2 | Al2O3 | Fe2O3 | MgO | CaO | Na2O | K2O | TiO2 | P2O5 | MnO | Cr2O3 | Ni | Sc | LOI | Sum |
|---------|---------|------|-------|-------|-----|-----|------|-----|------|------|-----|-------|-----|-----|-----|------|
| LS1 | Ap | 76.62 | 8.66 | 2.62 | 0.62 | 0.65 | 0.82 | 2.49 | 0.73 | 0.18 | 0.08 | 0.009 | 24 | 7 | 6.3 | 99.87 |
| LS1 | AE | 77.46 | 8.74 | 2.63 | 0.61 | 0.59 | 0.84 | 2.49 | 0.74 | 0.16 | 0.09 | 0.009 | 26 | 7 | 5.5 | 99.88 |
| LS1 | 2Btg1/E | 74.70 | 10.52 | 3.68 | 0.87 | 0.68 | 0.78 | 2.56 | 0.77 | 0.09 | 0.05 | 0.011 | 24 | 9 | 5.1 | 99.87 |
| LS1 | 2Btg2/E | 74.38 | 10.71 | 3.90 | 0.93 | 0.62 | 0.87 | 2.69 | 0.73 | 0.10 | 0.04 | 0.011 | 24 | 9 | 4.8 | 99.87 |
| LS1 | 3BC | 70.68 | 13.66 | 3.48 | 1.05 | 0.35 | 1.57 | 4.17 | 0.39 | 0.06 | 0.04 | 0.005 | 32 | 8 | 4.4 | 99.91 |
| LS2 | AE | 79.70 | 6.36 | 2.24 | 1.50 | 0.43 | 0.90 | 1.99 | 0.72 | 0.04 | 0.03 | 0.040 | 98 | 5 | 5.9 | 99.83 |
| LS2 | E | 80.35 | 7.12 | 2.80 | 1.55 | 0.42 | 0.87 | 2.12 | 0.76 | 0.04 | 0.05 | 0.048 | 128 | 6 | 3.7 | 99.82 |
| LS2 | EB | 75.57 | 9.68 | 3.97 | 1.35 | 0.34 | 0.78 | 2.36 | 0.73 | 0.06 | 0.05 | 0.036 | 125 | 9 | 4.9 | 99.83 |
| LS2 | 2Bt1 | 72.60 | 10.28 | 5.17 | 2.26 | 0.33 | 0.81 | 2.22 | 0.73 | 0.06 | 0.07 | 0.065 | 225 | 10 | 5.2 | 99.81 |
| LS2 | 2Bt2 | 71.88 | 9.97 | 5.29 | 3.17 | 0.38 | 0.82 | 2.10 | 0.69 | 0.04 | 0.09 | 0.076 | 317 | 11 | 5.3 | 99.81 |
| LS2 | 3BC | 67.09 | 9.16 | 6.67 | 6.23 | 0.34 | 0.61 | 1.64 | 0.57 | 0.02 | 0.10 | 0.155 | 810 | 13 | 7.1 | 99.77 |
| LS3 | ABw | 79.19 | 6.38 | 1.66 | 0.25 | 0.29 | 0.81 | 1.96 | 0.68 | 0.05 | 0.02 | 0.008 | <20 | 4 | 8.6 | 99.87 |
| LS3 | Bw1 (t) | 82.36 | 7.24 | 1.80 | 0.31 | 0.31 | 0.87 | 2.09 | 0.70 | 0.03 | 0.04 | 0.009 | <20 | 5 | 4.1 | 99.86 |
| LS3 | 2Bt | 82.74 | 7.64 | 1.90 | 0.36 | 0.32 | 0.93 | 2.27 | 0.70 | 0.03 | 0.03 | 0.008 | <20 | 5 | 2.9 | 99.86 |
| LS3 | 2BC | 82.04 | 8.10 | 1.99 | 0.42 | 0.32 | 1.09 | 2.46 | 0.67 | 0.02 | 0.03 | 0.009 | <20 | 21 | 2.7 | 99.86 |
| LS3 | 3BC | 71.17 | 14.95 | 2.22 | 0.42 | 0.09 | 3.66 | 3.68 | 0.47 | 0.03 | 0.02 | 0.004 | <20 | 6 | 3.2 | 99.90 |
| LS3 | 3CR | 65.28 | 18.54 | 2.70 | 0.51 | 0.05 | 3.90 | 4.54 | 0.50 | 0.03 | 0.01 | 0.002 | <20 | 8 | 3.8 | 99.89 |
| LS4 | AE | 79.24 | 8.21 | 2.38 | 0.50 | 0.53 | 0.92 | 2.32 | 0.72 | 0.08 | 0.11 | 0.010 | <20 | 7 | 4.8 | 99.84 |
| LS4 | EB | 78.29 | 9.27 | 3.21 | 0.64 | 0.52 | 0.84 | 2.25 | 0.67 | 0.05 | 0.05 | 0.012 | 24 | 8 | 4.1 | 99.85 |
| LS4 | 2Btg1 | 58.71 | 17.10 | 7.88 | 2.03 | 2.03 | 0.66 | 1.29 | 0.70 | 0.03 | 0.05 | 0.041 | 120 | 35 | 9.3 | 99.87 |
| LS4 | 2Btg2 | 69.96 | 13.10 | 5.02 | 0.89 | 1.01 | 1.15 | 1.85 | 0.64 | 0.03 | 0.06 | 0.017 | 48 | 21 | 6.2 | 99.91 |
| LS4 | 2BC | 57.78 | 18.62 | 7.49 | 1.18 | 1.58 | 1.39 | 2.04 | 1.14 | 0.03 | 0.12 | 0.034 | 69 | 33 | 8.5 | 99.88 |
| LS4 | 2BC (wedges) | 50.78 | 21.14 | 8.86 | 2.29 | 2.68 | 0.75 | 0.98 | 0.79 | 0.01 | 0.13 | 0.069 | 115 | 49 | 11.4 | 99.86 |
| LS5 | Eg | 83.06 | 7.23 | 1.82 | 0.38 | 0.44 | 0.9 | 2.16 | 0.8 | 0.07 | 0.02 | 0.01 | <20 | 5 | 3.0 | 99.91 |
| LS5 | Eg/Btg | 75.96 | 9.76 | 4.11 | 0.74 | 0.53 | 0.87 | 2.16 | 0.8 | 0.04 | 0.04 | 0.014 | 22 | 9 | 4.8 | 99.91 |
| LS5 | Btg1 | 74.71 | 10.48 | 3.78 | 0.86 | 0.58 | 0.85 | 2.27 | 0.82 | 0.05 | 0.03 | 0.015 | 28 | 11 | 5.4 | 99.89 |
| LS5 | 2CBtg | 64.74 | 12.93 | 7.38 | 1.34 | 0.91 | 0.74 | 1.8 | 1.35 | 0.13 | 0.14 | 0.034 | 84 | 16 | 8.3 | 99.85 |

Tab. B1: Additional geochemical information of each horizon.

| Profile | Horizon | Ba | Be | Co | Cs | Ga | Hf | Nb | Rb | Sn | Sr | Ta | Th | U | V | W | Zr |
|---|---|---|---|---|---|---|---|---|---|---|---|---|---|---|---|---|---|
| LS1 | Ap | 447 | 5 | 7.5 | 2.6 | 7.5 | 14.3 | 13.6 | 84.4 | 2 | 91.1 | 1.3 | 9.8 | 2.5 | 59 | 1.7 | 533.2 |
| LS1 | AE | 436 | 5 | 8.7 | 3.2 | 7.1 | 15.1 | 14.4 | 84.6 | 3 | 85.7 | 1.9 | 9.6 | 2.6 | 54 | 2.4 | 558.7 |
| LS1 | 2Btg1/E | 464 | 7 | 6.8 | 4.2 | 10.2 | 12.4 | 16.4 | 97.3 | 3 | 85.1 | 1.0 | 10.6 | 2.5 | 69 | 2.0 | 517.7 |
| LS1 | 2Btg2/E | 435 | <1 | 7.8 | 6.3 | 10.8 | 10.7 | 14.6 | 101.1 | 2 | 87.4 | 1.3 | 10.5 | 2.6 | 68 | 1.8 | 407.1 |
| LS1 | 3BC | 445 | <1 | 9.0 | 35.1 | 14.3 | 5.4 | 8.1 | 167.8 | 3 | 77.3 | 0.8 | 10.8 | 1.2 | 56 | 0.7 | 186.5 |
| LS2 | AE | 365 | <1 | 8.9 | 1.3 | 5.8 | 15.6 | 12.5 | 56.7 | 2 | 76.8 | 0.8 | 9.3 | 2.8 | 42 | 1.3 | 605.3 |
| LS2 | E | 393 | 1 | 15.5 | 1.6 | 6.2 | 17.6 | 14.5 | 62.0 | 2 | 79.0 | 1.0 | 10.4 | 3.4 | 47 | 1.3 | 656.2 |
| LS2 | EB | 438 | <1 | 15.8 | 3.0 | 9.9 | 13.3 | 13.4 | 80.3 | 2 | 76.9 | 1.2 | 10.9 | 2.8 | 67 | 1.1 | 491.3 |
| LS2 | 2Bt1 | 392 | <1 | 22.5 | 3.7 | 10.4 | 12.8 | 12.6 | 82.9 | 2 | 74.7 | 0.8 | 12.0 | 3.0 | 76 | 2.9 | 487.6 |
| LS2 | 2Bt2 | 373 | 2 | 24.3 | 3.5 | 9.6 | 11.1 | 11.6 | 78.3 | 2 | 70.4 | 1.0 | 11.2 | 2.9 | 73 | 1.9 | 421.0 |
| LS2 | 3BC | 328 | 2 | 47.2 | 3.5 | 9.2 | 7.6 | 10.5 | 70.2 | 2 | 59.5 | 0.9 | 8.5 | 2.2 | 74 | 2.6 | 292.6 |
| LS3 | ABw | 366 | <1 | 2.1 | 1.8 | 8.2 | 13.5 | 15.0 | 59.2 | 2 | 64.9 | 0.9 | 6.5 | 2.5 | 35 | 1.2 | 504.0 |
| LS3 | Bw1 (t) | 400 | <1 | 3.0 | 1.4 | 6.0 | 13.5 | 13.3 | 58.4 | 2 | 69.9 | 1.1 | 7.0 | 2.4 | 38 | 1.2 | 521.7 |
| LS3 | 2Bt | 435 | <1 | 3.4 | 1.7 | 7.8 | 13.4 | 13.6 | 67.0 | 2 | 72.4 | 1.0 | 8.0 | 2.7 | 38 | 1.6 | 509.5 |
| LS3 | 2BC | 414 | <1 | 4.0 | 1.9 | 8.5 | 13.2 | 14.1 | 74.2 | 2 | 74.5 | 1.0 | 7.6 | 2.3 | 37 | 1.4 | 509.9 |
| LS3 | 3BC | 427 | 2 | 4.1 | 1.5 | 16.0 | 5.7 | 19.2 | 107.1 | 4 | 63.0 | 2.2 | 7.9 | 2.8 | 33 | 1.3 | 200.4 |
| LS3 | 3CR | 419 | <1 | 5.6 | 1.1 | 23.7 | 5.2 | 26.2 | 158.0 | 6 | 53.2 | 3.1 | 16.5 | 3.5 | 35 | 1.1 | 152.8 |
| LS4 | AE | 459 | 1 | 8.0 | 1.9 | 7.6 | 13.6 | 13.0 | 73.2 | 2 | 83.1 | 1.0 | 8.9 | 2.8 | 47 | 1.1 | 493.8 |
| LS4 | EB | 439 | 1 | 7.7 | 2.7 | 9.0 | 11.8 | 12.6 | 75.7 | 2 | 79.8 | 0.7 | 8.3 | 2.6 | 55 | 1.5 | 457.0 |
| LS4 | 2Btg1 | 361 | 2 | 22.4 | 1.6 | 15.1 | 3.3 | 4.4 | 43.8 | <1 | 56.6 | 0.5 | 5.7 | 2.8 | 98 | 1.1 | 118.7 |
| LS4 | 2Btg2 | 311 | 3 | 23.3 | 1.7 | 12.2 | 2.6 | 5.6 | 61.7 | 1 | 61.2 | 0.6 | 9.4 | 2.5 | 67 | 2.4 | 84.8 |
| LS4 | 2BC | 431 | 6 | 68.3 | 1.3 | 16.8 | 2.0 | 5.3 | 61.6 | 1 | 80.3 | 0.6 | 5.5 | 4.2 | 102 | 4.8 | 50.6 |
| LS4 | 2BC (wedges) | 423 | 1 | 90.0 | 0.9 | 17.2 | 1.3 | 3.1 | 30.7 | <1 | 64.5 | 0.2 | 3.0 | 5.0 | 89 | 4.4 | 39.9 |
| LS5 | Eg | 425 | <1 | 3.0 | 1.8 | 6.9 | 13.0 | 15.1 | 89.1 | 2 | 83.2 | 1.1 | 7.5 | 2.1 | 52 | 1.7 | 481.5 |
| LS5 | Eg/Btg | 403 | <1 | 11.6 | 2.8 | 9.1 | 10.0 | 14.4 | 86.3 | 2 | 87.1 | 1.1 | 9.2 | 2.4 | 76 | 1.2 | 381.7 |
| LS5 | Btg1 | 446 | 1 | 14.0 | 3.1 | 10.4 | 12.0 | 15.4 | 76.9 | 2 | 93.8 | 1.0 | 10.0 | 2.5 | 75 | 1.1 | 432.2 |
| LS5 | 2CBtg | 442 | 2 | 29.3 | 3.8 | 14.3 | 10.6 | 27.8 | 74.9 | 3 | 115.2 | 1.6 | 9.9 | 2.9 | 141 | 1.6 | 403.5 |

Tab. C1: Measured Elements of each horizon.

| Profile | Horizon | Y | La | Ce | Pr | Nd | Sm | Eu | Gd | Tb | Dy | Ho | Er | Tm | Yb |
|---------|---------|------|------|------|------|------|------|------|------|------|------|------|------|------|------|
| LS1 | Ap | 26.4 | 29.7 | 66.6 | 7.07 | 27.0 | 4.68 | 0.81 | 4.35 | 0.70 | 4.15 | 0.86 | 2.55 | 0.45 | 3.01 |
| LS1 | AE | 26.7 | 29.1 | 68.1 | 6.85 | 25.4 | 4.61 | 0.90 | 4.17 | 0.64 | 4.42 | 0.94 | 2.93 | 0.41 | 3.19 |
| LS1 | 2Btg1/E | 28.2 | 32.4 | 73.3 | 7.21 | 28.0 | 4.72 | 0.95 | 4.69 | 0.71 | 4.11 | 0.83 | 2.84 | 0.45 | 2.77 |
| LS1 | 2Btg2/E | 25.3 | 31.0 | 64.9 | 7.45 | 26.9 | 5.10 | 0.91 | 4.55 | 0.71 | 4.69 | 0.93 | 2.87 | 0.37 | 2.98 |
| LS1 | 3BC | 24.0 | 27.2 | 55.3 | 6.14 | 23.3 | 3.80 | 0.78 | 3.96 | 0.59 | 3.73 | 0.83 | 2.69 | 0.35 | 2.39 |
| LS2 | AE | 22.3 | 26.6 | 54.3 | 6.08 | 22.0 | 4.28 | 0.65 | 3.61 | 0.61 | 3.75 | 0.83 | 2.53 | 0.42 | 2.76 |
| LS2 | E | 24.9 | 29.7 | 64.9 | 6.88 | 25.8 | 4.83 | 0.66 | 4.37 | 0.74 | 4.54 | 0.98 | 3.15 | 0.48 | 3.30 |
| LS2 | EB | 27.2 | 29.7 | 69.8 | 6.92 | 25.4 | 4.48 | 0.78 | 4.56 | 0.74 | 4.18 | 1.01 | 3.08 | 0.47 | 3.31 |
| LS2 | 2Bt1 | 26.8 | 33.8 | 77.7 | 8.15 | 30.7 | 5.48 | 0.99 | 5.17 | 0.84 | 4.78 | 1.04 | 3.27 | 0.49 | 3.25 |
| LS2 | 2Bt2 | 27.7 | 31.8 | 76.9 | 8.44 | 31.2 | 6.30 | 1.17 | 5.78 | 0.90 | 5.45 | 1.11 | 3.23 | 0.51 | 3.35 |
| LS2 | 3BC | 27.1 | 29.7 | 59.1 | 7.05 | 27.1 | 5.44 | 1.01 | 5.22 | 0.83 | 4.85 | 1.05 | 3.15 | 0.49 | 3.01 |
| LS3 | ABw | 21.5 | 21.7 | 42.2 | 4.85 | 17.7 | 3.29 | 0.56 | 3.30 | 0.55 | 3.57 | 0.84 | 2.88 | 0.43 | 2.62 |
| LS3 | Bw1 (t) | 20.4 | 21.5 | 45.4 | 4.79 | 16.9 | 3.41 | 0.57 | 3.13 | 0.53 | 3.40 | 0.77 | 2.42 | 0.39 | 2.70 |
| LS3 | 2Bt | 20.8 | 23.6 | 48.0 | 5.35 | 19.4 | 3.51 | 0.57 | 3.41 | 0.56 | 3.59 | 0.79 | 2.58 | 0.39 | 2.80 |
| LS3 | 2BC | 21.1 | 23.4 | 50.0 | 5.11 | 18.0 | 3.65 | 0.54 | 3.30 | 0.56 | 3.34 | 0.78 | 2.56 | 0.41 | 2.72 |
| LS3 | 3BC | 24.1 | 22.7 | 48.4 | 4.81 | 16.9 | 3.50 | 0.52 | 3.68 | 0.60 | 3.73 | 0.94 | 2.72 | 0.40 | 2.57 |
| LS3 | 3CR | 32.8 | 34.3 | 70.3 | 6.91 | 24.4 | 5.29 | 0.79 | 5.16 | 0.90 | 5.45 | 1.21 | 3.76 | 0.53 | 3.59 |
| LS4 | AE | 23.3 | 26.6 | 55.6 | 5.78 | 21.4 | 4.00 | 0.65 | 3.82 | 0.63 | 3.87 | 0.90 | 2.75 | 0.42 | 2.87 |
| LS4 | EB | 20.4 | 24.0 | 56.2 | 5.32 | 18.7 | 3.50 | 0.57 | 3.41 | 0.57 | 3.52 | 0.77 | 2.31 | 0.37 | 2.46 |
| LS4 | 2Btg1 | 14.1 | 15.9 | 32.2 | 3.60 | 13.5 | 2.90 | 0.52 | 2.84 | 0.45 | 2.57 | 0.54 | 1.57 | 0.23 | 1.56 |
| LS4 | 2Btg2 | 14.9 | 14.3 | 30.5 | 3.44 | 13.4 | 2.88 | 0.51 | 2.76 | 0.49 | 2.69 | 0.55 | 1.68 | 0.27 | 1.63 |
| LS4 | 2BC | 17.4 | 11.8 | 24.4 | 3.05 | 11.9 | 2.95 | 0.62 | 2.92 | 0.51 | 3.17 | 0.67 | 2.05 | 0.31 | 2.08 |
| LS4 | 2BC (wedges) | 17.5 | 10.8 | 24.1 | 2.81 | 11.2 | 2.64 | 0.74 | 2.99 | 0.51 | 3.08 | 0.67 | 2.09 | 0.28 | 1.85 |
| LS5 | Eg | 21.2 | 22.8 | 45.5 | 5.15 | 18.9 | 3.46 | 0.65 | 3.41 | 0.57 | 3.62 | 0.78 | 2.44 | 0.38 | 2.48 |
| LS5 | Eg/Btg | 19.5 | 23.3 | 51.6 | 5.58 | 21.2 | 3.65 | 0.72 | 3.45 | 0.56 | 3.59 | 0.75 | 2.19 | 0.34 | 2.27 |
| LS5 | Btg1 | 24.2 | 29.6 | 60.1 | 6.66 | 25.9 | 4.39 | 0.92 | 4.36 | 0.68 | 4.41 | 0.87 | 2.73 | 0.43 | 2.67 |
| LS5 | 2CBtg | 33.8 | 39.3 | 79.5 | 9.13 | 35.5 | 6.82 | 1.58 | 6.89 | 1.00 | 6.18 | 1.29 | 3.54 | 0.54 | 3.28 |

Tab. C2: Measured Elements of each horizon.

75

| Profile | Horizon | Lu | TOT/C | TOT/S | Mo | Cu | Pb | Zn | Ni | As | Cd | Sb | Ag | Au | Hg | Tl | Se |
|---|---|---|---|---|---|---|---|---|---|---|---|---|---|---|---|---|---|
| LS1 | Ap | 0.44 | 1.56 | 0.02 | 0.3 | 12.8 | 19.6 | 41 | 14.4 | 7.7 | 0.2 | 0.3 | <0.1 | <0.5 | 0.06 | 0.1 | <0.5 |
| LS1 | AE | 0.48 | 1.28 | <0.02 | 0.3 | 10.6 | 19.9 | 40 | 14.0 | 7.9 | 0.3 | 0.2 | <0.1 | <0.5 | 0.06 | 0.1 | <0.5 |
| LS1 | 2Btg1/E | 0.50 | 0.26 | <0.02 | 0.3 | 12.7 | 13.6 | 39 | 19.2 | 7.6 | 0.1 | 0.1 | <0.1 | 1.0 | 0.02 | 0.2 | <0.5 |
| LS1 | 2Btg2/E | 0.43 | 0.15 | <0.02 | 0.3 | 13.4 | 13.7 | 39 | 24.7 | 8.5 | <0.1 | 0.2 | <0.1 | <0.5 | 0.02 | 0.2 | <0.5 |
| LS1 | 3BC | 0.37 | 0.06 | <0.02 | 0.6 | 14.6 | 19.3 | 41 | 22.0 | 9.5 | <0.1 | 0.3 | <0.1 | 1.1 | 0.01 | 0.2 | <0.5 |
| LS2 | AE | 0.46 | 2.09 | <0.02 | 0.2 | 5.0 | 19.2 | 22 | 59.5 | 5.2 | 0.2 | 0.2 | <0.1 | 1.0 | 0.04 | <0.1 | <0.5 |
| LS2 | E | 0.51 | 0.69 | <0.02 | 0.7 | 8.6 | 10.6 | 28 | 96.7 | 4.1 | <0.1 | 0.1 | <0.1 | 1.5 | 0.02 | <0.1 | <0.5 |
| LS2 | EB | 0.50 | 0.54 | <0.02 | 0.2 | 11.7 | 11.1 | 36 | 94.2 | 6.6 | 0.1 | 0.2 | <0.1 | 1.3 | 0.03 | 0.1 | <0.5 |
| LS2 | 2Bt1 | 0.48 | 0.55 | <0.02 | 0.3 | 17.2 | 12.4 | 38 | 171.4 | 7.5 | <0.1 | 0.1 | <0.1 | 3.7 | 0.04 | 0.1 | <0.5 |
| LS2 | 2Bt2 | 0.52 | 0.40 | <0.02 | 0.2 | 20.4 | 12.2 | 43 | 254.9 | 7.4 | 0.1 | 0.1 | <0.1 | 2.7 | 0.04 | 0.1 | 2.0 |
| LS2 | 3BC | 0.45 | 0.53 | <0.02 | 0.4 | 20.2 | 10.2 | 30 | 689.4 | 5.6 | 0.1 | 0.2 | <0.1 | 0.8 | 0.05 | 0.1 | 0.6 |
| LS3 | ABw | 0.43 | 3.54 | 0.02 | 0.7 | 4.9 | 28.9 | 13 | 3.5 | 6.8 | 0.2 | 0.4 | <0.1 | 0.6 | 0.06 | <0.1 | <0.5 |
| LS3 | Bw1 (t) | 0.43 | 1.04 | <0.02 | 0.3 | 3.6 | 8.8 | 18 | 4.2 | 3.2 | <0.1 | 0.1 | <0.1 | <0.5 | 0.04 | <0.1 | <0.5 |
| LS3 | 2Bt | 0.44 | 0.75 | <0.02 | 0.2 | 6.5 | 7.2 | 18 | 5.9 | 3.3 | <0.1 | 0.1 | <0.1 | <0.5 | 0.05 | <0.1 | 0.8 |
| LS3 | 2BC | 0.44 | 0.33 | <0.02 | 0.7 | 9.3 | 6.0 | 20 | 8.1 | 2.9 | <0.1 | <0.1 | <0.1 | <0.5 | 0.04 | <0.1 | <0.5 |
| LS3 | 3BC | 0.39 | 0.27 | <0.02 | 0.2 | 8.5 | 4.4 | 35 | 5.5 | 3.3 | <0.1 | 0.1 | <0.1 | <0.5 | 0.02 | <0.1 | <0.5 |
| LS3 | 3CR | 0.51 | 0.26 | <0.02 | 0.5 | 9.3 | 5.1 | 54 | 4.4 | 3.0 | <0.1 | <0.1 | <0.1 | <0.5 | 0.02 | <0.1 | <0.5 |
| LS4 | AE | 0.47 | 1.14 | <0.02 | 0.5 | 10.6 | 27.7 | 35 | 10.4 | 5.5 | 0.2 | 0.3 | <0.1 | 0.8 | 0.07 | 0.1 | 0.6 |
| LS4 | EB | 0.40 | 0.55 | <0.02 | 0.4 | 13.4 | 10.7 | 30 | 12.7 | 4.8 | 0.1 | 0.2 | <0.1 | <0.5 | 0.04 | <0.1 | <0.5 |
| LS4 | 2Btg1 | 0.21 | 0.56 | <0.02 | 0.2 | 29.7 | 6.0 | 27 | 31.9 | 4.6 | <0.1 | 0.1 | <0.1 | 1.5 | 0.04 | <0.1 | <0.5 |
| LS4 | 2Btg2 | 0.25 | 0.30 | <0.02 | 0.3 | 18.6 | 6.7 | 21 | 16.5 | 4.4 | 0.1 | <0.1 | <0.1 | 0.9 | 0.04 | <0.1 | <0.5 |
| LS4 | 2BC | 0.32 | 0.46 | <0.02 | 0.4 | 28.1 | 7.6 | 23 | 20.1 | 5.1 | 0.2 | <0.1 | <0.1 | 0.8 | 0.11 | <0.1 | 0.5 |
| LS4 | 2BC (wedges) | 0.29 | 0.56 | <0.02 | 0.1 | 38.1 | 6.4 | 27 | 31.4 | 3.3 | 0.2 | <0.1 | <0.1 | 1.3 | 0.10 | <0.1 | <0.5 |
| LS5 | Eg | 0.40 | 0.63 | <0.02 | 0.3 | 3.5 | 8.7 | 17 | 5.9 | 2.7 | 0.1 | <0.1 | <0.1 | 2.0 | 0.03 | <0.1 | <0.5 |
| LS5 | Eg/Btg | 0.37 | 0.39 | <0.02 | 0.3 | 9.9 | 12.3 | 38 | 15.7 | 6.4 | 0.1 | 0.2 | <0.1 | 1.0 | 0.04 | 0.1 | <0.5 |
| LS5 | Btg1 | 0.40 | 0.23 | <0.02 | 0.1 | 11.5 | 10.8 | 28 | 20.3 | 3.5 | <0.1 | 0.1 | <0.1 | 1.7 | 0.04 | 0.1 | <0.5 |
| LS5 | 2CBtg | 0.51 | 0.33 | <0.02 | 0.4 | 23.0 | 13.4 | 48 | 68.3 | 6.8 | <0.1 | 0.2 | <0.1 | 3.4 | 0.15 | 0.1 | 0.5 |

Tab. C3: Measured Elements of each horizon.

| Profile/horizon | LS1-AE | LS1-AE | LS1-2BgE | LS1-2BgE | LS1-3BC | LS1-3BC | LS2-E | LS2-E | LS2-2Bt1 | LS2-2Bt1 | LS2-2BC | LS2-2BC | LS3-Bw | LS3-Bw |
|---|---|---|---|---|---|---|---|---|---|---|---|---|---|---|
| | No. Grains | percentage | No. Grains | percentage | No. Grains | percentage | No. Grains | percentage | No. Grains | percentage | No. Grains | percentage | No. Grains | percentage |
| Al2SiO5 | 0 | 0.0 | 3 | 2.2 | 0 | 0.0 | 0 | 0.0 | 0 | 0.0 | 0 | 0.0 | 0 | 0.0 |
| Albite | 0 | 0.0 | 0 | 0.0 | 3 | 1.4 | 0 | 0.0 | 0 | 0.0 | 0 | 0.0 | 0 | 0.0 |
| Amphibole | 5 | 2.6 | 10 | 7.2 | 0 | 0.0 | 22 | 10.0 | 13 | 5.6 | 0 | 0.0 | 6 | 2.9 |
| Apatite | 2 | 1.1 | 0 | 0.0 | 0 | 0.0 | 0 | 0.0 | 0 | 0.0 | 0 | 0.0 | 0 | 0.0 |
| Biotite | 4 | 2.1 | 3 | 2.2 | 7 | 3.3 | 0 | 0.0 | 0 | 0.0 | 0 | 0.0 | 0 | 0.0 |
| Chlorite | 2 | 1.1 | 0 | 0.0 | 0 | 0.0 | 0 | 0.0 | 0 | 0.0 | 0 | 0.0 | 0 | 0.0 |
| Chrysotile | 0 | 0.0 | 0 | 0.0 | 0 | 0.0 | 0 | 0.0 | 0 | 0.0 | 0 | 0.0 | 0 | 0.0 |
| Epidote-groupe | 4 | 2.1 | 6 | 4.3 | 0 | 0.0 | 8 | 3.7 | 7 | 3.0 | 10 | 4.9 | 12 | 5.7 |
| Fe-oxide | 58 | 30.5 | 37 | 26.8 | 71 | 33.2 | 7 | 3.2 | 3 | 1.3 | 11 | 5.4 | 71 | 34.0 |
| Garnet | 17 | 8.9 | 14 | 10.1 | 0 | 0.0 | 13 | 5.9 | 5 | 2.2 | 8 | 3.9 | 14 | 6.7 |
| Ilmenite | 23 | 12.1 | 13 | 9.4 | 46 | 21.5 | 3 | 1.4 | 5 | 2.2 | 16 | 7.8 | 35 | 16.7 |
| Magnesiochromite & Magnetite | 33 | 17.4 | 20 | 14.5 | 35 | 16.4 | 152 | 69.4 | 169 | 73.2 | 137 | 66.8 | 27 | 12.9 |
| Monazite | 2 | 1.1 | 1 | 0.7 | 3 | 1.4 | 0 | 0.0 | 2 | 0.9 | 2 | 1.0 | 6 | 2.9 |
| Olivine & Pyroxene | 0 | 0.0 | 0 | 0.0 | | 0.0 | 8 | 3.7 | 19 | 8.2 | 13 | 6.3 | 2 | 1.0 |
| Pumpellyite | 0 | 0.0 | 0 | 0.0 | 0 | 0.0 | 0 | 0.0 | 0 | 0.0 | 0 | 0.0 | 0 | 0.0 |
| Rutile | 24 | 12.6 | 19 | 13.8 | 18 | 8.4 | 3 | 1.4 | 3 | 1.3 | 4 | 2.0 | 20 | 9.6 |
| Spinel | 0 | 0.0 | 0 | 0.0 | | 0.0 | | 0.0 | | 0.0 | 0 | 0.0 | 0 | 0.0 |
| Staurolite | 1 | 0.5 | 0 | 0.0 | 0 | 0.0 | 0 | 0.0 | 0 | 0.0 | 0 | 0.0 | 1 | 0.5 |
| Titanite | 0 | 0.0 | 2 | 1.4 | 0 | 0.0 | 0 | 0.0 | 0 | 0.0 | 0 | 0.0 | 0 | 0.0 |
| Tourmaline | 3 | 1.6 | 5 | 3.6 | 0 | 0.0 | 0 | 0.0 | 0 | 0.0 | 0 | 0.0 | 0 | 0.0 |
| Ulvospinel | 0 | 0.0 | 2 | 1.4 | 15 | 7.0 | 0 | 0.0 | 0 | 0.0 | 0 | 0.0 | 0 | 0.0 |
| Xenotime | 0 | 0.0 | 0 | 0.0 | 4 | 1.9 | 0 | 0.0 | 0 | 0.0 | 0 | 0.0 | 1 | 0.5 |
| Zircon | 5 | 2.6 | 3 | 2.2 | 11 | 5.1 | 0 | 0.0 | 1 | 0.4 | 3 | 1.5 | 14 | 6.7 |
| Zoisite | 0 | 0.0 | 0 | 0.0 | 0 | 0.0 | 0 | 0.0 | 0 | 0.0 | 0 | 0.0 | 0 | 0.0 |
| other | 7 | 3.7 | 0 | 0.0 | 1 | 0.5 | 3 | 1.4 | 4 | 1.7 | 1 | 0.5 | 0 | 0.0 |
| Total | 190 | 100 | 138 | 100 | 214 | 100 | 219 | 100 | 231 | 100 | 205 | 100 | 209 | 100 |

Tab. D1: Counted heavy mineral grains and resulting percentages of the SEM measurements for LS1, LS2 and LS3.

| Profile/horizon | LS3-2BC | LS3-2BC | LS3-3BC | LS3-3BC | LS4-AE | LS4-AE | LS4-2Btg1 | LS4-2Btg1 | LS4-2BC | LS4-2BC | LS5-Aeg | LS5-Btg1 | LS5-BCg2 |
|---|---|---|---|---|---|---|---|---|---|---|---|---|---|
|  | No. Grains | percentage | No. Grains | percentage | No. Grains | percentage | No. Grains | percentage | No. Grains | percentage | percentage | percentage | percentage |
| Al2SiO5 | 0 | 0.0 | 0 | 0.0 | 0 | 0.0 | 0 | 0.0 | 0 | 0.0 | 0 | 0 | 0 |
| Albite | 0 | 0.0 | 0 | 0.0 | 0 | 0.0 | 0 | 0.0 | 0 | 0.0 | 0 | 0 | 0 |
| Amphibole | 0 | 0.0 | 0 | 0.0 | 58 | 29.1 | 63 | 29.3 | 46 | 22.2 | 18 | 15 | 11 |
| Apatite | 0 | 0.0 | 0 | 0.0 | 2 | 1.0 | 0 | 0.0 | 0 | 0.0 | 0 | 0 | 0 |
| Biotite | 2 | 0.9 | 41 | 18.0 | 3 | 1.5 | 0 | 0.0 | 0 | 0.0 | 0 | 0 | 0 |
| Chlorite | 0 | 0.0 | 0 | 0.0 | 0 | 0.0 | 0 | 0.0 | 0 | 0.0 | 0 | 0 | 0 |
| Chrysotile | 0 | 0.0 | 0 | 0.0 | 0 | 0.0 | 0 | 0.0 | 0 | 0.0 | 0 | 0 | 0 |
| Epidote-groupe | 15 | 6.8 | 0 | 0.0 | 0 | 0.0 | 102 | 47.4 | 116 | 56.0 | 23 | 16 | 9 |
| Fe-oxide | 52 | 23.7 | 18 | 7.9 | 14 | 7.0 | 3 | 1.4 | 7 | 3.4 | 2 | 5 | 3 |
| Garnet | 7 | 3.2 | 0 | 0.0 | 12 | 6.0 | 3 | 1.4 | 2 | 1.0 | 0 | 0 | 0 |
| Ilmenite | 40 | 18.3 | 3 | 1.3 | 20 | 10.1 | 20 | 9.3 | 16 | 7.7 | 11 | 12 | 11 |
| Magnesiochromite & Magnetite | 9 | 4.1 | 0 | 0.0 | 55 | 27.6 | 9 | 4.2 | 4 | 1.9 | 0 | 0 | 0 |
| Monazite | 8 | 3.7 | 8 | 3.5 | 4 | 2.0 | 0 | 0.0 | 1 | 0.5 | 1 | 2 | 1 |
| Olivine & Pyroxene |  | 0.0 | 0 | 0.0 | 5 | 2.5 | 0 | 0.0 | 5 | 2.4 | 5 | 7 | 18 |
| Pumpellyite | 0 | 0.0 | 0 | 0.0 | 0 | 0.0 | 0 | 0.0 | 2 | 1.0 | 10 | 10 | 12 |
| Rutile | 69 | 31.5 | 152 | 66.7 | 10 | 5.0 | 3 | 1.4 | 2 | 1.0 | 18 | 6 | 5 |
| Spinel | 0 | 0.0 | 0 | 0.0 | 0 | 0.0 | 0 | 0.0 | 0 | 0.0 | 2 | 0 | 1 |
| Staurolite | 7 | 3.2 | 0 | 0.0 | 1 | 0.5 | 0 | 0.0 | 0 | 0.0 | 0 | 1 | 1 |
| Titanite | 0 | 0.0 | 0 | 0.0 | 2 | 1.0 | 0 | 0.0 | 0 | 0.0 | 3 | 9 | 0 |
| Tourmaline | 0 | 0.0 | 0 | 0.0 | 2 | 1.0 | 2 | 0.9 | 2 | 1.0 | 0 | 0 | 0 |
| Ulvospinel | 0 | 0.0 | 0 | 0.0 | 0 | 0.0 | 0 | 0.0 | 0 | 0.0 | 5 | 12 | 25 |
| Xenotime | 0 | 0.0 | 5 | 2.2 | 0 | 0.0 | 1 | 0.5 | 0 | 0.0 | 1 | 0 | 0 |
| Zircon | 9 | 4.1 | 0 | 0.0 | 9 | 4.5 | 7 | 3.3 | 0 | 0.0 | 3 | 5 | 2 |
| Zoisite | 0 | 0.0 | 0 | 0.0 | 0 | 0.0 | 0 | 0.0 | 3 | 1.4 | 0 | 0 | 0 |
| other | 1 | 0.5 | 1 | 0.4 | 2 | 1.0 | 2 | 0.9 | 1 | 0.5 | 2 | 1 | 3 |
| Total | 219 | 100 | 228 | 100 | 199 | 100 | 215 | 100 | 207 | 100 | 104 | 101 | 102 |

Tab. D2: Counted heavy mineral grains and resulting percentages of the SEM measurements for LS3, LS4 and LS5.
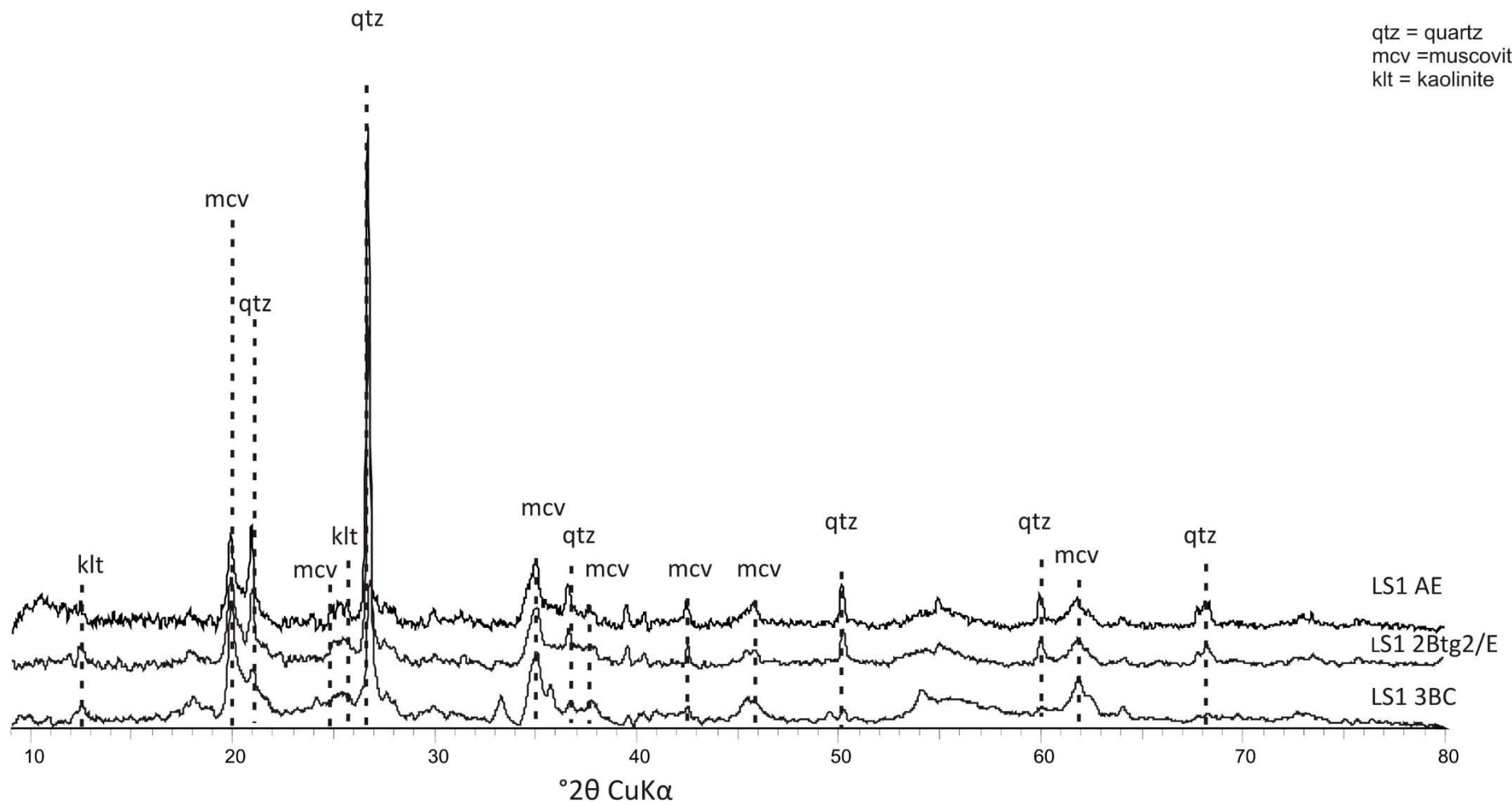
Fig. E1: XRD-plot from 10°2θ to 80°2θ for LS1.
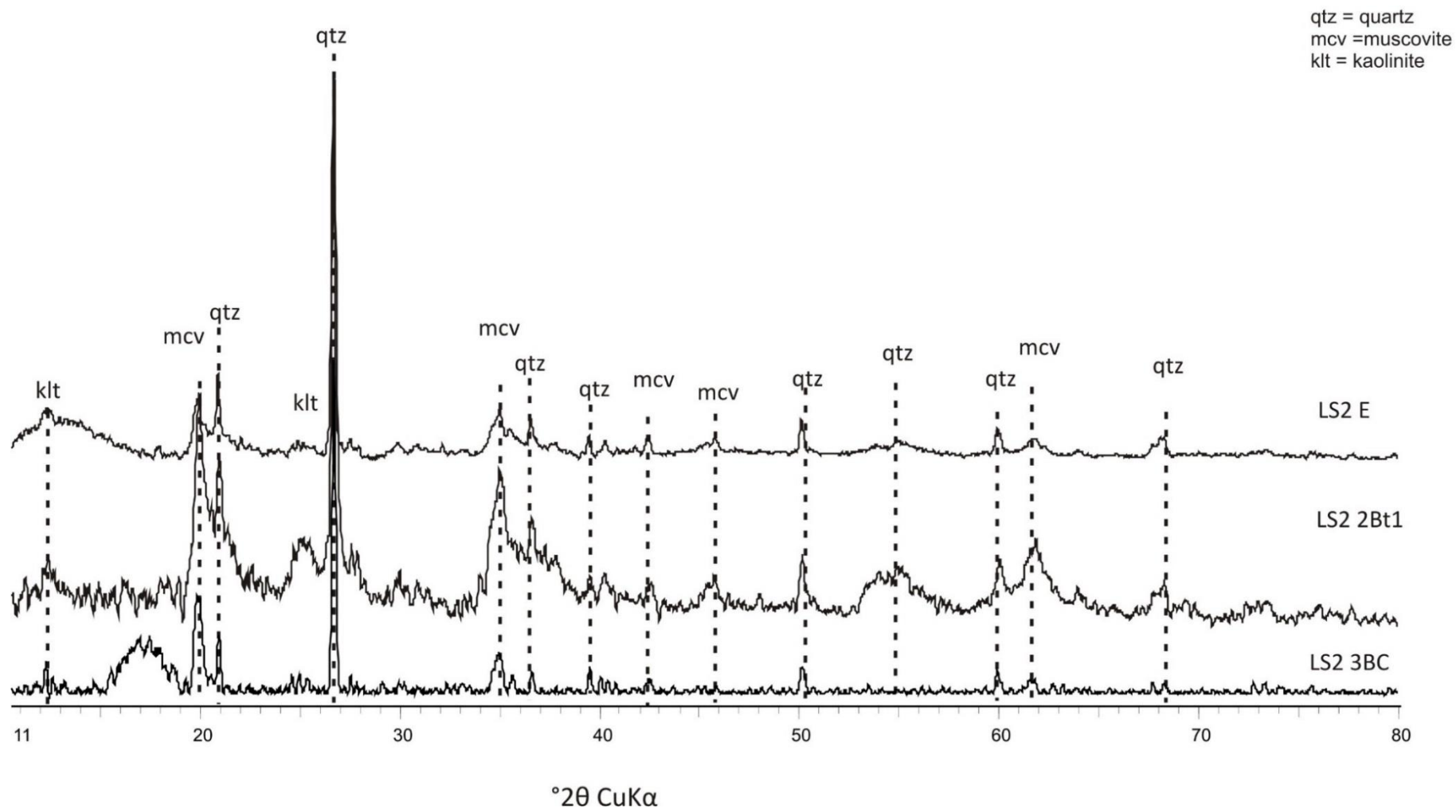
Fig. E2: XRD-plot from 11°2θ to 80°2θ for LS2.

qtz = quartz
mcv = muscovite
klt = kaolinite
orth = orthoclase

°2θ CuKα
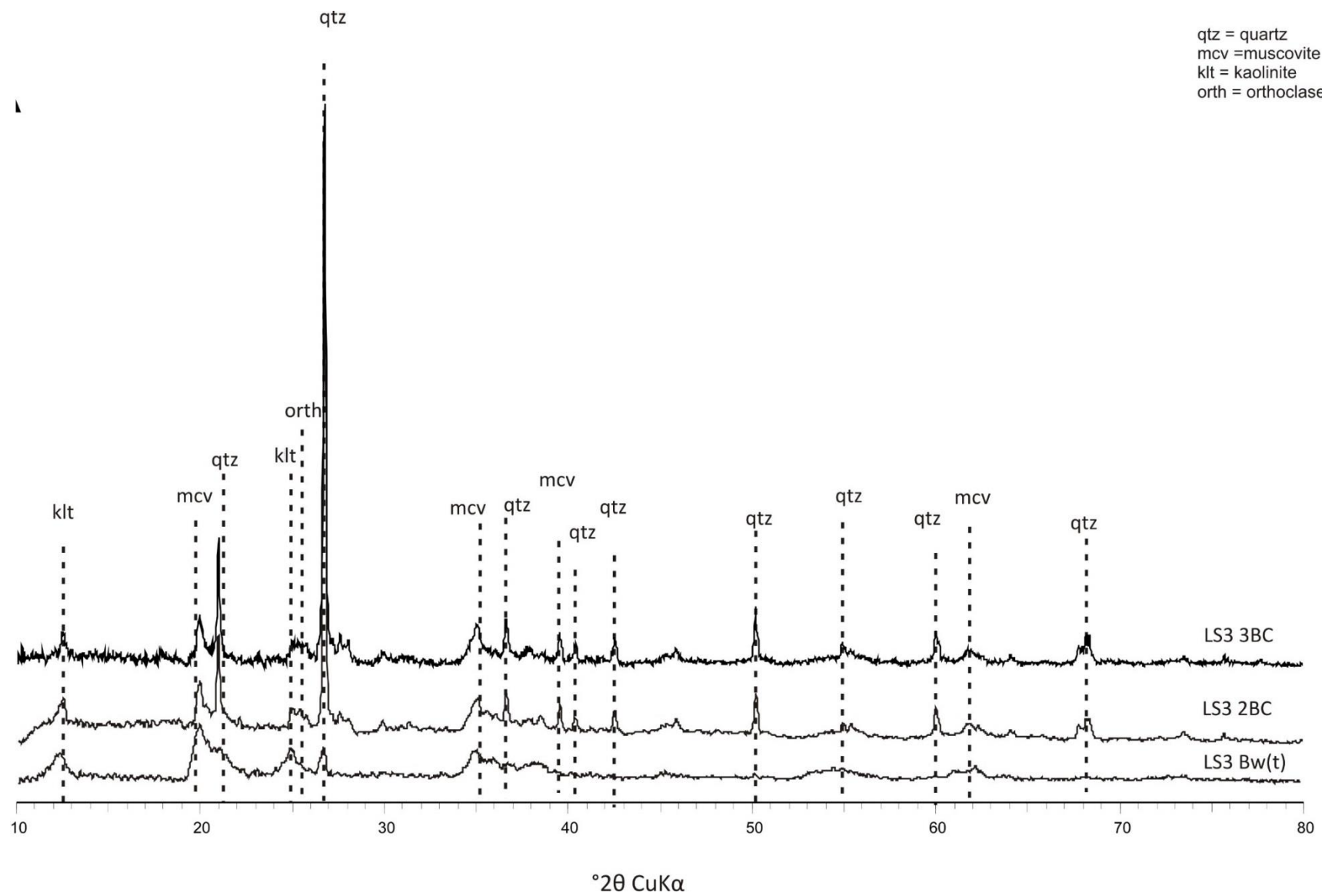
Fig. E3: XRD-plot from 10°2θ to 80°2θ for LS3.
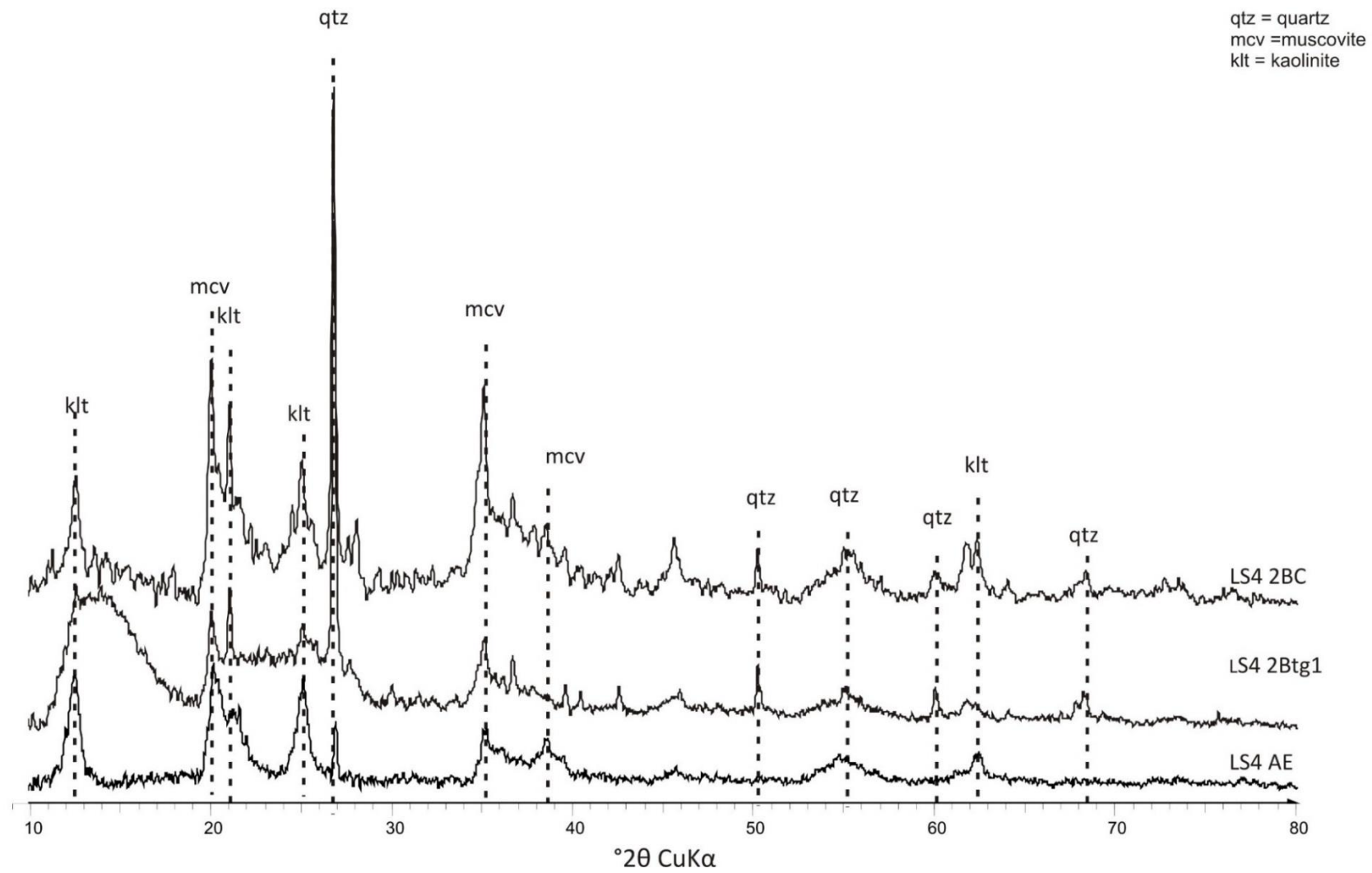
Fig. E4: XRD-plot from 10°2θ to 80°2θ for LS4.
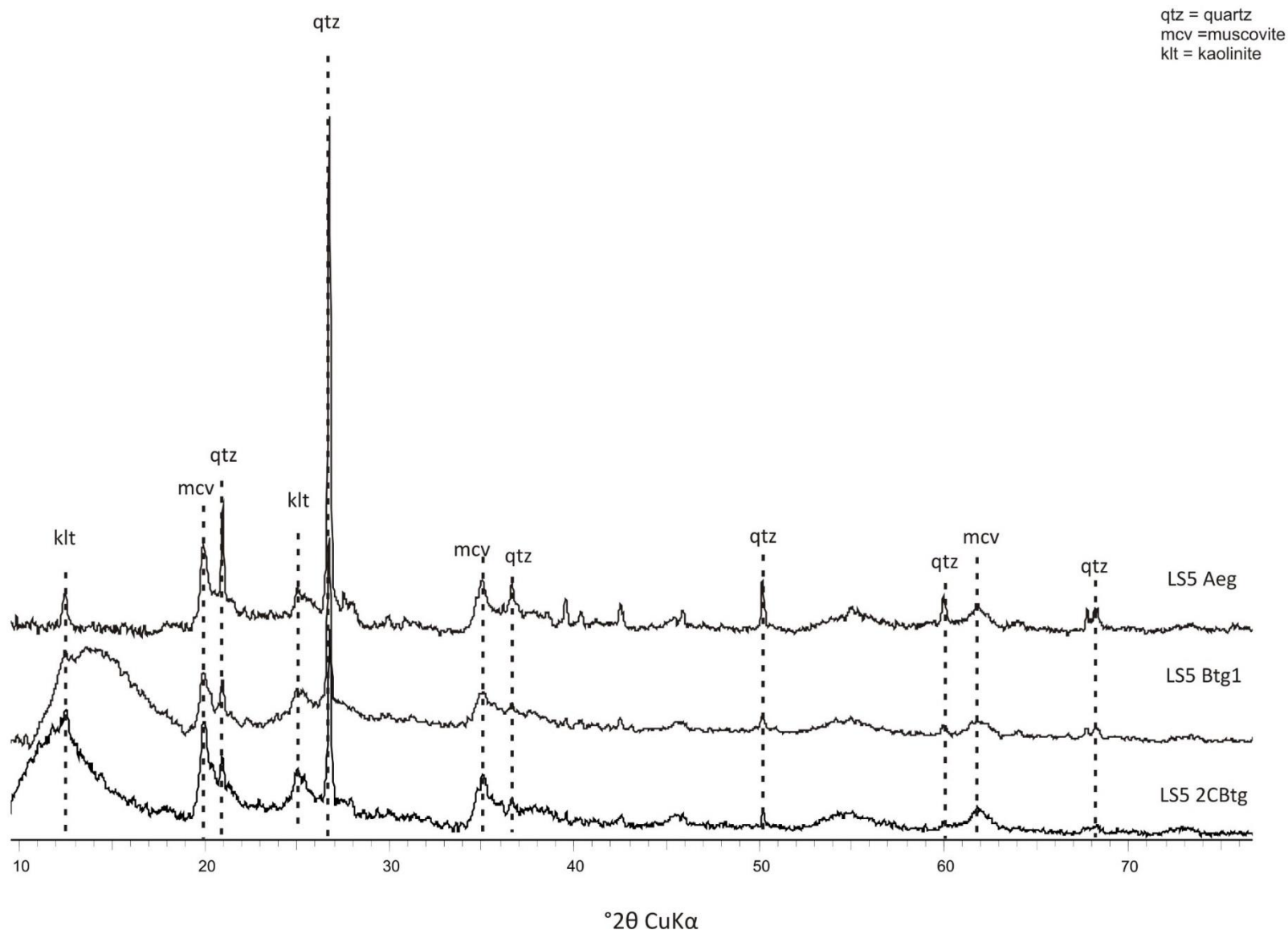
Fig. E5: XRD-plot from 10°2θ to 80°2θ for LS5.

| Sample # | 1 | 1 | 2 | 2 | 3 | 3 | 4 | 4 | 5 | 5 | 6 | 6 | 7 | 7 |
|---|---|---|---|---|---|---|---|---|---|---|---|---|---|---|
| | [%] | [%norm] | [%] | [%norm] | [%] | [%norm] | [%] | [%norm] | [%] | [%norm] | [%] | [%norm] | [%] | [%norm] |
| Quartz | 96.3 | 58.3 | 99.7 | 53.4 | 194.8 | 35.6 | 104.9 | 59.2 | 172.1 | 52.8 | 98.4 | 53.3 | 276.0 | 39.6 |
| Plagioclase | 4.6 | 2.8 | 3.5 | 1.9 | 17.0 | 3.1 | 3.9 | 2.2 | 13.1 | 4.0 | 4.8 | 2.6 | 16.0 | 2.3 |
| Orthoclase | 7.0 | 4.3 | 6.7 | 3.6 | 30.9 | 5.6 | 6.6 | 3.7 | 14.1 | 4.3 | 5.7 | 3.1 | 19.2 | 2.8 |
| Amphibole | 5.5 | 3.3 | 4.5 | 2.4 | 18.8 | 3.4 | 4.7 | 2.7 | 5.2 | 1.6 | 6.2 | 3.3 | 17.1 | 2.5 |
| Biotite | 4.0 | 2.4 | 4.0 | 2.2 | 22.6 | 4.1 | 4.8 | 2.7 | 8.8 | 2.7 | 5.3 | 2.9 | 22.5 | 3.2 |
| Muscovite | 13.4 | 8.1 | 15.2 | 8.2 | 87.8 | 16.0 | 15.6 | 8.8 | 33.8 | 10.4 | 23.8 | 12.9 | 102.7 | 14.7 |
| Magnetite | 5.6 | 3.4 | 5.7 | 3.0 | 50.3 | 9.2 | 6.8 | 3.8 | 15.4 | 4.7 | 6.8 | 3.7 | 38.1 | 5.5 |
| Ilmenite | 3.2 | 2.0 | 2.7 | 1.4 | 18.3 | 3.3 | 2.4 | 1.4 | 5.4 | 1.7 | 3.3 | 1.8 | 14.1 | 2.0 |
| Rutile | 4.5 | 2.7 | 6.8 | 3.6 | 22.9 | 4.2 | 4.6 | 2.6 | 16.1 | 4.9 | 6.4 | 3.5 | 17.2 | 2.5 |
| Garnet | 4.3 | 2.6 | 3.8 | 2.1 | 6.2 | 1.1 | 4.1 | 2.3 | 5.5 | 1.7 | 2.6 | 1.4 | 14.3 | 2.0 |
| Kaolinite | 9.7 | 5.9 | 10.7 | 5.7 | 17.9 | 3.3 | 12.1 | 6.8 | 27.6 | 8.5 | 10.0 | 5.4 | 97.1 | 13.9 |
| Chlorite | 7.0 | 4.3 | 0.0 | 0.0 | 13.9 | 2.5 | 6.8 | 3.8 | 8.9 | 2.7 | 4.1 | 2.2 | 24.8 | 3.6 |
| Epidote | 0.0 | 0.0 | 1.8 | 0.9 | 0.0 | 0.0 | 0.0 | 0.0 | 0.0 | 0.0 | 0.0 | 0.0 | 0.0 | 0.0 |
| Titanite | 0.0 | 0.0 | 6.3 | 3.3 | 0.0 | 0.0 | 0.0 | 0.0 | 0.0 | 0.0 | 0.0 | 0.0 | 0.0 | 0.0 |
| Kyanite | 0.0 | 0.0 | 4.5 | 2.4 | 0.0 | 0.0 | 0.0 | 0.0 | 0.0 | 0.0 | 0.0 | 0.0 | 0.0 | 0.0 |
| Zircon | 0.0 | 0.0 | 11.0 | 5.9 | 0.0 | 0.0 | 0.0 | 0.0 | 0.0 | 0.0 | 0.0 | 0.0 | 37.2 | 5.3 |
| Albite | 0.0 | 0.0 | 0.0 | 0.0 | 12.3 | 2.3 | 0.0 | 0.0 | 0.0 | 0.0 | 0.0 | 0.0 | 0.0 | 0.0 |
| Ulvospinel | 0.0 | 0.0 | 0.0 | 0.0 | 33.3 | 6.1 | 0.0 | 0.0 | 0.0 | 0.0 | 0.0 | 0.0 | 0.0 | 0.0 |
| Olivine | 0.0 | 0.0 | 0.0 | 0.0 | 0.0 | 0.0 | 0.0 | 0.0 | 0.0 | 0.0 | 7.2 | 3.9 | 0.0 | 0.0 |
| Total | 165.3 | 100.0 | 186.7 | 100.0 | 547.0 | 100.0 | 177.2 | 100.0 | 326.0 | 100.0 | 184.6 | 100.0 | 696.4 | 100.0 |

Tab. F6: Detailed table for XRD-plots showing percentages and normative percentages of the investigated minerals.

| Sample # | 8 | 8 | 9 | 9 | 10 | 10 | 11 | 11 | 12 | 12 | 13 | 13 | 14 | 14 | 15 | 15 |
|---|---|---|---|---|---|---|---|---|---|---|---|---|---|---|---|---|
| | [%] | [%norm] | [%] | [%norm] | [%] | [%norm] | [%] | [%norm] | [%] | [%norm] | [%] | [%norm] | [%] | [%norm] | [%] | [%norm] |
| Quartz | 109.7 | 63.2 | 101.3 | 64.2 | 100.6 | 28.5 | 160.0 | 51.2 | 296.3 | 45.3 | 96.7 | 57.4 | 206.1 | 47.4 | 194.8 | 40.3 |
| Plagioclase | 4.0 | 2.3 | 3.7 | 2.3 | 15.6 | 4.4 | 9.8 | 3.1 | 11.9 | 1.8 | 4.9 | 2.9 | 18.1 | 4.2 | 17.5 | 3.6 |
| Orthoclase | 6.4 | 3.7 | 4.8 | 3.1 | 13.0 | 3.7 | 14.3 | 4.6 | 14.2 | 2.2 | 6.8 | 4.0 | 20.9 | 4.8 | 21.3 | 4.4 |
| Amphibole | 5.1 | 3.0 | 2.3 | 1.4 | 6.8 | 1.9 | 6.1 | 1.9 | 12.2 | 1.9 | 6.2 | 3.7 | 10.4 | 2.4 | 11.4 | 2.4 |
| Biotite | 3.3 | 1.9 | 1.3 | 0.8 | 11.6 | 3.3 | 7.2 | 2.3 | 11.0 | 1.7 | 4.6 | 2.7 | 23.0 | 5.3 | 24.1 | 5.0 |
| Muscovite | 12.2 | 7.0 | 9.2 | 5.8 | 44.2 | 12.5 | 19.5 | 6.2 | 51.7 | 7.9 | 4.4 | 2.6 | 30.8 | 7.1 | 54.0 | 11.2 |
| Magnetite | 5.9 | 3.4 | 3.5 | 2.2 | 16.9 | 4.8 | 9.9 | 3.2 | 31.1 | 4.7 | 5.6 | 3.3 | 19.2 | 4.4 | 21.8 | 4.5 |
| Ilmenite | 2.4 | 1.4 | 1.9 | 1.2 | 5.5 | 1.5 | 4.2 | 1.3 | 7.4 | 1.1 | 1.3 | 0.8 | 8.5 | 2.0 | 7.9 | 1.6 |
| Rutile | 6.3 | 3.6 | 4.3 | 2.7 | 11.8 | 3.3 | 13.9 | 4.4 | 13.2 | 2.0 | 7.1 | 4.2 | 21.5 | 4.9 | 16.6 | 3.4 |
| Garnet | 3.5 | 2.0 | 1.0 | 0.6 | 8.3 | 2.4 | 6.1 | 2.0 | 8.0 | 1.2 | 2.6 | 1.5 | 11.1 | 2.6 | 27.0 | 5.6 |
| Kaolinite | 10.6 | 6.1 | 20.4 | 12.9 | 109.8 | 31.1 | 41.7 | 13.3 | 171.0 | 26.1 | 19.8 | 11.8 | 53.8 | 12.4 | 75.4 | 15.6 |
| Chlorite | 4.4 | 2.5 | 4.3 | 2.7 | 9.0 | 2.5 | 8.5 | 2.7 | 14.8 | 2.3 | 8.4 | 5.0 | 11.3 | 2.6 | 11.8 | 2.4 |
| Epidote | 0.0 | 0.0 | 0.0 | 0.0 | 0.0 | 0.0 | 11.5 | 3.7 | 11.9 | 1.8 | 0.0 | 0.0 | 0.0 | 0.0 | 0.0 | 0.0 |
| Titanite | 0.0 | 0.0 | 0.0 | 0.0 | 0.0 | 0.0 | 0.0 | 0.0 | 0.0 | 0.0 | 0.0 | 0.0 | 0.0 | 0.0 | 0.0 | 0.0 |
| Kyanite | 0.0 | 0.0 | 0.0 | 0.0 | 0.0 | 0.0 | 0.0 | 0.0 | 0.0 | 0.0 | 0.0 | 0.0 | 0.0 | 0.0 | 0.0 | 0.0 |
| Zircon | 0.0 | 0.0 | 0.0 | 0.0 | 0.0 | 0.0 | 0.0 | 0.0 | 0.0 | 0.0 | 0.0 | 0.0 | 0.0 | 0.0 | 0.0 | 0.0 |
| Albite | 0.0 | 0.0 | 0.0 | 0.0 | 0.0 | 0.0 | 0.0 | 0.0 | 0.0 | 0.0 | 0.0 | 0.0 | 0.0 | 0.0 | 0.0 | 0.0 |
| Ulvospinel | 0.0 | 0.0 | 0.0 | 0.0 | 0.0 | 0.0 | 0.0 | 0.0 | 0.0 | 0.0 | 0.0 | 0.0 | 0.0 | 0.0 | 0.0 | 0.0 |
| Olivine | 0.0 | 0.0 | 0.0 | 0.0 | 0.0 | 0.0 | 0.0 | 0.0 | 0.0 | 0.0 | 0.0 | 0.0 | 0.0 | 0.0 | 0.0 | 0.0 |
| Total | 173.7 | 100.0 | 157.9 | 100.0 | 352.9 | 100.0 | 312.6 | 100.0 | 654.5 | 100.0 | 168.4 | 100.0 | 434.7 | 100.0 | 483.4 | 100.0 |

Tab. F7: Detailed table for XRD-plots showing percentages and normative percentages of the investigated minerals.
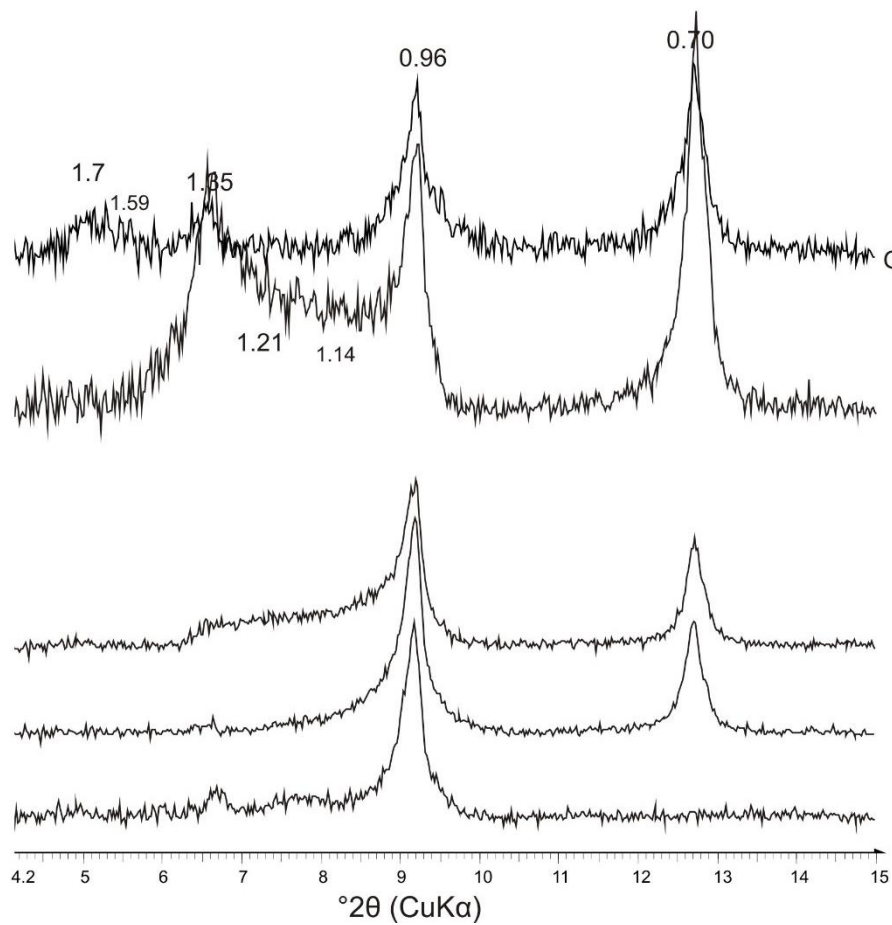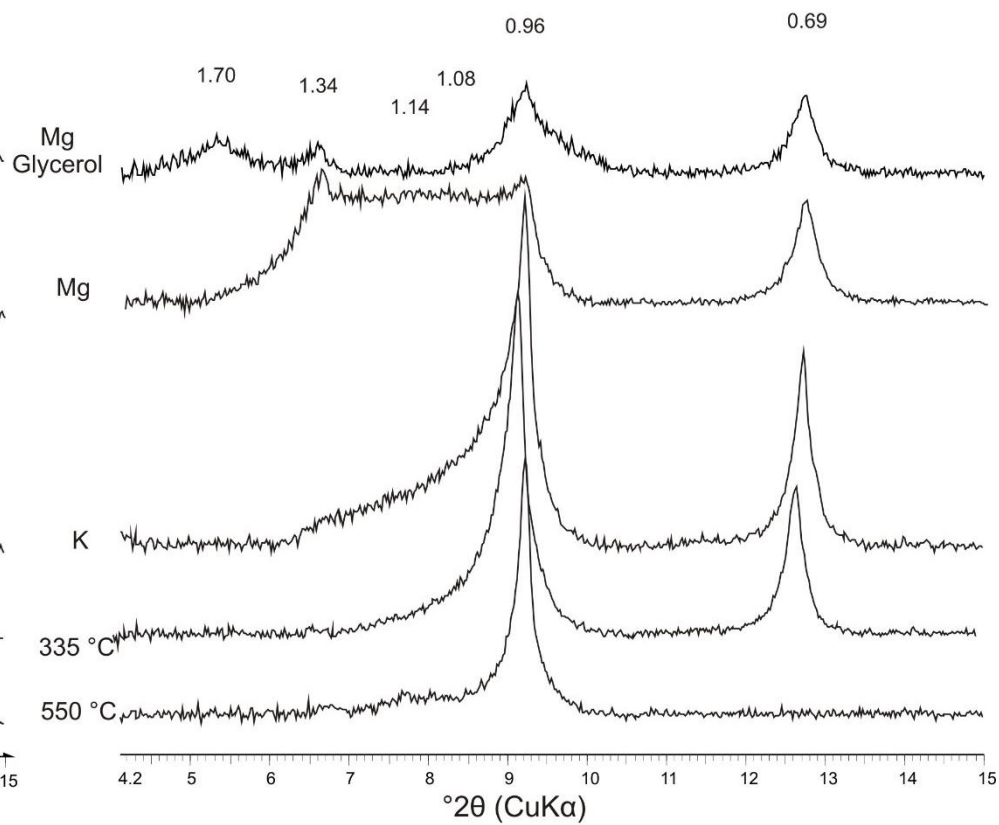
Fig. G1: XRD-plots from 4.2°2θ to 15°2θ for the AE and 2Btg/E horizons of LS1.
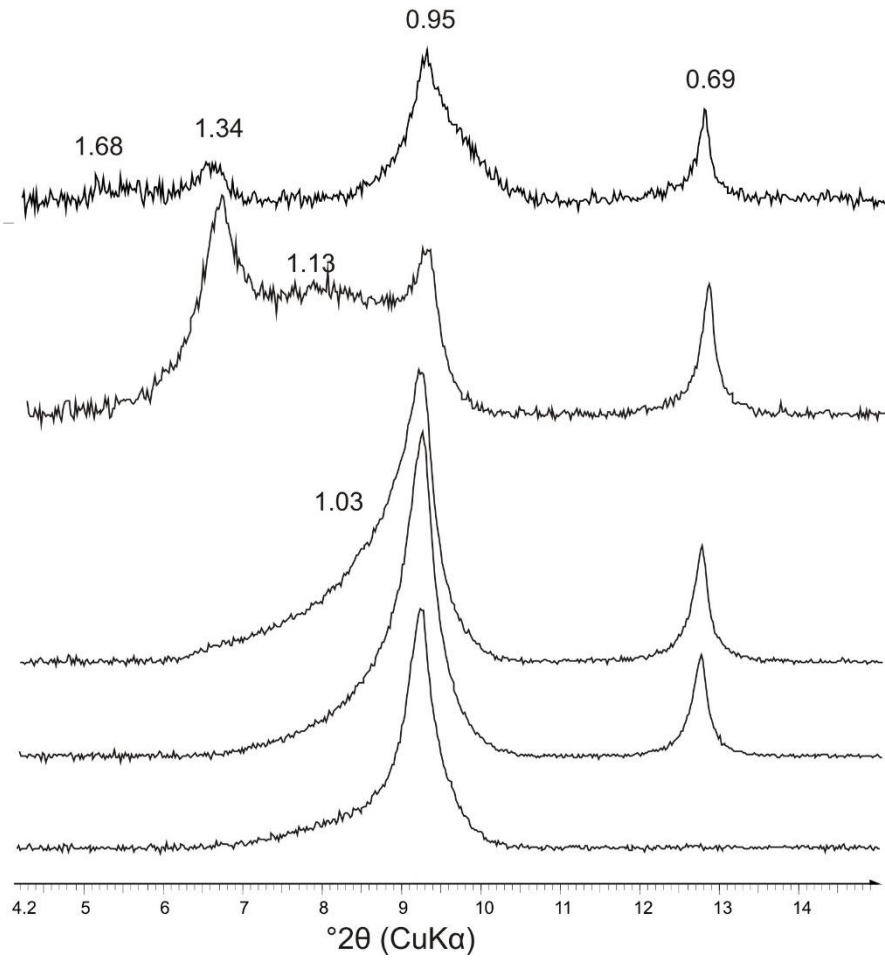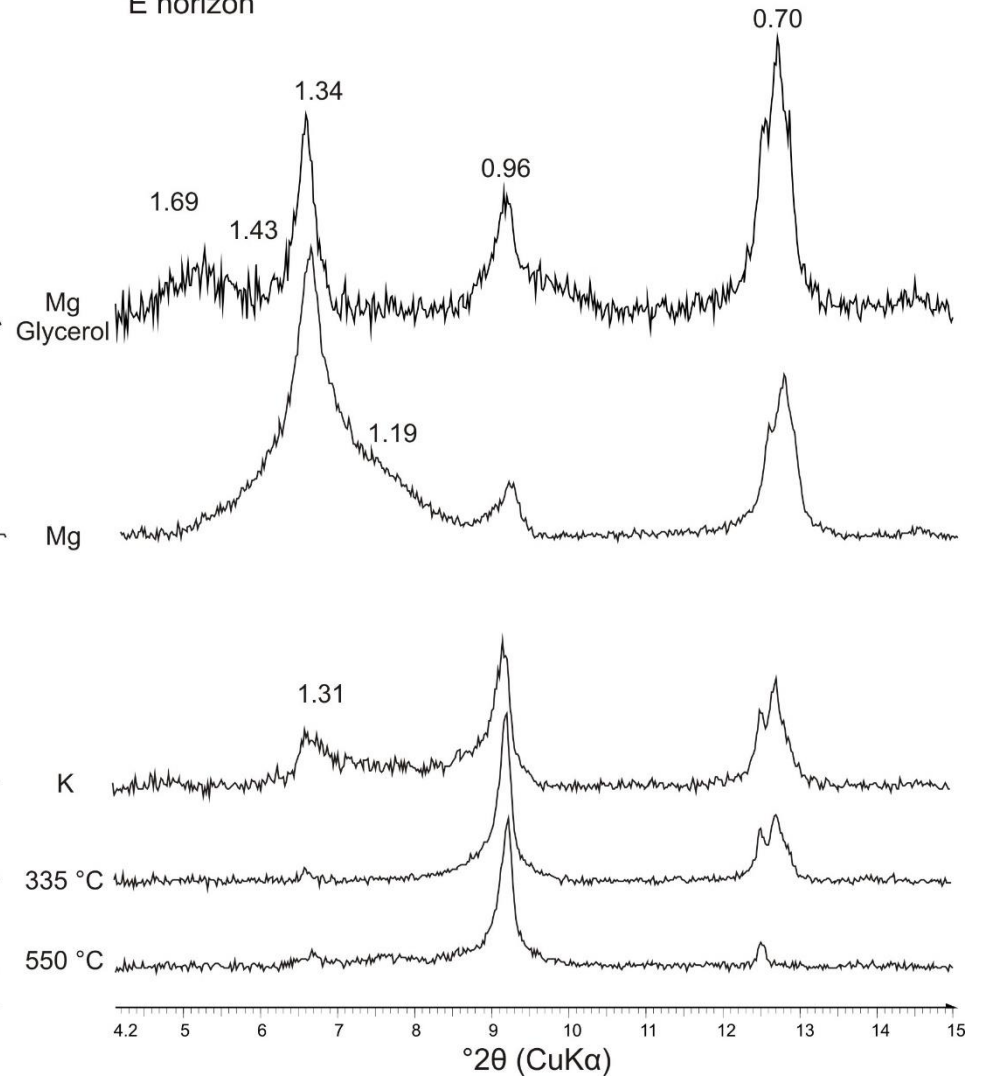
Fig. G2: XRD-plots from 4.2°2θ to 15°2θ for the 3BC horizon of LS1 and the E horizon of LS2.
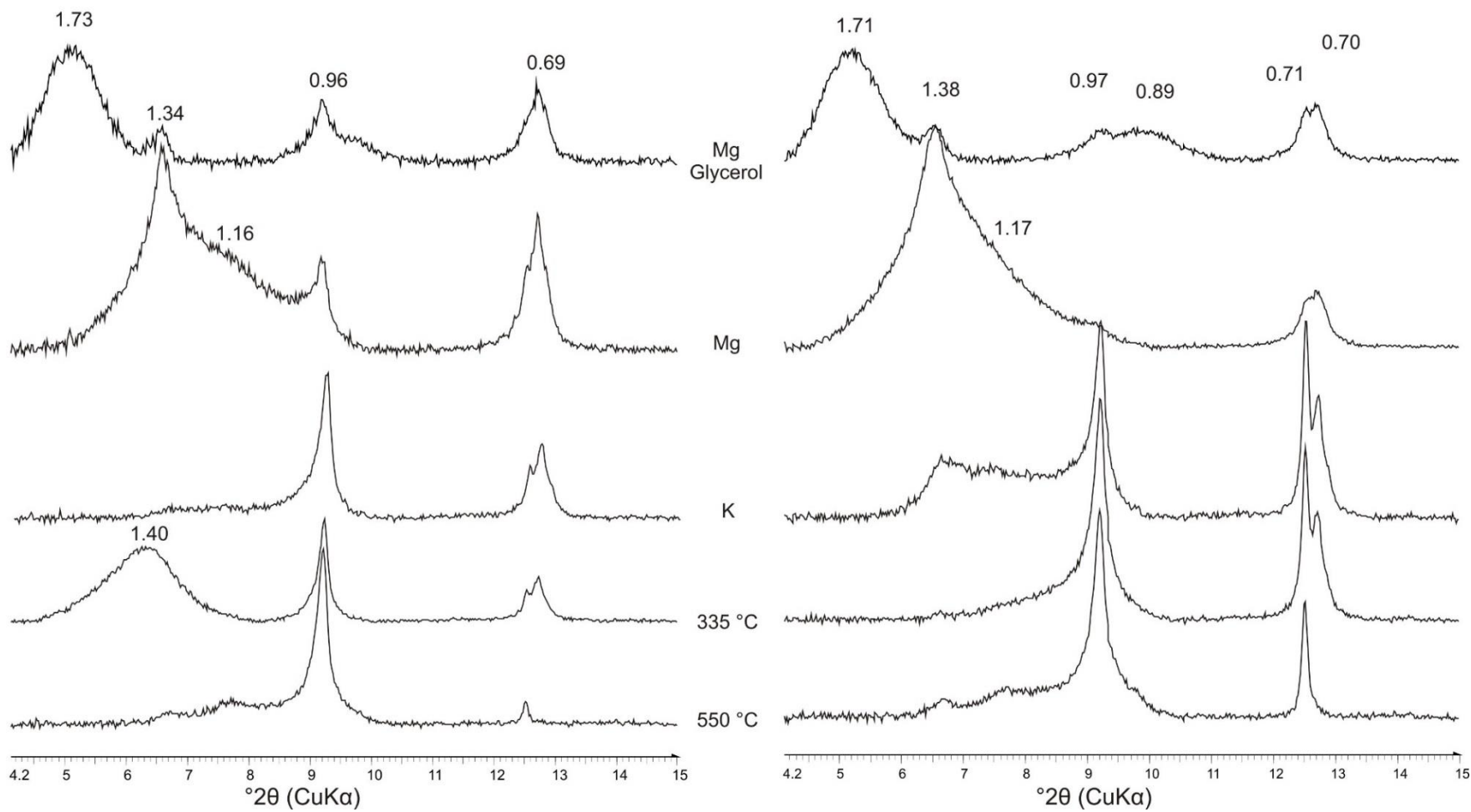
Fig. G3: XRD-plots from 4.2°2θ to 15°2θ for the 2Bt1 and 3BC horizons of LS2.
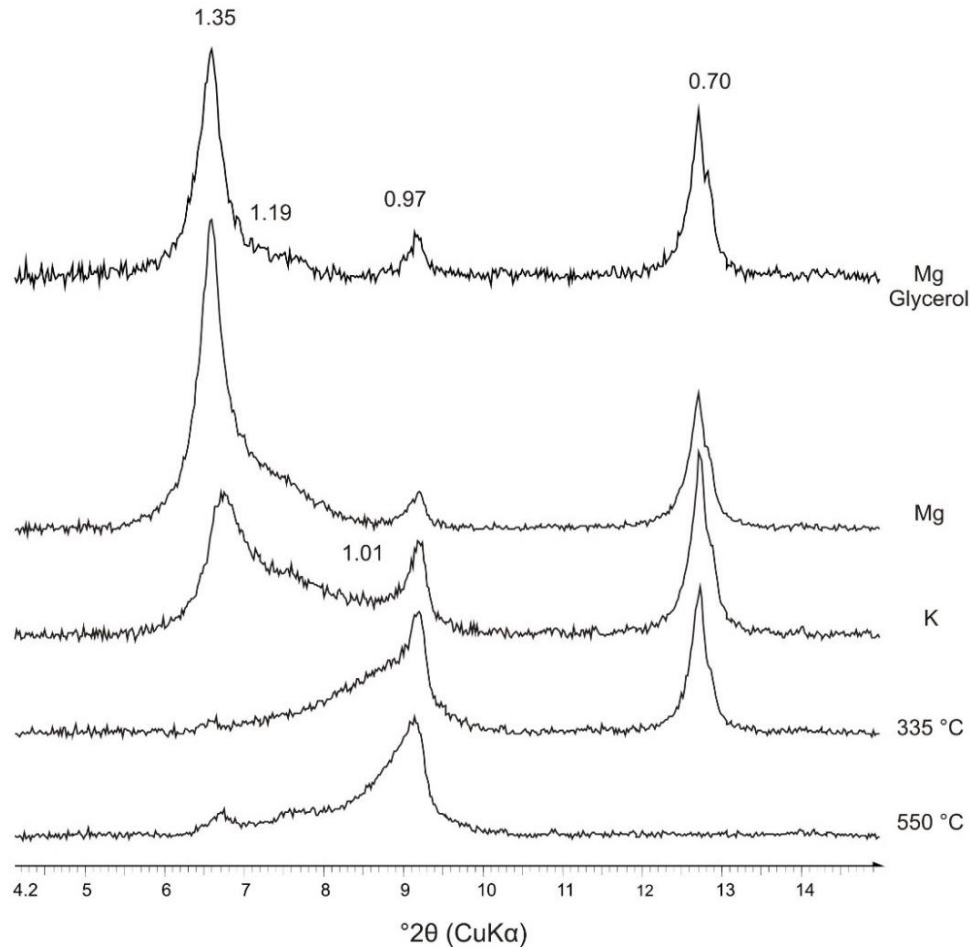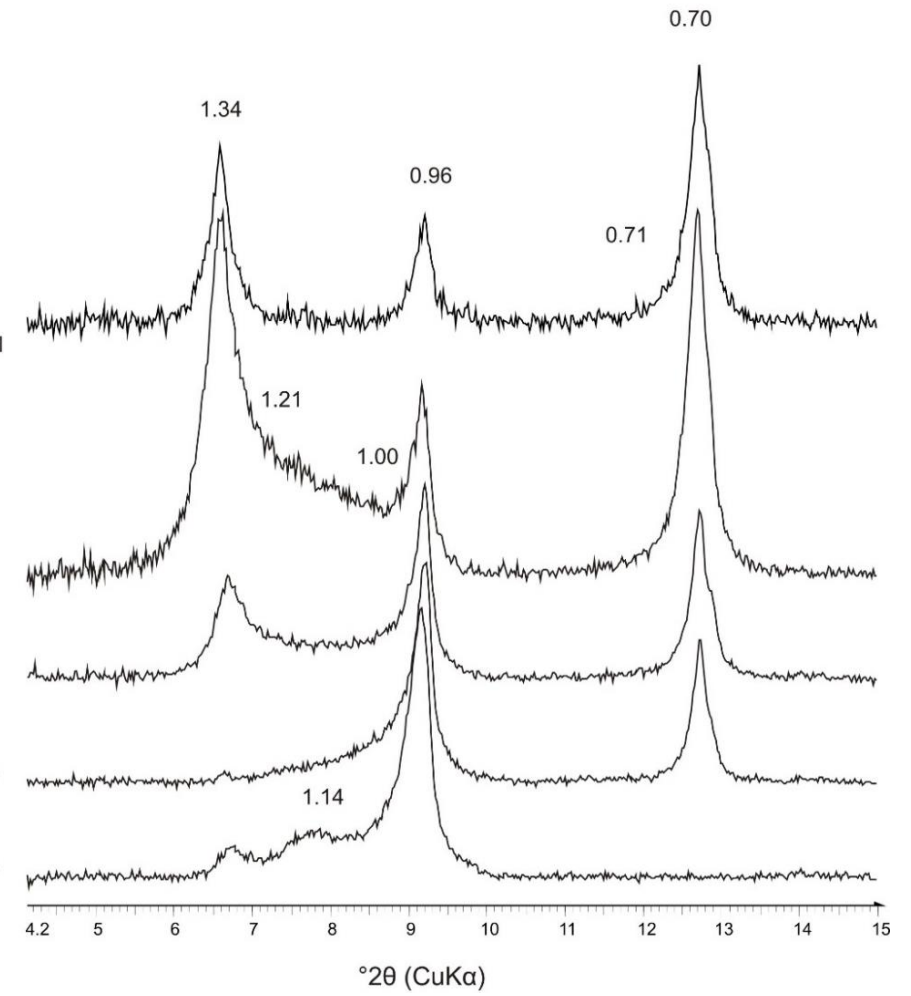
Fig. G4: XRD-plots from 4.2°2θ to 15°2θ for the Bw (t) and the 2BC horizons of LS3.
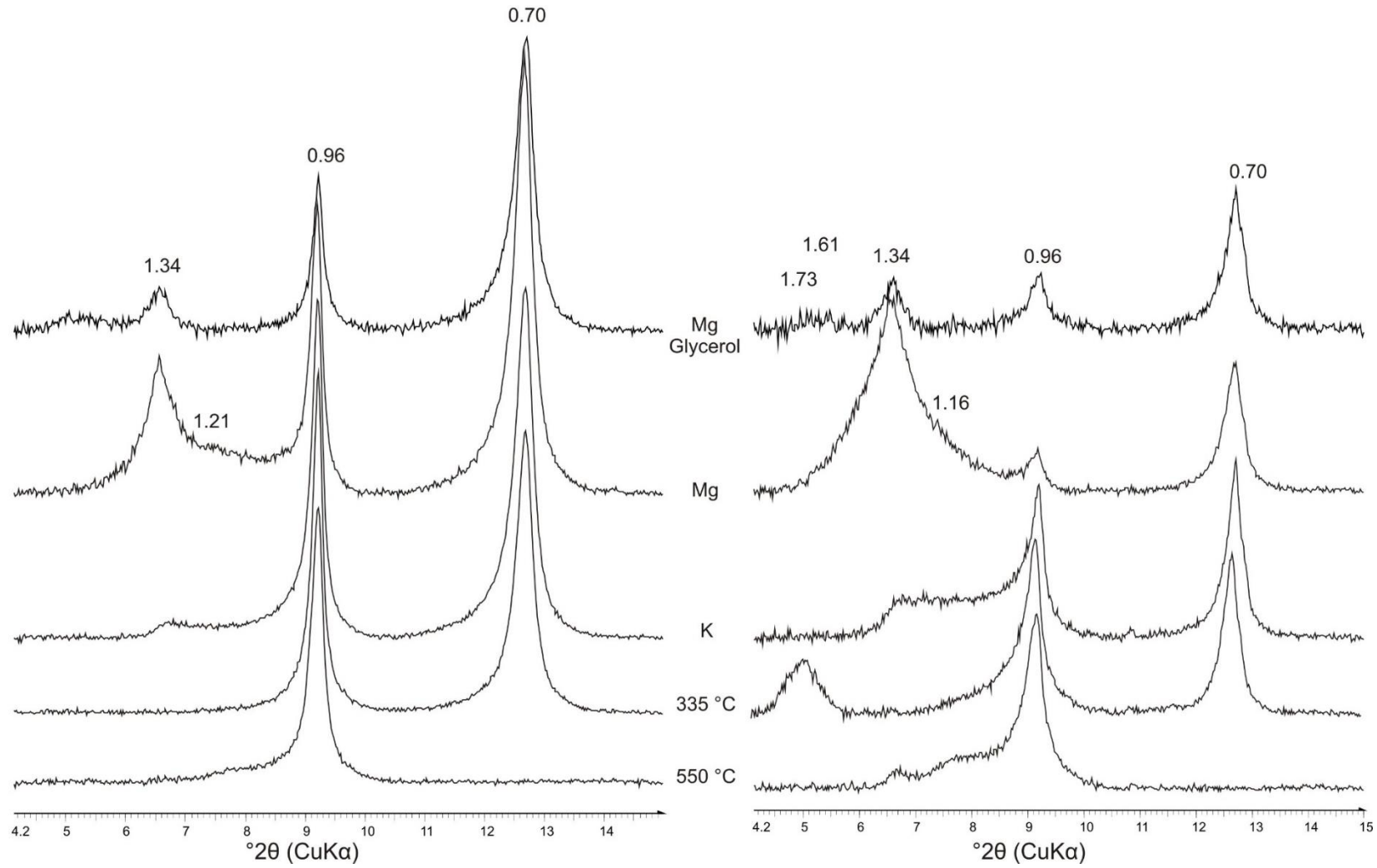
Fig. G5: XRD-plots from 4.2°2θ to 15°2θ for the 3BC horizon of LS3 and the AE horizon of LS4.
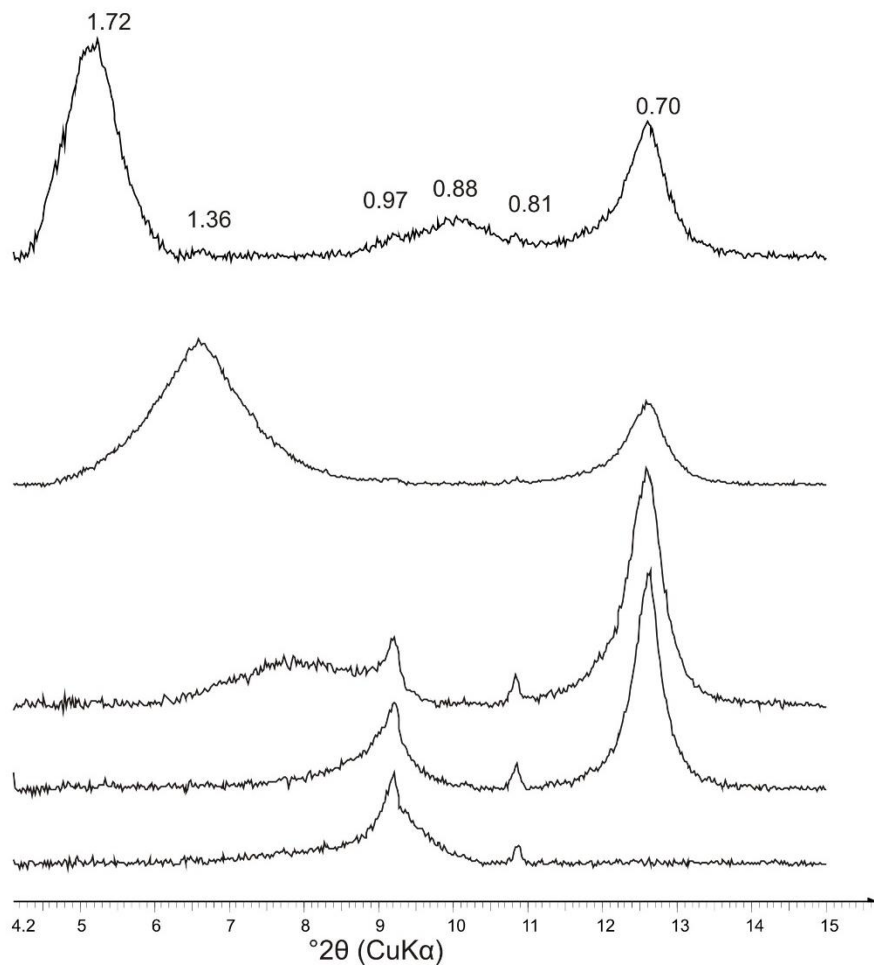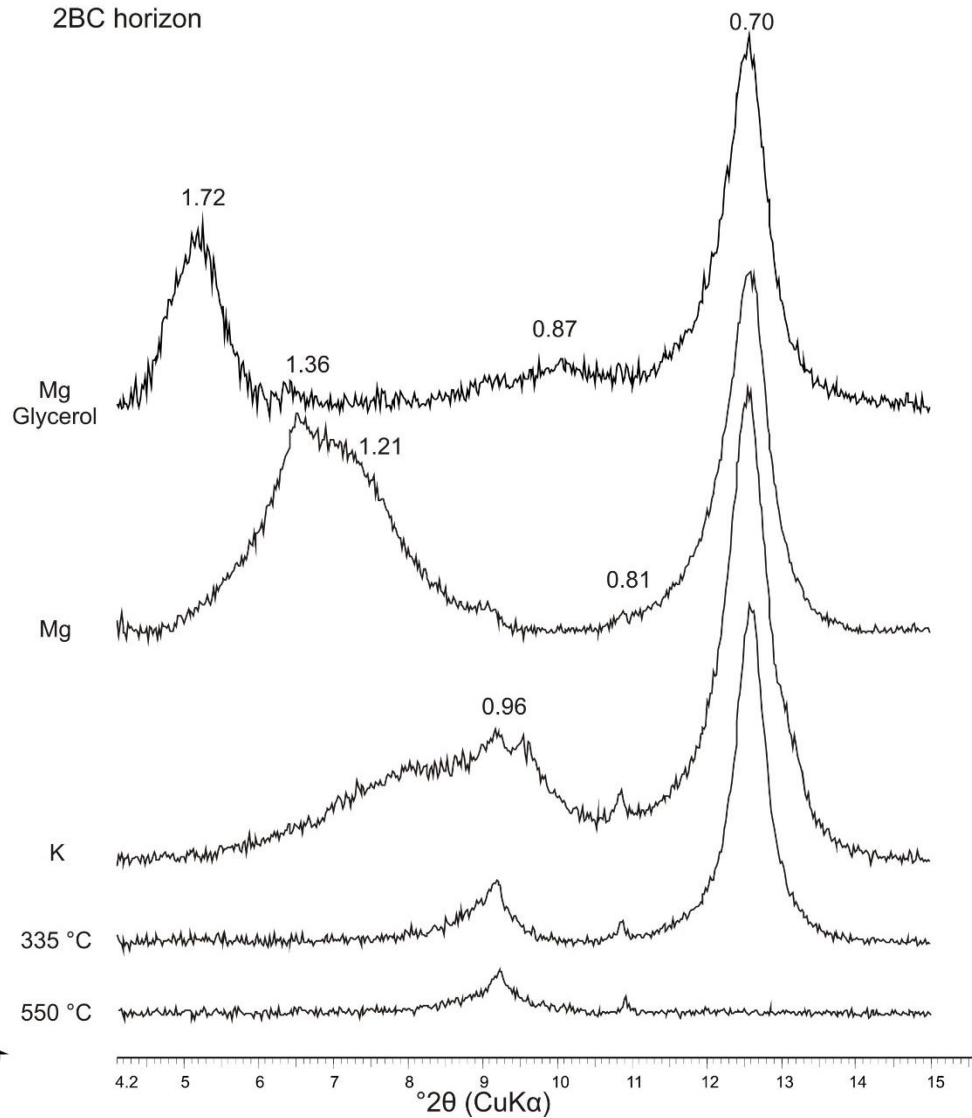
Fig. G6: XRD-plots from 4.2°2θ to 15°2θ for the 2Btg1 and the 2BC horizons of LS4.
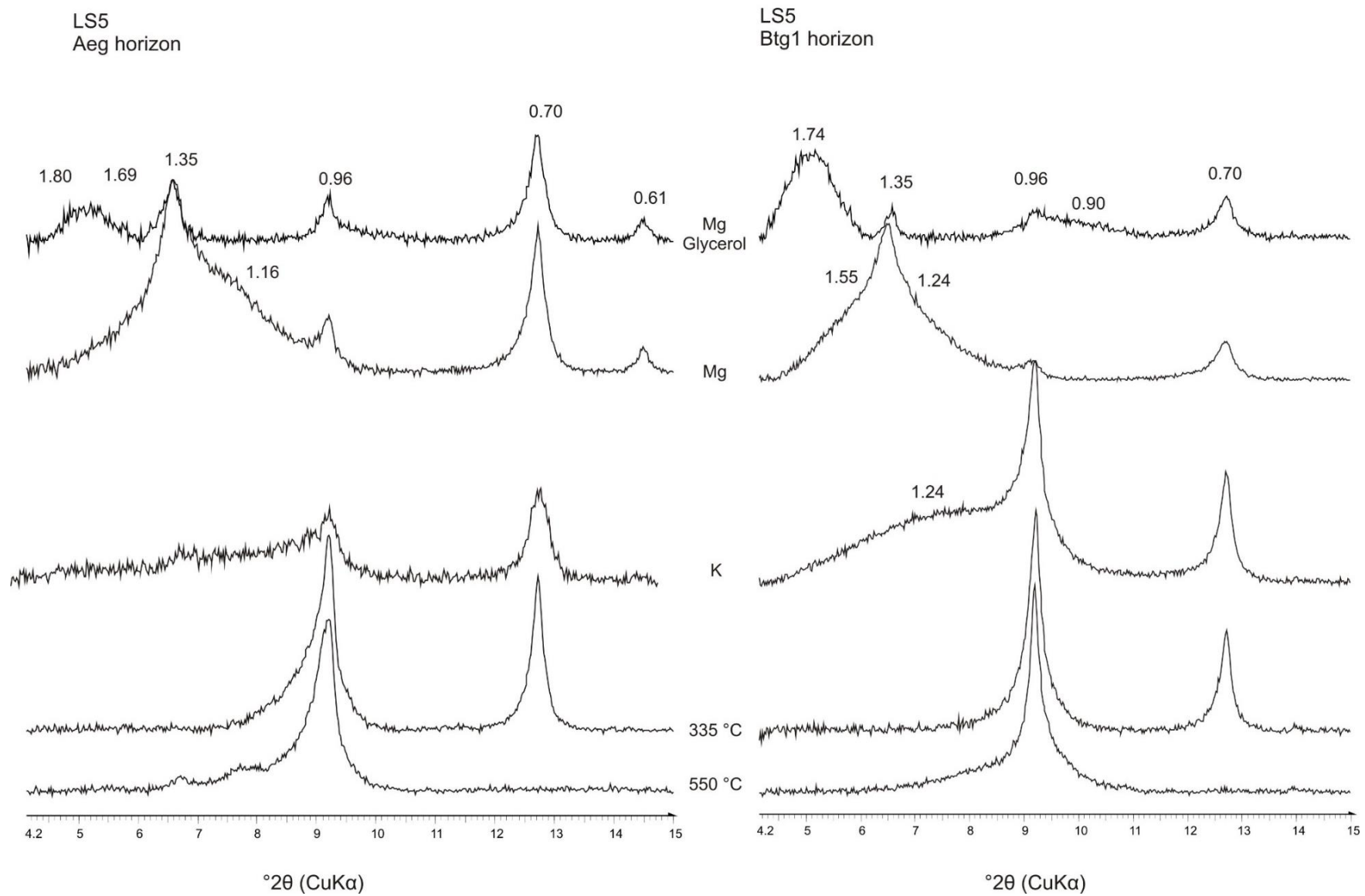
Fig. G7: XRD-plots from 4.2°2θ to 15°2θ for the Aeg and the Btg1 horizons of LS5.
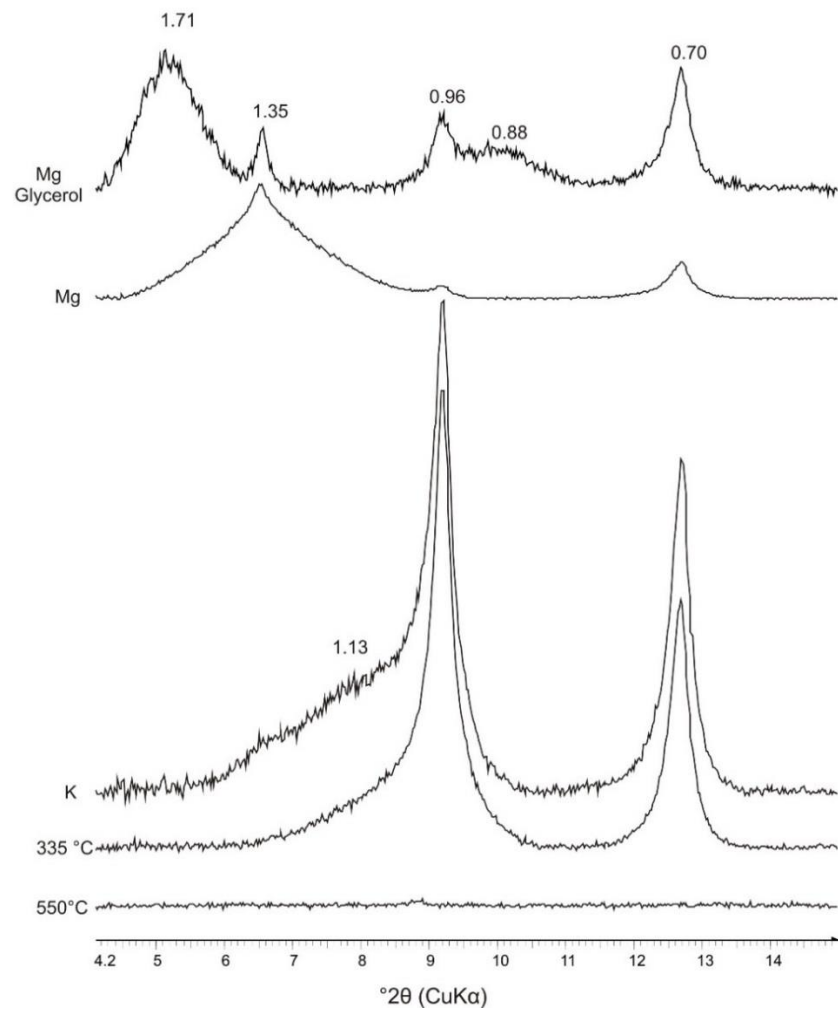
Fig. G8: XRD-plot from 4.2°2θ to 15°2θ for the 2CBtg horizon of LS5.
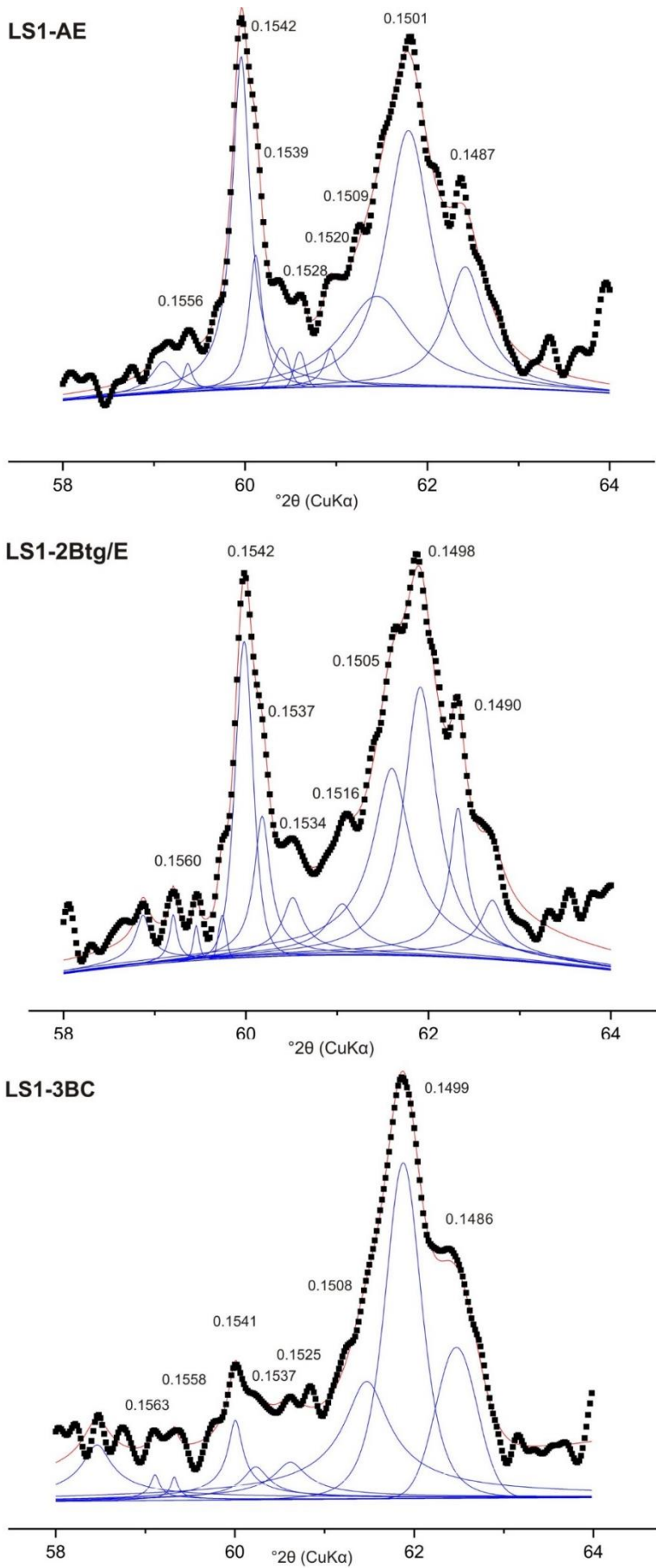
Fig. H1: Modelled curves of XRD pattern between 58°2θ to 64°2θ for LS1.
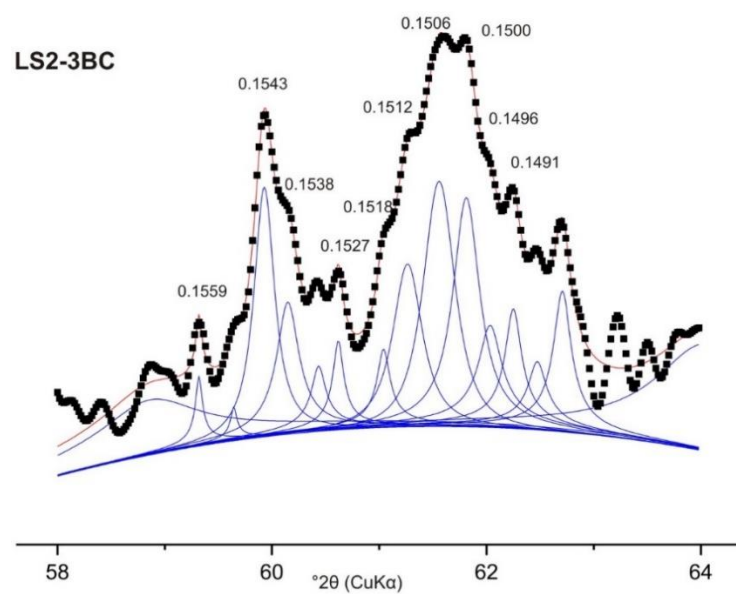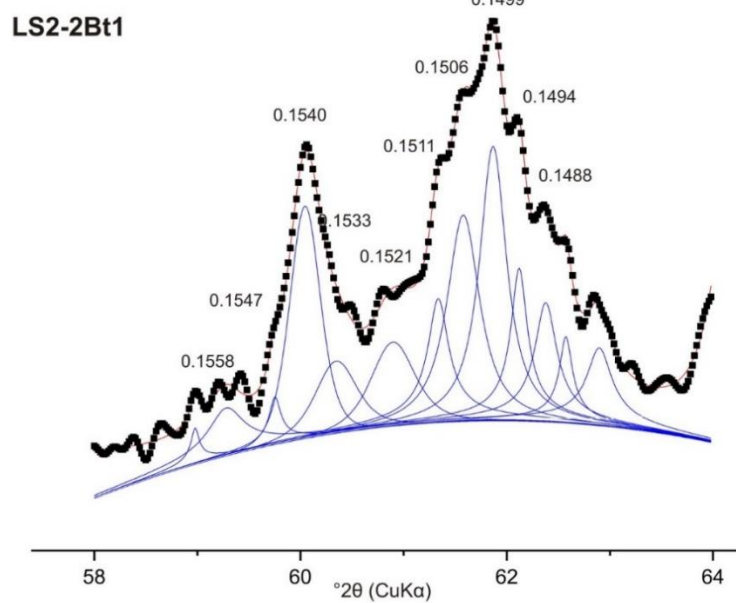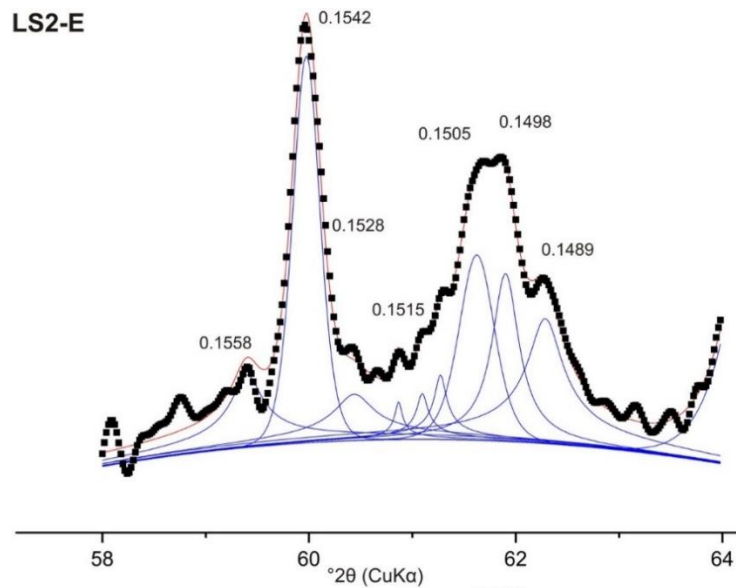
H2: Modelled curves of XRD pattern between 58°2θ to 64°2θ for LS2.
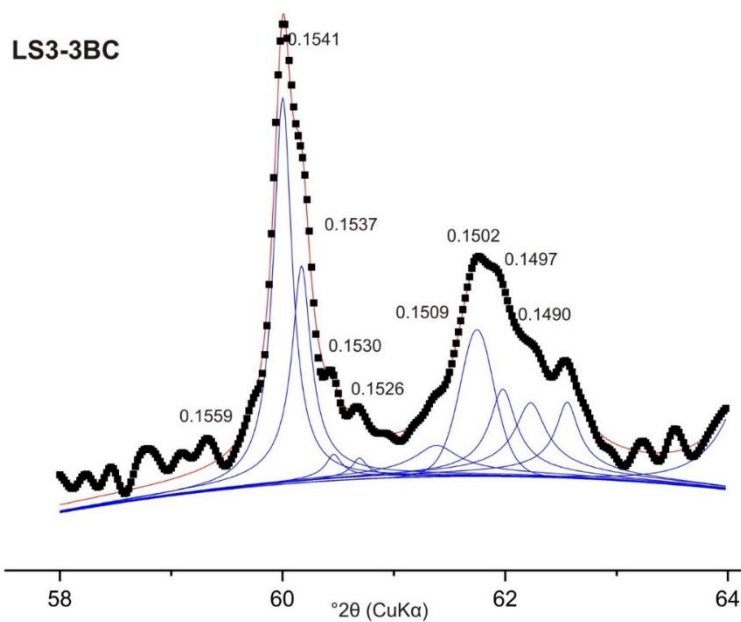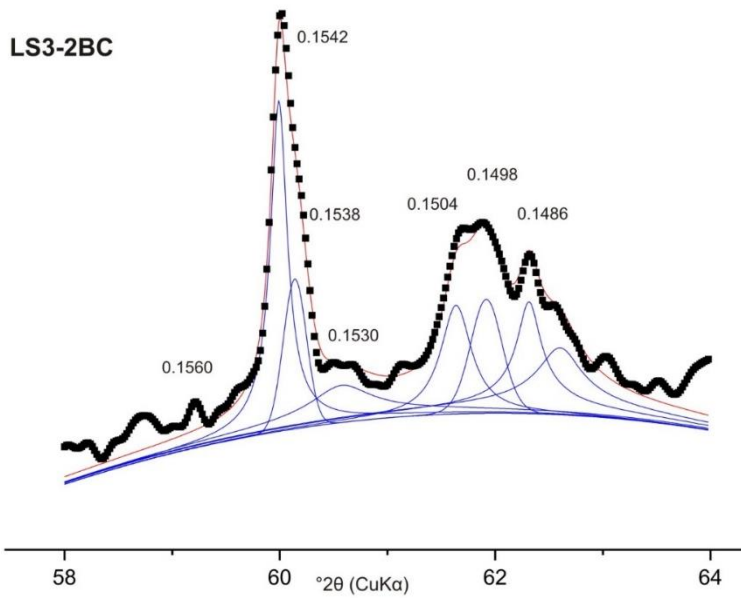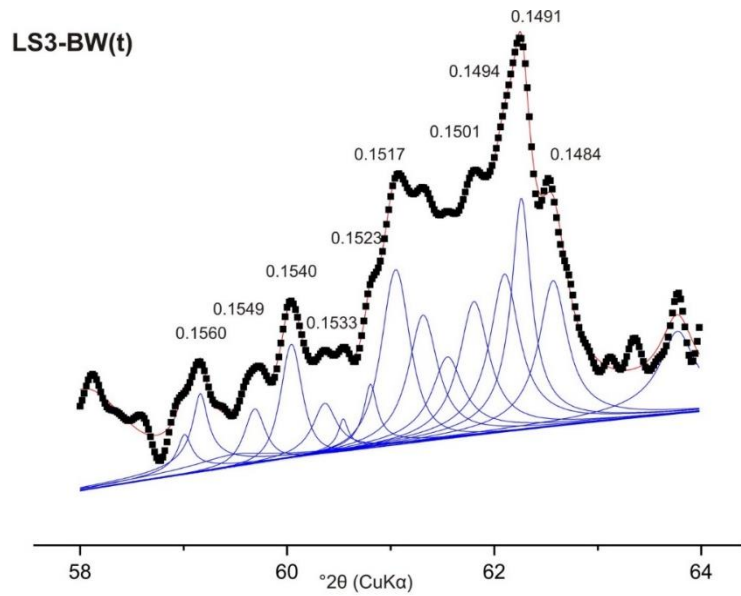
H3: Modelled curves of XRD pattern between 58°2θ to 64°2θ for LS3.
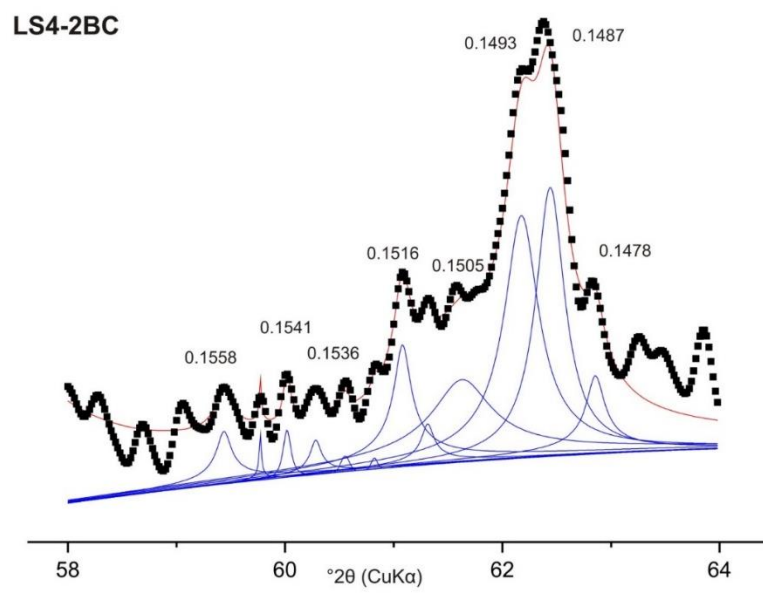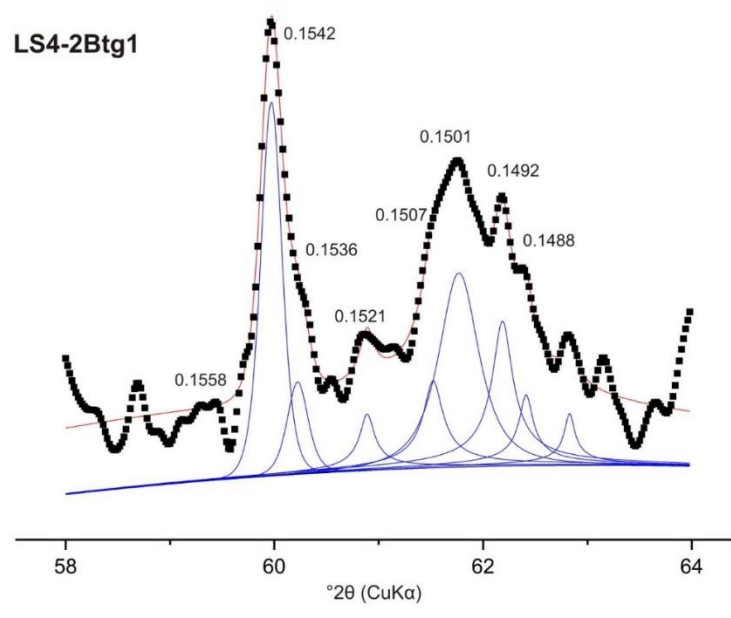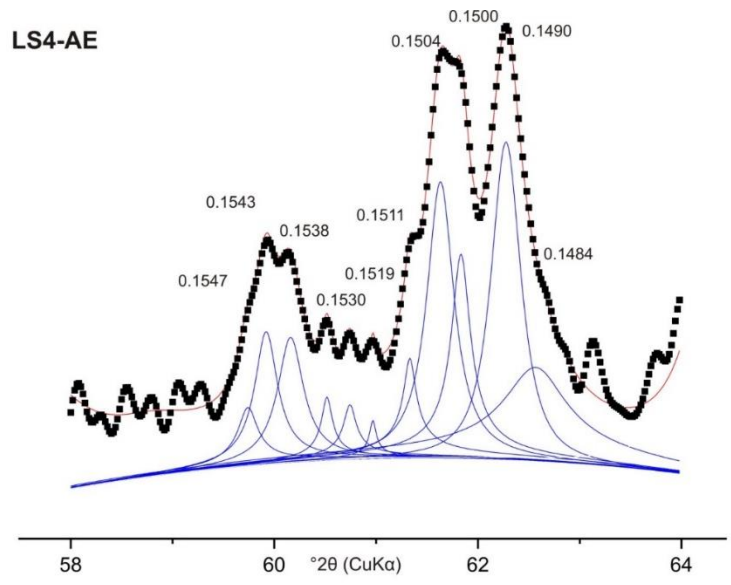
H4: Modelled curves of XRD pattern between 58°2θ to 64°2θ for LS4.
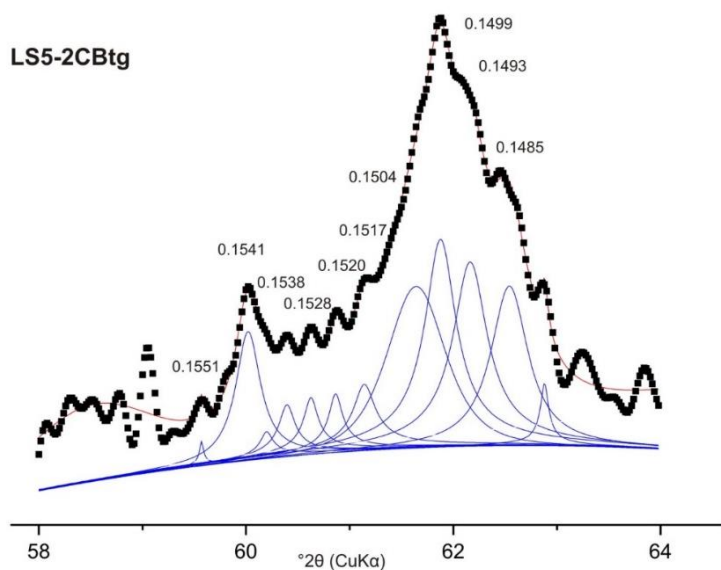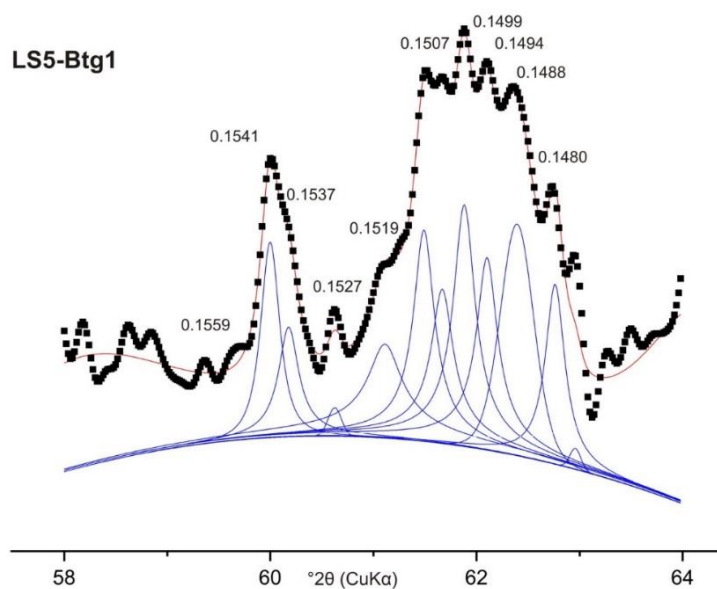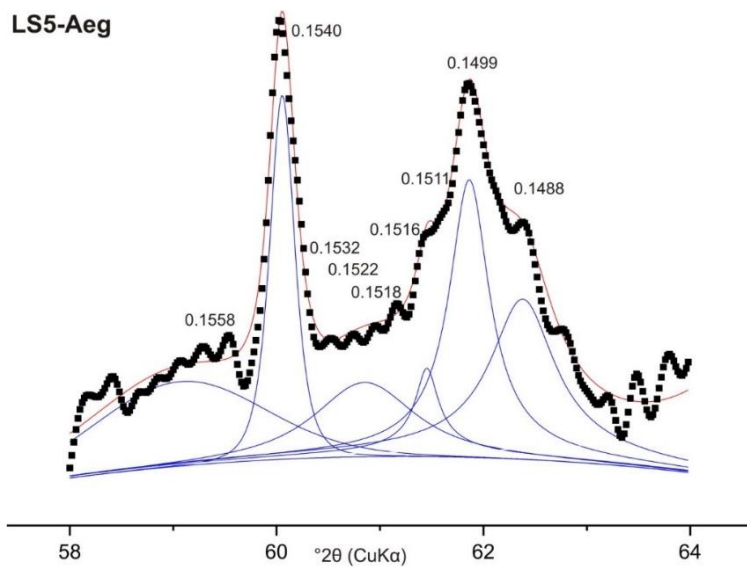
H5: Modelled curves of XRD pattern between 58°2θ to 64°2θ for LS5.

| | (cm⁻¹) | Sample 1 | 2 | 3 | 4 | 5 | 6 | 7 | 8 | 9 |
|---|---|---|---|---|---|---|---|---|---|---|
| Kaolinite | 3694 | x | x | x | x | x | x | x | x | x |
| | 3652 | x | x | x | x | x | (x) | x | x | x |
| | 3620 | x | x | x | x | x | x | x | x | x |
| | 474 | | x | x | | x | x | | x | x |
| | 348 | x | (x) | x | | | | x | | |
| Gibbsite | 3620 | x | x | x | x | x | x | x | x | x |
| | 3526 | x | | | x | x | x | x | | x |
| | 3469 | | | | | | (x) | x | x | |
| | 1017 | x | x | | x | x | (x) | x | x | x |
| | 366 | | | | | | | | (x) | x |
| Chlorite | 3676 | | | | | x | ? | | | (x) |
| | 3575 | (x) | | | | | | (x) | x | x |
| | 3428 | | | x | x | x | (x) | (x) | x | (x) |
| | 750 | x | (x) | | | x | x | x | (x) | x |
| Imogolite | 375 | x | x | x | x | x | x | x | x | (x) |
| | 348 | x | (x) | x | | | x | x | | |
| Kaolinite, Qz or Illite | 474 | | x | x | x | x | x | x | x | x |
| Illit, Muscovite | 531/474 | x/ | /x | x/x | x/x | x/x | (x)/x | x/x | x/x | /x |
| | 831/752 | | | (x) | | /x | (x)/(x) | x/x | (x)/(x) | x/x |
| oct. Mg/Fe | 650 | x | | | x | x | x | x | x | x |
| dioct. Smectite | 690 | (x) | | | x | (x) | x | (x) | x | x |
| Quartz | 692 | x | x | | x | x | x | x | x | x |
| Muscovite | 750 | x | (x) | (x) | | x | x | x | (x) | x |
| and Chlorite | | | | | | | x | | | |
| Qz-Doublet | 780/800 | x | x | | x | x | x | x | x | x |
| AlMgOH | 830 | x | (x) | | | | (x) | x | | x |
| Kaolinite | 915 | x | x | | x | x | x | x | x | x |

Fig. I1: Typical peaks/bands and their significance for LS1, LS2 and LS3, x = present, (x) = assumed

| | (cm$^{-1}$) | Sample 10 | 11 | 12 | 13 | 14 | 15 |
|---|---|---|---|---|---|---|---|
| Kaolinite | 3694 | x | x | x | x | x | x |
| | 3652 | x | x | | x | x | x |
| | 3620 | x | x | x | x | x | x |
| | 474 | x | x | x | x | x | (x) |
| | 348 | | x | (x) | x | x | |
| Gibbsite | 3620 | x | x | x | x | x | x |
| | 3526 | x | | (x) | x | (x) | x |
| | 3469 | | x | (x) | (x) | (x) | x |
| | 1017 | x | x | (x) | x | x | x |
| | 366 | | x | | | | |
| Chlorite | 3676 | | | | | | |
| | 3575 | (x) | (x) | | | | x |
| | 3428 | | (x) | | x | x | (x) |
| | 750 | x | x | x | x | x | x |
| Imogolite | 375 | x | | x | x | x | |
| | 348 | | x | (x) | x | x | |
| Kaolinite, Qz or Illite | 474 | x | x | x | x | x | (x) |
| Illit, Muscovite | 531/474 | x/x | x/x | x/x | x/x | x/x | (x)/(x) |
| | 831/752 | (x)/x | (x)/x | (x)/x | /(x) | /x | x/x |
| oct. Mg/Fe | 650 | x | | (x) | x | x | x |
| dioct. Smectite | 690 | x | x | x | x | x | x |
| Quartz | 692 | x | x | x | x | x | x |
| Muscovite and Chlorite | 750 | x | x | x | x | x | x |
| Qz-Doublet | 780/800 | x | x | x | x | x | x |
| AlMgOH | 830 | (x) | | x | (x) | | |
| Kaolinite | 915 | x | x | x | x | x | x |

Fig. I2: Typical peaks/bands and their significance for LS4 and LS5, x = present, (x) = assumed

# Personal declaration

Personal declaration: I hereby declare that the submitted thesis is the result of my own, independent work. All external sources are explicitly acknowledged in the thesis.

Place and date                                  Signature

Basel,

23rd of September 2018